On the Design of a Combined Raman and Interferometric Scattering High Resolution Microscope

by

Ashton Christy

B.Sc. Hons., The University of British Columbia, 2012

A THESIS SUBMITTED IN PARTIAL FULFILLMENT
OF THE REQUIREMENTS FOR THE DEGREE OF

Master of Science

in

THE FACULTY OF GRADUATE AND POSTDOCTORAL STUDIES
(Chemistry)

The University Of British Columbia
(Vancouver)

July 2016

Abstract

Contemporary imaging science needs label-free methods of microscopy that resolve morphological and chemical information in complex materials on a submicron length scale. Many of the most commonly-used techniques require substantial adulteration of samples, and thus are hindered in their utility for in vivo or time-resolved studies.

This thesis introduces a new approach that integrates a confocal Raman microscope with interferometric scattering, or iSCAT. The former technique is well-reported in the literature; iSCAT, however, is relatively novel. The principles of iSCAT, developed in the last few years, have established a platform that provides superior resolving power and signal contrast compared with other optical techniques. Our novel approach integrates wide-field iSCAT microscopy acquired at video rate with point-by-point confocal Raman spectroscopy.

After first providing a brief overview of contemporary methods in microscopy and the challenges they present, this thesis discusses the basics of iSCAT, and the design and development of the instrument that unites this new technique with confocal Raman microscopy. A discussion of design challenges follows. Next is a description of the instruments user-end capabilities, followed by a brief exploration of future prospects.

Provided throughout the text are results illustrating the capability of the instrument. These demonstrate how much potential the combination of iSCAT and Raman holds for characterizing complex materials, as well as the precision with which the instrument can do so. Wide-field images, 100 μm square with 200 nm resolution, are sampled at 45 frames per second. The integrated Raman probe provides label-free highly reproducible chemical information without sample degradation. Together, these two data sets provide insights into covariance between morphology and chemistry, all with minimal sample preparation.

Preface

The original idea for the instrument presented in this thesis was concieved with the partnership of the pulp and paper industry, as well as the pioneering work of Dr. Philipp Kukura at Oxford University. The instrument in its various configurations (Chapters 3-6) was largely designed by me, with assistance in design refinement and construction provided by Dr. Qifeng Li of Tianjin University. The instrument's user interface, outlined in Chapter 7, was coded by me.

The research presented in this thesis provided the foundation for the following conference presentation: A. Christy, N. Tavassoli, A. Bain, L. Melo, and E. R. Grant, "Wide-Field Confocal Interferometric Backscattering (iSCAT)-Raman Microscopy," in *Optics in the Life Sciences, OSA Technical Digest* (online) (Optical Society of America, 2015), paper NM4C.4. I prepared and delivered the presentation at the conference in April 2015, and the text published online was drafted by Dr. Edward Grant, with input from all co-authors.

Pulp and paper samples were provided by FPInnovations and Canfor Corp. Aerosol samples were provided by the lab of Dr. Allan Bertram, Department of Chemistry, University of British Columbia. Brain tissue samples were provided by the lab of Dr. Shernaz Bamji, Department of Cellular and Physiological Sciences, University of British Columbia. Mineral samples were provided by Dr. Gregory Dipple, Department of Earth, Ocean & Atmospheric Sciences, University of British Columbia. Plant specimens were provided by the University of British Columbia Herbarium.

Table of Contents

List of Figures

List of Equations

Glossary

Acronyms

50:50 BS 50:50 Beamsplitter Cube, an optical component that uses two equilateral triangular prisms fused together on their hypotenuses to form a cube; this configuration reflects 50% of incident light at an angle of 45°, and allows 50% of incident light to pass through the cube unperturbed. They can be oriented in either a right- or left-handed configuration.

AOD Acousto-Optic Deflector, an optical hardware component that uses a radio frequency electrical input to piezoelectrically induce shear waves in a tellurium dioxide (TeO_2) crystal; light passing through the crystal is deflected along a rastering pattern.

AFM Atomic Force Microscopy, a microscopic surface analysis technique that functions in a manner analogous to a record player; a needle is dragged over a surface, and vibrations caused by surface topology are used to reconstruct a surface image.

ATR-FTIR Attenuated Total Reflectance-Fourier Transform Infrared Spectroscopy, a widely used suite of spectroscopic techniques commonly bundled into a single instrument. The ATR portion of the instrument uses a crystal with a high refractive index to send an infrared evanescent wave into a sample. The reflected light is then collected into the FTIR portion of the instrument, where the data are converted from the frequency to the time domain, and are collected with a very high sensitivity. [18]

CCD Charge-Coupled Device, a type of high-sensitivity photodetector that consists of an array of metal-oxide-semiconductor pixels, and that allows accumulated photoelectric charge to be shifted between pixels to an external amplifier. A more specialized, sensitive, and expensive alternative to a CMOS sensor.

CMOS Complementary Metal-Oxide-Semiconductor sensor, a type photodetector that consists of an array of metal-oxide-semiconductor pixels, each with an integrated amplifier unit. A cheaper and less sensitive alternative to a CCD.

CRT Cathode Ray Tube, a type of screen that uses an electron beam to illuminate phosphorescent pixels to display an image.

DBS Dichroic Beamsplitter, an optical band-rejection filter that uses a dichroic optical coating to split light of a certain frequency range away from its incident beam path.

DWT Discrete Wavelet Transform, a method of multivariate analysis that decomposes a signal into a set orthogonal wavelets. Some wavelets (highest and lowest frequencies) are discarded, and the signal is reconstructed from the remaining wavelets.

FPS Frames per Second, a measure of the data retrieval rate from an image sensor.

HeNe Helium-Neon laser, a type of gas-phase laser that uses a $10:1$ mix of helium and neon as its gain medium.

HNF Holographic Notch Filter, an optical component that uses a holographically etched surface to stop a very narrow range of frequencies.

iSCAT Interferometric Scattering Microscopy, a technique that relies on the interference between reflected and scattered light to observe refractive index morphology.

LCF Laser Clean-up Filter, an optical bandpass filter that uses an optical coating to transmit light over a very narrow range of wavelengths, used to filter out extraneous wavelengths generated by a laser.

NA Numerical Aperture, a number that quantifies the resolving power of a microscope objective.

NBSK Northern Bleached Softwood Kraft, a standard type of pulp produced from boreal softwood (i.e. coniferous) trees, used to reinforce writing paper and manufacture kraft and tissue paper. [49]

NDF Neutral Density Filter, an opitcal filter that uses smoked glass to attenuate light passing through it.

NEP Noise-equivalent Power, a measure of a photodetector's minimum detection threshold, integrated over half a second. That is to say, it is the power below which a signal is indistinguishable from random noise.

NIR Near-Infrared Spectroscopy, a spectroscopic technique using light in the near-infrared region, typically between 700 and 2500 nm. Its main advantage over conventional (mid-range) infrared spectroscopy is its penetration depth; NIR is commonly used in medicine.

NSERC Natural Sciences and Engineering Research Council of Canada

N-BK7 Nachfolgematerials Bor-Kronglas 7 (*lit. "Successor to Boro-Crown Glass 7"*), a proprietary type of high-quality borosilicate glass, developed and manufactured by Schott AG (Mainz, Germany), used in a wide variety optical applications.

OSC-SVM Orthogonal Signal Correction-Support Vector Machine, a pair of advanced multivariate statistical techniques used to build a classification model for complex sets of variables. These are designed to remove orthogonal data from the model to simplify it and yield better results, something which a Partial Least-Squares Regression cannot do. [90]

PCA Principal Component Analysis, a multivariate statistical technique used to rank orthonormal components of a transformed data set by their contribution to set's overall variance.

PLS Partial Least-Squares Regression, a multivariate statistical technique used to build a classification model for complex sets of variables, where correlations may not be readily apparent.

PMMA poly(methyl methacrylate), a transparent polymer with a wide variety of uses. Commonly known as acrylic, Plexiglas, or Lucite.

PSF Point Spread Function, a broadening or blurring of in-focus point sources on an image. Mathematically, it is the optical domain transfer function (as opposed to optical frequency), and is usually determined by the system rather than the sample.

ROI Region of Interest

RMSEP Root-Mean-Square Error of Prediction, a measure of the uncertainty of a classification model's predictions; as such, the lowest possible value is preferred. [87] In this way it the converse of the more commonly used Coefficient of Determination (R^2).

SDVM Second-Derivative Variance Minimization, an iterative data processing technique used to minimize the variance between a data signal and a background signal; it functions by successively subtracting the second derivatives of the signals from one another until their variance reaches some arbitrary threshold, then removing the computed background components from the data signal. [84]

SERS Surface-Enhanced Raman Spectroscopy, a Raman technique that employs surface adsorption to enhance the Raman effect of a sample by up to ten orders of magnitude, although the exact mechanism is still debated in the literature.

SiPM Silicon Photomultiplier, a type of photodetector consisting of an array of avalanche photodiodes on a silicon platform. SiPM detectors are exceptionally sensitive, able to detect single photons.

SITK Scientific Imaging Toolkit, a proprietary collection of LabVIEW software,

developed by RCubed Software (Princeton, NJ, USA), used for communicating with various scientific cameras.

TEM Transverse Electromagnetic Mode, a laser beam mode in which neither the electric nor magnetic field oscillates along the direction of light propagation. A 00 subscript (TEM_{00}) indicates the beam is propagating in a purely Gaussian shape.

TOGA Template-Oriented Genetic Algorithm, a type of evolutionary multivariate processing technique that uses a fixed set of predictor variables to guide its iterative calculations, in order to minimize their variance. [45]

VCO Voltage-Controlled Oscillator, a hardware component that uses an AC voltage input to control the oscillation frequency of its signal output.

VI Virtual Instrument, a proprietary file format used for LabVIEW software.

Acknowledgments

- Dr. Ed Grant
- Dr. Qifeng Li
- Najmeh Tavassoli
- Luke Melo
- The rest of the lab crew, past and present - Hossein, Julian, Mahyad, Evan, Jamie, Jachin, Zhiwen, Alison, Markus, J.P.
- The Canada Foundation for Innovation
- The Natural Sciences and Engineering Research Council of Canada

Chapter 1

Conceptual and Theoretical Background

This chapter will serve to frame the new instrument that is the focus of this thesis, in the context of a brief overview of contemporary microscopy and its limitations.

1.1 Contemporary Optical Microscopy

Optical microscopy is nothing new; the optical microscope dates back to at least 1609, when Galileo Galilei developed an instrument he called an *occhiolino*, consisting of two simple lenses. Since then, microscopes have offered us a view into what our eyes alone cannot see.

For most of the history of the microscope, designs tended to be quite simple, with a minimum number of lenses and simple incandescent illumination. Over time, as our understanding of optics progressed, new techniques were developed. This section outlines some of the most basic approaches to light microscopy.

1.1.1 Brightfield Microscopy

The simplest of all microscopies is termed *brightfield microscopy*. It simply consists of a lamp transmitting incoherent light through a sample and simple lenses or an objective to expand and collect the transmitted light. This transillumination approach requires that samples be transparent (and ideally colored); thus, a sample

appears dark on a bright background, hence the name of the technique. In modern applications, brightfield microscopy is often considered a "quick and dirty" technique, providing fast, reliable, and reproducible results, at the cost of low contrast and resolution. [1, 2]

1.1.2 Darkfield Microscopy

An alternative illumination approach, termed *darkfield microscopy*, uses an inverted configuration, where the light illuminates the sample through the objective, as opposed to through the sample. Thus, instead of collecting the transmitted light, the objective collects backscattered light. This causes a sample to appear bright on a dark background. Darkfield microscopy can provide better detail than brightfield because it does not collect shadows, but it typically cannot image a sample in its totality, and requires more specialized sample preparation than does brightfield. [1, 3]

1.1.3 Interferometric Microscopy

A number of techniques have been developed to enhance the contrast of transilluminated brightfield microscopy. These techniques exploit interference between transmitted and scattered light that has passed through the sample. The interference arises due to a shift in the phase of scattered light. Transmitted light does not interact with a sample, while scattered light does; thus, the optical path length of the scattered light is longer than that of transmitted light, causing the former to move slightly out of phase of the latter. This interference amplifies image contrast.

The first such technique, known as *phase-contrast microscopy*, uses a series of annular optics to exploit the phase shift caused by diffraction in a sample. Ring-shaped light is first focused onto a sample; light scattered (and phase-shifted) by the sample is collected as-is, while light transmitted by the sample is phase-aligned to either 0° or 180° relative to the scattered light, then attenuated. This phase modulation increases image contrast by introducing constructive interference between the transmitted and scattered light when they recombine at the image plane. Selectively attenuating the transmitted light further increases contrast. [4, 5] Thus, an image produced with a phase-contrast microscope is much more sharply resolved

than that produced with an analogous brightfield microscope.

Though phase-contrast microscopes are relatively simple and robust, they are limited by two factors; first, samples must be optically transparent. Second, the diffraction caused by the annular illumination often creates halos of light around samples, which can make interpreting an image somewhat more complicated. [4, 6]

An alternative approach to increasing phase contrast is Differential Interference Contrast microscopy (DIC), which uses a specialized prism to separate polarized illumination into two orthogonal rays. The separated rays enter the sample at slightly different positions, so after interacting with the sample, their phases are slightly different. The rays are recombined in another prism, and subsequently interfere. At points where there is little phase shift between the rays, there is constructive interference, and thus image brightening; conversely, where the phase shift is large, due to sample morphology, there is destructive interference and image darkening. In effect, samples appear to cast shadows at an oblique angle. [4, 6, 7]

As with phase-contrast microscopy, imaging opaque samples is not possible with a typical DIC microscope.[1] Additionally, the orientation of the recombination prism can have a substantial effect on the observed image, by rotating the angle of the sample "shadows"; thus, some features may become more pronounced at a different prism orientation, while others become less visible. [4, 6]

1.1.4 Disadvantages of Conventional Optical Techniques

Though these conventional light microscopy techniques are routinely used, they have serious limitations, probably the most widely recognized of which is the Abbe diffraction limit, shown below.

$$d = \frac{\lambda}{2n\sin\theta} = \frac{\lambda}{2 * \mathrm{NA}} \tag{1.1}$$

where λ is the illumination wavelength, n is the index of refraction of the sample medium, θ is the maximum half angle of the light cone exiting the objective, and Numerical Aperture (NA) is defined as: $\mathrm{NA} \equiv n\sin\theta$. In simplest terms, the limit

[1] By substantially altering the optical train of a DIC microscope, opaque samples can indeed be imaged, though this is not commonly done. [4]

can be understood following: one cannot measure something smaller than one's instrument of measure. In the context of optical microscopy, this effectively means that objects smaller than the wavelength of illumination cannot be resolved.

Another limitation of conventional optical techniques is their dynamic range of resolution. Specifically with regards to inverted microscopy, the detected intensity is dependent on the diameter of the sample scatterer to the sixth power (D^6).[2] With the Abbe diffraction limit in mind, this dynamic range scaling means that it can be difficult to observe fine features with specificity.

These two limitations mean that conventional techniques are not well suited to imaging the nanoscale samples that are often of interest to today's researcher.

1.2 Super-Resolution Microscopy

Recently, new developments in optical microscopy techniques have broken the Abbe diffraction limit. There are a number of ways this is accomplished, such as exploiting molecular fluorescence, or imaging using a nanoscale scanning probe.[8–12]

1.2.1 Scanning Probe Techniques

One approach to surpassing the Abbe diffraction limit is to decrease the size of the probe, thereby improving the angular resolution of the instrument beyond that of pure diffracted light. By feeding all the sample information through a nanoscopic conductor - a metal tip - the sources of the information can be localized with great precision.

Tip-Enhanced Raman Spectroscopy

Tip-Enhanced Raman Spectroscopy (TERS) is a popular technique to extract both chemical and topographical information from a wide range of samples. The probe itself, a nanoscopic gold tip, performs Surface-Enhanced Raman Spectroscopy (SERS); its point is small enough that its evanescent field enhances the Raman effect in samples by several orders of magnitude. [13, 14] The tip is kept a very short distance from the sample surface, and is illuminated by a laser; the most efficient illu-

[2] See Ch. 2.1 for more information.

mination geometry is in-line, that is to say, focused onto the tip through the sample. [14] The tip is then rastered across the sample surface, providing highly localized Raman spectra and effectively constructing an Atomic Force Microscopy (AFM) image. TERS can provide spatial resolutions in the tens of nanometers, but the Raman spectra it generates are often difficult to interpret without a reference collected using more conventional means. [13, 15]

Infrared Nano-Imaging (Nano-IR)

Infrared absorption is an alternative approach to imaging samples with a scanning probe. The instrumental design for a nano-IR experiment is very similar in principle to that of a TERS experiment, and in fact relies on a similar surface enhancement effect. [16, 17] Infrared absorption is label-free, provides complementary data to Raman spectroscopy, [18], and is often used to investigate metallic samples. [16, 19–21]

Disadvantages

Techniques that rely on metallic nanoscopic probes suffer one major drawback, and that is the sheer complexity of the setup they require. Nanoscopic probe tips are extremely delicate and prone to contamination, and thus require special accommodation. Isolating signals from these probes requires a very complex optical train, and generating a sample image requires a substantial time commitment. [14, 17, 21] Further, scanning probe techniques are designed for surface analysis, so imaging the interior of samples can be challenging. [13, 14]

1.2.2 Fluorescence Techniques

Another approach to breaking the Abbe diffraction limit is to resolve light sources within the sample (i.e. fluorophores), rather than relying on external light to illuminate the sample. Direct detection of fluorophores affords greater certainty of their position within the sample; thus, fluorescing sample features can be localized with greater precision than the Abbe diffraction limit would seem to allow.

The earliest effective super-resolution fluorescence technique involves selective depletion of fluorophores, and was awarded the Nobel prize in Chemistry in

2014. This depletion is generally referred to as the Reversible Saturable Optical Linear Fluorescence Transitions (RESOLFT) principle, and perhaps best known application is Stimulated Emission Depletion Microscopy (STED). [12, 22–25]

STED images samples with two laser pulses; one circular pulse to excite fluorophores within a sample, shortly followed by a second annular pulse (of a different color light) to quench the excited fluorophores, with the exception of those in the small central area of the ring. Thus, only those fluorophores this small central area are observed. The two beams are rastered over a sample, so that a super-resolved image of the sample can be built, with resolutions in the dozens of nanometers. [22, 23, 25]

Disadvantages

Using techniques such as STED requires that a sample contain spatially distributed photoswitchable fluorophores. These fluorophores must be introduced to samples, either as dyes or as labels. [12, 26] Though with the proliferation of highly functionalizable fluorescent proteins, this has become a routine procedure in most biological labs, labeling still presents several challenges. Label specificity and density are the most notable, as well as concerns about adulteration of the sample itself by the introduction of large proteins functionalized with antibodies. [27]

Another difficulty that often arises is photobleaching; that is to say, repeated exposure to high intensity light may alter the chemical structure of fluorophores (eg. the denaturing of a fluorescent protein), which prevents them from fluorescing. [10, 26] This is an especially relevant concern for stochastic methods, that collect sequences of fluorescence images.

Note that photobleaching is a separate phenomenon from quenching, as exploited by STED. Quenching is an electronic effect, where electrons are forcibly transferred to lower energy levels without fluorescing,[3] and no chemical changes take place. [22] Nonetheless, photobleaching does remain a problem with STED and RESOLFT techniques, albeit one of less concern than stochastic techniques. [24]

[3] Quenching forces an excited fluorophore to undergo stimulated emission, rather than fluorescence.

1.3 Interferometric Scattering Microscopy (iSCAT) As an Alternative

Given the pitfalls of conventional optical and fluorescence techniques, a new technique has been recently developed to offer an alternative, not necessarily to replace, but to compliment these techniques. The new technique is known as Interferometric Scattering Microscopy. Essentially, the technique exploits the interference between backscattered and reflected light from a sample to probe the sample's refractive index morphology. This is similar to the phase-contrast techniques mentioned above, but with the noted difference that iSCAT is an inverted microscopy technique, like darkfield, and does not use transillumination like phase-contrast and DIC microscopies. The next chapter will outline the technical aspects of the methodology, but its advantages bear mentioning here.

One of iSCAT's biggest advantages is iSCAT's much greater resolution than other optical techniques. In brief, iSCAT's dynamic range of resolution depends on a scatterer's diameter to the third power (D^3), as opposed as to the sixth power (D^6). The reasons are discussed in more detail in Ch. 2.1. In effect, this difference affords iSCAT a much greater ability to image smaller samples than techniques such as darkfield imaging.

A further advantage is that iSCAT is entirely label-free, i.e. that it requires no sample adulteration. This advantage is shared with conventional optical techniques. iSCAT is also entirely non-destructive, and photobleaching is not a concern. When combined with its increased resolution, iSCAT is well-suited to provide new insights into biological samples that may not be particularly compatible with other techniques.

When compared specifically with phase-contrast techniques, iSCAT can image both optically transparent and opaque samples without any alteration of the optical train. This allows for a much larger variety of samples to be imaged.

Chapter 2

Experimental and Technical Background

This chapter will outline the fundamental physical principles of two key methodologies, Interferometric Scattering Microscopy (iSCAT) and confocal Raman microscopy. This thesis focuses on the instrument that unites the two, as opposed to the methodologies themselves, this chapter will not delve into great detail, but will provide a review of the underlying principles sufficient for the reader to better understand the instrumental development outlined in the next several chapters.

2.1 iSCAT: Interferometric Scattering Microscopy

In their seminal 2012 paper, Kukura and Ortega-Arroyo describe Interferometric Scattering Microscopy as "*[yielding] extremes in sensitivity and speed that have until recently been deemed far beyond reach in fluorescence-free optical microscopy.*"[28]

Generally, iSCAT has a nearly identical in setup to darkfield imaging; that is to say, it relies on an inverted objective. This differs from phase-contrast techniques; although they rely on similar interference, the latter use transmitted light. In an inverted regime, detected intensity I generally depends on the sum of the reflected and backscattered light fields, $E_{\text{reflection}}$ and $E_{\text{scattering}}$ respectively.

I can be calculated as follows:

$$I = \frac{1}{2} c\varepsilon \left| E_{\text{reflection}} + E_{\text{scattering}} \right|^2 = \left| E_{\text{incident}} \right|^2 \left\{ r^2 + |s|^2 - 2r|s| \cos\phi \right\} \tag{2.1}$$

where c and ε are the speed of light and permittivity of the medium, respectively, r and s are the reflection and scattering amplitudes, respectively, E_{incident} is the incident light field (from the illumination source), and ϕ is the phase difference between the reflected and scattered light.[1] [28, 29] The right-most term in Eq. (2.1) is obtained by expanding the reflection and scattering field terms, assuming that they interfere. [29] In this formulation, it is easier to separate iSCAT from darkfield microscopy. The three resulting variables represent reflected, scattered, and interfering light, respectively.

In the darkfield regime, scattered light is the dominant contribution to the detected intensity I; thus, Eq. (2.1) becomes:

$$I_{\text{darkfield}} = \left| E_{\text{incident}} \right|^2 |s|^2 \tag{2.2}$$

This simple scattering-based formulation is observed in darkfield images, in which the sample appears light and the background appears dark. However, iSCAT relies not on the pure backscattering from a sample, but on the interference between that backscattering and the reflected light from the sample.

The eponymous interference arises because light that is backscattered from a sample has a longer optical path length than light that is simply reflected from the sample surface; thus, is phase-shifted with respect to reflected light. The difference in path length, manifested as phase difference, is due to refraction within the sample. Snell's law (Eq. (2.3)) describes how light bends when passing through an interface between materials with different indices of refraction.

[1] In a standard transillumination scheme, used for brightfield or phase-contrast microscopies, the reflection field is replaced with a background field, $E_{\text{background}}$. Otherwise the math in Eq. (2.1) remains the same.

$$\frac{\sin\theta_1}{\sin\theta_2} = \frac{n_1}{n_2} \tag{2.3}$$

The ratio of indices of refraction (n) of the sample determines the angle of refraction (θ), and thus the path length. Since backscattering may occur throughout a sample, and an inhomogeneous sample will have a pronounced refractive index morphology, backscattered light collected by the inverted objective will likewise have an inhomogeneous set of phases. When reflected light from the flat glass coverslip (or from the sample itself) is taken as a reference, the interference between said reflection and the backscattered light will provide an accurate image of the sample's refractive index morphology, visible as variations in detected intensity.

Returning to Eq. (2.1), it can be assumed that most iSCAT samples are weak scatterers, such that $r \gg s$; thus, the interference term will outweigh the pure scattering term. The resulting iSCAT image will therefore look more like a brightfield image, with dark features on a light background. Eq. (2.1) becomes:

$$I_{\text{iSCAT}} = |E_{\text{incident}}|^2 \left\{ r^2 - 2r|s|\cos\phi \right\} \tag{2.4}$$

Thus, it can be seen that the interference will be destructive when the scattered and reflected light are in of phase (i.e. when $\phi = 0$ or 2π), and constructive in the converse case (when $\phi = \pi$). For strongly scattering samples, i.e. when $r \leq s$, the $|s|^2$ term in (2.1) becomes non-negligible, and the iSCAT image inverts; light features will be observed on a dark background. [28–30]

In either case, the iSCAT signal contrast C can be determined as follows:

$$C = \frac{I_{\text{signal}}}{I_{\text{background}}} = \frac{\text{interference}}{\text{reflection}} = \frac{2|s|\cos\phi}{r} \tag{2.5}$$

Note that the contrast is linearly dependent on scattering amplitude $|s|$. Per Mie theory, this in turn means that the dynamic range of feature sizes visible to iSCAT is scaled to the third power (D^3). The equation below (Eq. (2.6)) shows the wavelength-dependent scattering cross-section of an object, as determined by Mie

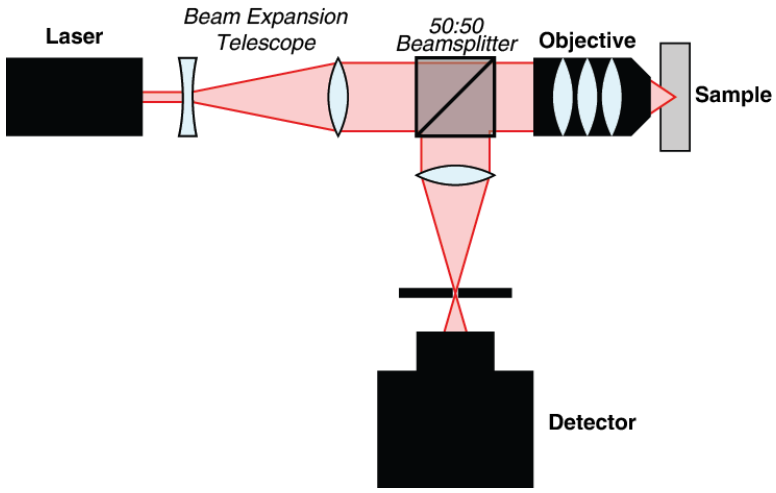

Figure 2.1: A simplified outline of a single-channel iSCAT experiment.

theory.[2]

$$s(\lambda) = \frac{\pi D^3}{2} Q_{ext}(m, \alpha) \tag{2.6}$$

where D_p is the diameter of the scatterer and Q_{ext} is extinction efficiency, the latter dependent on refractive index and the dimensionless size parameter $\alpha \equiv \pi D/\lambda$. Referring to Eq. (2.2), the contrast provided by darkfield microscopy has a quadratic dependence on the scattering amplitude, due to the dominance of the $|s|^2$; thus, darkfield's dynamic range of resolution scales with D^6. Recall from Eq. (2.4) that iSCAT's intensity depends on $|s|$ in the interference term; thus, the dynamic range of its resolution scales with D^3.[3][28, 29, 31] In practical terms, this gives iSCAT a much broader detection range, allowing it to observe much smaller features than darkfield microscopy, though both are ultimately Abbe diffraction-limited.

Figure 2.1 shows a schematic of a basic single-channel iSCAT detector. The detector, in this case, would be something like a photodiode or a Silicon Photomul-

[2]Mie scattering occurs when the wavelength of light and diameter of the scatterer are on the same order of length. The actual mathematics involved are beyond the scope of this thesis. [31]

[3]Brightfield and phase-contrast microscopies' dynamic ranges also scale with D^6.

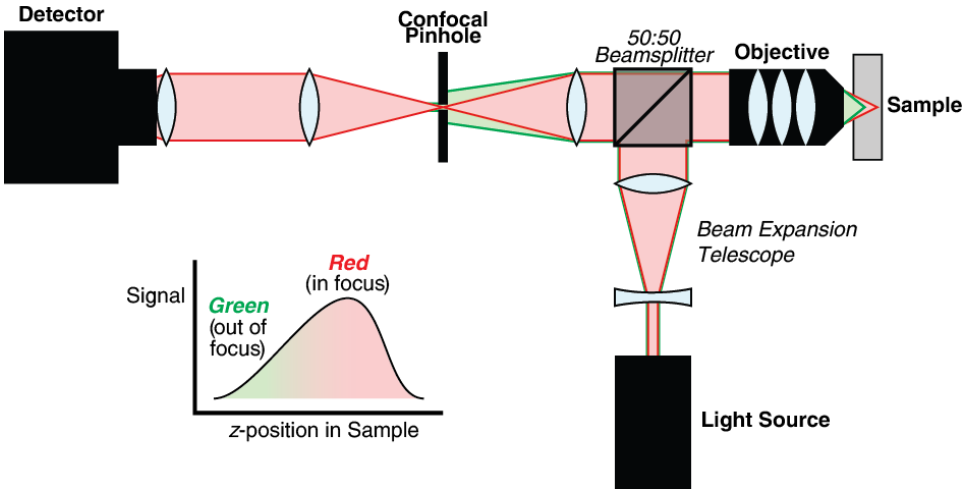

Figure 2.2: A simplified outline of a confocal experiment, showing in-focus (red) and out-of-focus (green) light.

tiplier (SiPM). The interference pattern would be measured by the detector (along with the reflection background; see Eq. (2.4)); the interference would vary over the spatial domain of the sample, and by collecting a series of points across the sample, an image could be reconstructed.

2.2 Confocal Raman Microscopy

The basic principle of confocality is evident in its name: a focus point in a sample is also focused through a pinhole. Thus, in a confocal microscope, out-of-focus light from the sample is largely - though not completely - excluded by the pinhole, and the in-focus image can be collected with much higher contrast than with a conventional optical microscope. [32]

The basic outline of a confocal microscope can be seen in Fig. 2.2. Light is focused through a fixed objective onto a sample; light returning from the sample through the objective is fed through a confocal pinhole and into a detector. The position of the pinhole must be tuned so that it collects exclusively in-focus light. The graph on Fig. 2.2 shows the detected signal with respect to the position of origin within the sample (along the z-axis). At lower z values, i.e. z values below the focal length of the objective, light is largely excluded by the pinhole, and relatively

little signal reaches the detector. When the z value is equal to the objective's focal length, the light is focused through the pinhole, and collected in its entirety by the detector. Moving the sample is all that is required to image different areas of the sample, since the focal length and position of the objective are fixed.

In order to optimize confocal methodology, care must be taken to choose the right optical components. This includes an appropriate objective and pinhole; Numerical Aperture (NA) and pinhole diameter both affect performance. The choice of objective affects the shape and position of the light cone in the sample, which in turn determines the size of the focus point, and thus, the pinhole. [33, 34]

There is a plethora of literature regarding confocal Raman microscopy, especially relating to its uses in the life sciences. [11, 35–41] One of its big advantages is its ability to perform *in vivo* imaging of biological tissues. [42–44] This is partly due to its purely optical, non-invasive nature, as well as its minimal sample preparation. The other key advantage of Raman spectroscopy that lends itself to *in vivo* imaging, compared to similar non-invasive techniques such as Fourier Transform Infrared (FTIR), is that water heavily absorbs infrared light, and transmits visible light. Thus, Raman spectroscopy conducted in the visible range is better able to characterize biological samples that consist mainly of water. [38, 43]

2.3 A Novel Combination

Merging confocal Raman microscopy with iSCAT microscopy presents a number of unique opportunities. There are two main disadvantages to Raman microscopy. Firstly, not every material is susceptible to the Raman effect, and secondly, most materials that are scatter very weakly and are difficult to observe and quantify, even using a confocal microscope.

By pairing confocal Raman microscopy with iSCAT, these limitations are not necessarily resolved, but they become less of a concern. Rather than necessitating adulterative Raman enhancement methods such as Surface-Enhanced Raman Spectroscopy (SERS), iSCAT opens up a second window on a sample, where a researcher can observe refractive index morphology that is often complementary to chemical morphology. Thus, the non-invasive, label-free approach is preserved, and two data sets can be obtained from a single sample with a single instrument.

Another advantage, specifically arising from the two complementary data sets, is the ability to instantaneously cross-reference iSCAT and Raman data. iSCAT imaging may reveal information about a sample that is invisible to Raman microscopy, and vice versa. Further, if there is a region of particular interest that is visible in an iSCAT image, the confocal Raman probe can be directed to that specific region, obviating the need for lengthy trial-and-error approaches to collecting meaningful Raman data.

The process of combining these two techniques into a single working instrument is outlined in the next several chapters.

Chapter 3

Early Stages of Design

From a sketch on the proverbial cocktail napkin to a working reality: this chapter describes the development and construction of the first ever microscope to combine confocal Raman spectroscopy and Interferometric Scattering Microscopy (iSCAT). The earliest designs were significantly altered by the time the instrument was completed. One need only glance at Figs. 3.3 and 4.1 to see the divergence; this process of design refinement is described in this chapter, and the finalized instrument is described in the next (Ch. 4).

3.1 Early Work

Initially, the new microscope instrument was conceived of as both an exercise in optomechanical engineering and, more importantly, as a way to better examine samples of wood pulp and paper products. At the time this new instrument was coming together as a concept, much work was being done in the lab on the classification of samples provided by our research partners in the forestry and paper industry. This work involved taking many Raman spectra of a variety of samples, then using a variety of chemometric methods to build a classification model for various sample parameters of import to the industry. Some of these models also involved data taken using Near-Infrared Spectroscopy (NIR) and Attenuated Total Reflectance-Fourier Transform Infrared Spectroscopy, both of which provide much higher signal strength than spontaneous Raman spectroscopy. [18]

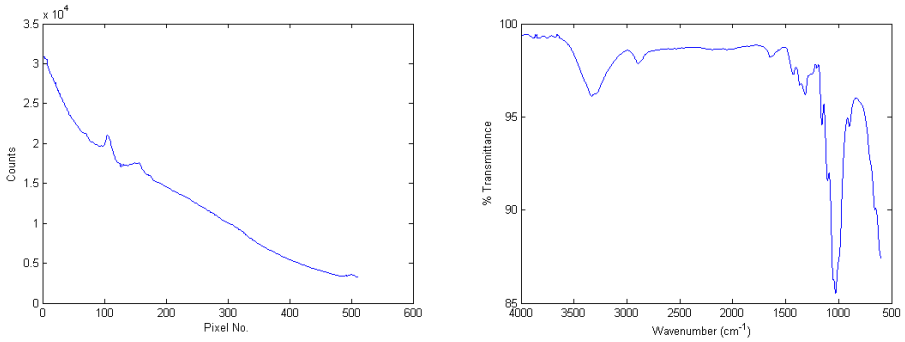

Figure 3.1: Raman spectrum (left, taken using the *RP-1* instrument; integration time 4 s) and ATR-FTIR spectrum (right; average of 20 scans) of a tissue paper sample.

3.1.1 Non-Confocal Raman Instruments

The Raman data was collected from the pulp and paper samples using one of two instruments, as described below.

RP-1

The first instrument routinely used was an *RP-1* "Raman Gun", manufactured by SpectraCode, Inc. (formerly of West Lafayette, IN, USA). The instrument itself was created for use when sorting plastic materials for recycling; it was designed to collect a library of spectra from samples of known composition, and to classify unknown samples using that library. Thus, it was well suited for use with the classification of pulp and paper samples. Its robust, user-friendly design meant that no modifications were needed.

The *RP-1*'s spectrograph is a 150 mm (f/4.0) component monochromator, manufactured by Acton Research Corp. (Acton, MA, USA), and the detector is a Charge-Coupled Device (CCD) camera comprised of a 1024×256 array of 20 μm pixels. The *RP-1*'s laser source is a 785 nm, 350 mW single-mode diode source, suitable for spontaneous Raman spectroscopy. The light itself is guided to and from the sample using fiber optics; this was necessary to construct the mobile "gun" probe, which was designed to be used by minimally-trained employees.

When used to collect data from pulp and paper samples, the "gun" was mounted

in a vertical position, with the active end pointing down towards the sample. Since the probe's internal optics have a fixed focal length of several centimeters, its vertical position was fixed, and the sample stage was placed on a lab jack. Said stage consists of a fixed sample holder attached to a spinning plate, designed to allow the RP-1 to collect data over an area of the sample, rather than just a single point. Thus, a single spectrum (with an exposure time of a second or more) contains spatially averaged data; in theory, this would average out any sample abnormalities.

Due to the limitations imposed by the pre-packaged design of the RP-1, attenuating background light proved difficult; the best (or, at least, easiest) solution was simply to shroud the "gun" and sample stage with a blanket. This has the clear drawback of impeding user access to both the "gun" and the sample. Additionally, the *RP-1*'s use of fiber optics mean that the system is especially susceptible to picking up sample fluorescence and background noise, even when shrouded. Both drawbacks necessitated the frequent use of background removal. The lack of confocality also limits the *RP-1*'s resolution. However, despite those issues, the robustness of the *RP-1*'s design mean that it is eminently reliable, and records highly reproducible spectra. An example can be seen in Fig. 3.1.

The *RP-1* requires no sample preparation whatsoever; that was indeed the goal of its gun-like point-and-shoot design. This unfortunately makes the *RP-1* impossible to use with certain types of samples, especially those that necessitate microscope slides. Since the list of incompatible samples includes most samples of biological and biomedical interest, the *RP-1* alone could not satisfy the research goals of the group.

Olympus Microscope (*BX51*)

Another instrument that was routinely used to collect data was a Raman microscope. This instrument consists of a 785 nm, 300 μW diode laser manufactured by Innovative Photonic Solutions (IPS) (Monmouth Junction, NJ, USA), fiber-coupled to an upright optical microscope (model no. *BX51*, manufactured by Olympus Corp., Shinjuku, Toyko, Japan). Much as with the *RP-1*, light returning from the sample is spread through a vertical stack of fibers onto a 300 mm monochromator manufactured by Acton Research Corp. (Acton, MA, USA), and detected by a

back-cooled CCD camera (PIXIS family, manufactured by Princeton Instruments, Trenton, NJ, USA). [45]

Although the *BX51* microscope routinely provides reproducible spontaneous Raman spectra, its resolution is still limited, due to the nature of fiber optics and its lack of confocality. Nonetheless, its ability to probe samples on microscope slides makes it highly useful. Its sample stage features manual and computer-controlled positioning, which allows sample surfaces to be held in place or easily scanned, both of which were distinct challenges using the *RP-1*.

ATR-FTIR

As mentioned previously, an Attenuated Total Reflectance-Fourier Transform Infrared Spectroscopy (ATR-FTIR) instrument was used to take additional data for use in classification models. The instrument is located in the UBC Chemistry Department's Shared Instrument Facility (SIF); it is a commercial PerkinElmer Frontier™ Fourier Transform Infrared (FTIR) spectrometer (Waltham, MA, USA), with an Attenuated Total Reflectance (ATR) attachment. See Fig. 3.1 for an example.

3.2 Classification Models and Chemometrics

Most of the samples processed using the *RP-1* were of soft tissue paper, provided by FPInnovations (Pointe-Claire, QC, Canada). The ATR-FTIR was mainly used with bleached and unbleached cardboard samples provided by Canfor Corp. (Vancouver, BC, Canada). The *BX51* microscope was used for both types of samples (and for other projects besides).

The immediate goal of the work was to see if Raman spectroscopy, using the *RP-1* to begin with, would be able to accurately predict a number of the paper samples' intrinsic qualities, such as handfeel (or softness), tensile strength, burst strength, tear strength, and pulp density. Some of these parameters, especially those related to physical strength of the pulp samples, are fairly easy to determine using standard force gauging equipment. However, finding some parameters, such as cellulose content, requires the lengthy and destructive chemical transformation of samples. [46] Still other parameters, such as handfeel, are entirely subjective, and cannot be determined before the product manufacture is complete. The forestry

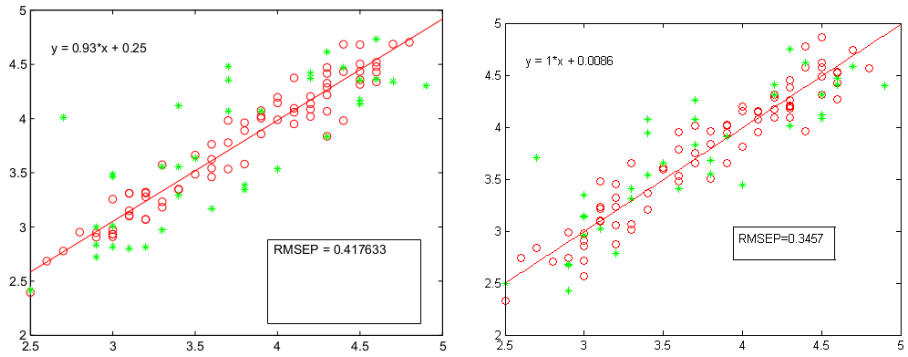

Figure 3.2: Classification models for tensile strength of bleached pulp; the spectra were collected using ATR-FTIR. Red circles show the data sets obtained using traditional methods (physically ripping samples apart using a force gauge), [50] and green stars show the predicted data sets, based on the ATR-FTIR spectra. Note the significantly lower RMSEP on the right-hand model.
Left: Model built using DWT and PLS; RMSEP= 0.42
Right: Model built using OSC-SVM analysis; RMSEP= 0.35.

industry has significant interest in the ability to predict these relevant parameters before or during manufacture, as they can significantly affect product quality, and ultimately, profit margins.

Of further interest to the forestry industry are the effects of the mountain pine beetle (*Dendroctonus ponderosae*) on the pulp and paper produced from infested trees. *D. ponderosae* infestations have caused significant damage to the forest resources of western North America. [47] In the British Columbia Interior, populations of lodgepole pine (*Pinus contorta* var. *latifolia*) have been severely affected by *D. ponderosae*. *P. contorta* var. *latifolia* is extremely important to the forestry industry, as it is the main constituent of Canadian Northern Bleached Softwood Kraft (NBSK) pulp, which is of significant economic importance both locally and nationally. [47–49]

To determine the predictive ability of Raman spectroscopy, several classification models were constructed for various parameters. The Raman data were analyzed using a variety of multivariate analyses and chemometric methods, such as Principal Component Analysis (PCA), Partial Least-Squares Regression (PLS), and

Template-Oriented Genetic Algorithm (TOGA). In some cases, the Raman-based classification models were compared to those built using NIR or ATR-FTIR-based data. [51] See Fig. 3.2 for an example of such a model. Though there is ample documentation of the use of NIR- and ATR-FTIR-based classification models for pulp and paper analysis in the literature, [52–58] the success of our Raman-based models was hampered by the instrumental limitations of the *RP-1* and *BX51* microscope. As mentioned previously, there were also difficulties related to sample mounting and Raman resolution. These limitations led to the development of the instruments that are the focus of this thesis.

3.3 Original Design Ideas

The original concept for an integrated iSCAT and confocal Raman microscope arose from the group's collaboration with partners in the pulp and paper industry. The design concept was an instrument that would allow a user to take an iSCAT image of a pulp sample, use it to localize individual fibers, then direct the confocal Raman probe to them directly.

An early design decision was the orientation of the objective. In most conventional light microscopes, the objective points town towards the sample stage, and the light source illuminates the sample from below. Such microscopes typically use broadband sources to produce brightfield or darkfield imagery. However, for iSCAT imaging, the illumination beam and signal beam are collinear, and therefore an inverted orientation where the objective points up to the sample is preferable. This maximizes ease of access to the sample, as well as keeping the optical train low to the table. The height of the optical train (from the surface of the optical table) is almost always determined by the height of the monochromator's entrance slit, which is generally fixed, on the order of several inches.

In order to implement the collinearity of the iSCAT and confocal Raman systems, a laser appropriate for both methodologies had to be selected. In this decision was a tradeoff; shorter wavelengths provide better spatial resolution for iSCAT, higher signal intensity for Raman, but compromise the ability to obtain a spontaneous Raman signal by greatly increasing sample fluorescence. [59, 60] Longer wavelengths, on the other hand, are more effective for spontaneous Raman mea-

surements despite decreasing signal intensity, but sacrifice iSCAT resolution by increasing the diffraction limit. [59, 61, 62] Additionally, reliably collecting spontaneous Raman emissions through a confocal pinhole requires an incredibly clean laser beam with a perfect spatial mode. A Helium-Neon (HeNe) laser was selected as the best solution to these requirements.

3.3.1 Designing an iSCAT System

We decided a single-channel iSCAT system using an autobalanced photoreceiver for a detector would best suit our needs. Such a design had been used to localize a single molecule of terrylene diimide adsorbed to a thin layer of poly(methyl methacrylate) (PMMA), [28] though that instrumental setup was substantially different from the instruments described herein.

Using an autobalanced detector would correct for fluctuations in the laser's power over time, thereby providing a more true-to-life iSCAT signal. However, the most important reason a single-channel iSCAT detector was chosen was because from the earliest moments of conception, iSCAT was intended to be fully integrated (i.e. collinear) with a confocal Raman system. This meant that wide-field iSCAT designs, using Acousto-Optic Deflector (AOD) units and a Complementary Metal-Oxide-Semiconductor (CMOS) camera, were entirely inapplicable. [28] These wide-field designs, however, were revisited later (see Ch. 5.1).

To understand how an autobalanced detector works, one must consider a basic differential amplifier. Such an amplifier reads two voltage inputs and outputs a single voltage, the latter being the difference between the two input voltages, such that:

$$V_{out} = g(V_{signal} - V_{ref}) \tag{3.1}$$

where g is the circuit gain, that is to say, the factor by which the amplifier amplifies the difference between the two inputs. The output, V_{out}, is termed the *differential signal*. The amplifier thus rejects the voltage range common to both the signal and reference inputs (V_{signal} and V_{ref}, respectively). [63] The autobalanced photoreceiver used in the instrument (model name *Nirvana 2007*, New Focus Inc., Santa

Clara, CA, USA) uses two photodiodes to convert optical power to current, which is then fed to differential amplifiers. Given the basic relationship of power, voltage, and current ($P = VI$), the *Nirvana* effectively converts the difference in optical power between the two inputs into a single output voltage. [64]

This differential signal output should theoretically be zero when the signal and reference inputs are identical; that is to say, when there is no sample for iSCAT to probe. Recall from Ch. 2.1 that iSCAT relies on the phase difference between light reflected from a coverslip and backscattered from a sample. The backscattered light will be out of phase with the reflected light due to the change in optical path length; this, in turn, is due to the different refractive indices of the sample and glass coverslip. [28] Thus, the optical power of the iSCAT signal read by the photodetector will vary with respect to the reference signal coming from the laser. This variance falls outside the common mode of the two signals, and thus is converted to V_{out} by the detector. If there is no discernible sample, then there is no optical path difference, and the signal and reference channels are effectively identical. However, in such a situation, the inescapable scourge that is shot noise rears its head, preventing V_{out} from truly reaching zero. Thus, the autobalanced detector is shot noise-limited. [64]

Any variability - or rather, instability - in the laser's output over time would also cause the signal beam to vary, which would be indistinguishable from actual refractive index-induced variance in the iSCAT signal. Using the autobalanced detector solves this potential problem, in that the variance would be detected on both the signal and reference channels. HeNe lasers are generally very stable, [65] but nonetheless environmental factors such as vibrations or humidity changes could cause some variation to occur.

In the instrumental design, the autobalanced photoreceiver collects a single channel of iSCAT data, through its two inputs (*Reference* and *Signal*). The *Nirvana*'s two physical outputs used to collect pertinent data are *Log Output* and *Signal Monitor*. They can be determined as follows:

$$\text{Log Output } (V) = -\frac{T}{273} * \ln \frac{P_{\text{reference}}}{P_{\text{signal}}} - 1 \tag{3.2}$$

$$\text{Signal Monitor } (V) = -10 * R * P_{\text{signal}} \tag{3.3}$$

where T is the circuit temperature in K, P is the optical power of the signal or reference photodiode in W, and R is the photodiode's responsivity, in A/W. [64]

A single, auto-balanced iSCAT channel was deemed most appropriate for this instrument, though this would prohibit video-rate viewing of samples. To facilitate integration with a high-precision confocal Raman branch, a single iSCAT channel that did not require the use of AOD units was ideal, as the AOD-induced beam motion would present a severe impediment to achieving confocality.

3.4 First Drafts

The earliest drafts of the instrument took on a substantially different form from the completed product. Figure 3.3 shows the cleaned-up original design, used to begin sourcing components; compare with Figure 4.1 to visually contrast this with the final product. The most striking element of the early designs that was eliminated was the raised breadboard that would have held the objective.

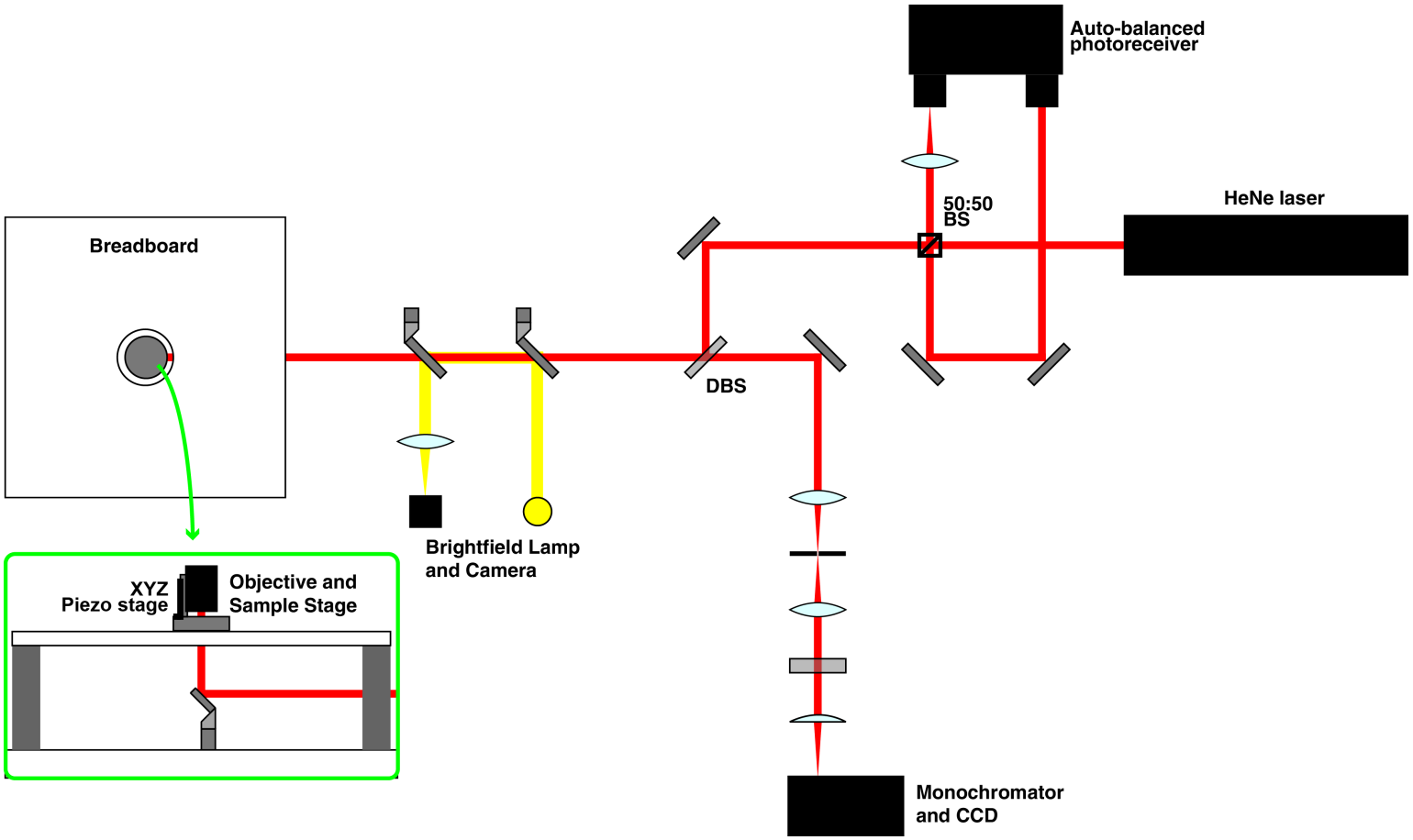

Figure 3.3: First Draft of the Single-Color Instrument.

This breadboard concept was conceived of as an easy way to create a fixed platform for the inverted objective and associated components. Mounting the breadboard at a fixed height several inches above the tabletop would ensure the high degree of stability necessary for maintaining the collimation of the objective beam. The breadboard was to be threaded to accommodate the objective in a fixed position over an angled mirror. This mirror would reflect the horizontal (i.e. parallel to the tabletop) illumination beam directly upwards into the objective. On top of the breadboard were to be mounted the piezo stage and sample holder; these components are by necessity independent from the objective.

Also included in the earliest designs was a system for brightfield imaging, represented by yellow lines in Fig. 3.3. This was to be implemented using an incandescent lamp for illumination, flip-down mirrors or beamsplitters, and a webcam-like CMOS camera, but was eventually scrapped. Brightfield imaging was resurrected later on, however; see the next section (Ch. 3.5) for more.

In order to obtain useful data, the system had to be designed in such a way that would allow a user to control where to collect data on the sample. Confocal Raman data vary most meaningfully between samples; a single spectrum is largely meaningless unless contextualized within a sample set.[1] As such, the important design factors for collecting Raman data are user-controlled positioning and ease of sample mounting. Conversely, iSCAT signals vary most meaningfully *within* samples. An iSCAT signal collected at a single point within a sample is *entirely* devoid of meaning, unless it can be compared with signals collected at neighboring points within the sample. To facilitate this, automated positioning becomes necessary, especially when considering the need for repeatable data collection. Using wide-field iSCAT imaging would obviate this problem (see Ch. 5.1), but the detector in this case is single-channel for reasons discussed previously.

To allow both user-controlled and automated positioning of the sample required two *xyz* stages: one with manual actuators and one with computer-controllable piezo drivers. In fact, a stage integrating the two was sourced and purchased (model

[1] Strictly speaking, this statement only holds true when the Raman data are being used to construct classification models, as described in Ch. 3.2. Since this is the general purpose of the instrument described herein, this can be accepted as a reasonable assertion. Single Raman spectra are indeed useful when attempting the identification of individual compounds, or classification of samples using a pre-existing model, neither of which are of relevance here.

no. *MAX312D/M*, Thorlabs, Inc., Newton, NJ, USA), along with a microscope slide holder. These together formed the sample mount. These components are described in more detail in Chapter 4.1.1.

Integrating the confocal Raman probe into this design was not especially challenging, given the prevalence of the methodology. Given their vastly different detection systems, the key step to integrating Raman spectroscopy and iSCAT was to effectively and efficiently separate the signal beam returning from the sample into its Raman and iSCAT components. This required finding an appropriate Dichroic Beamsplitter (DBS) that would reflect non-shifted light towards the iSCAT detector and transmit Stokes-shifted light towards the spectrometer. The Stokes-shifted light would then pass through a confocal pinhole, as per the typical design of confocal Raman systems. [33, 66]

3.5 Constructing the Instrument

This section outlines the instrument's construction process. The next chapter (Ch. 4) describes the instrument in general terms, and details how it was operated.

3.5.1 Hardware

Sourcing and pricing of the various components needed to construct the instrument began once the NSERC grant came through. In order to save money, some old equipment already present in the lab was used. Chief among these were the optical isolation table (manufactured by Newport Corp., Irvine, CA, USA), the spectrometer (model no. *SP 2150i*, manufactured by Acton Research Corp., Acton, MA, USA), the CCD camera (model no. *Spec-10*, manufactured by Roper Scientific Inc., Sarasota, FL, USA), and the computer (running Windows XP, manufactured by Dell Inc. (Round Rock, TX, USA)).

The components required for constructing the breadboard design outlined in the previous section (Ch. 3.4) were purchased as well, and the breadboard was threaded to mount the objective. At this point, however, it became apparent that the breadboard mount made adjusting the objective and tuning the laser beam so impractical as to be effectively impossible. A new objective mount was quickly devised: a 45° elliptical mirror mount, fitted with a thread adapter, mounted between

two optical posts. This was simple enough, and necessitated that the sample stage be elevated on optical posts as well.

Another design flaw, or more accurately, an inefficiency, was the design of the sample stage system itself. Originally, the manual and piezo actuators were to be separate entities. The system would have worked as follows:

- Sitting atop the breadboard would be a two-dimensional (xy) stage with a circular hole bored through the middle (model no. *122-0245*, OptoSigma, Santa Ana, CA, USA).[2] The stage came with two manual linear actuators, and was fitted to incorporate two standalone piezoelectric actuators (model no. *AE0505D16F*, Thorlabs Inc., Newton, NJ, USA).
- A 90° L-bracket would then be attached to the 2D stage.
- A one-dimensional (z) stage (model no. *NFL5DP20/M*, Thorlabs Inc.) would then be attached to the vertical face of the L-bracket. This stage incorporated both a manual and a piezoelectric actuator.
- The two standalone (xy) piezo actuators and the integrated (z) piezo actuator were to be driven by a 3-axis open-loop piezo controller (model no. *MDT693A*, Thorlabs, Inc.).
- A slide holder was to be designed and fabricated, in order to be attached to the vertical (z) stage.

This design proved to be needlessly complicated. Furthermore, there were a number of difficulties in getting the standalone piezo actuators to work with the xy stage. Modifying the stage to accommodate the actuators proved far more challenging than anticipated, so much so that they could not be relied upon to move the stage repeatably, if at all. On top of this, the L-bracket proved to be more unstable than anticipated. A fork-like piece of aluminum was milled to give the L-bracket more stability, but it made positioning the vertical z stage with respect to the objective much more difficult.

Eventually, the entire multi-part design was scrapped in favor of a self-contained but much more expensive unit (model no. *MAX312D/M*, Thorlabs Inc.). This unit

[2] This hole was the factory design, not after-market.

featured three manual linear actuators as well as integrated three-dimensional piezo actuators, and was compatible with the piezo controller we had already purchased. In addition to the new stage, a new, more stable slide holder was purchased (model no. *MAX3SLH*, Thorlabs Inc.). After these design flaws were corrected, construction proceeded smoothly.

After the system was constructed, the next step was to align the HeNe laser, and test its performance for spontaneous confocal Raman spectroscopy. This was done using a sample of diamond, which produces a very sharp peak. During testing it quickly became apparent that the random polarization of the laser was significantly hindering performance. The laser was exchanged for its polarized equivalent, at the cost of a slightly lower output power (model no. *HNL225R*, 22.5 mW vs. model no. *HNL210L*, 21.0 mW, both manufactured by Thorlabs Inc., Newton, NJ, USA). The performance of the linearly polarized model was deemed to be acceptable.

Another problem that surfaced during the construction of the instrument was a defect in the piezo controller unit, which was unable to vary the voltage on the z-axis piezo driver. The problem was resolved after two RMAs, and with the working controller in hand, the software needed to operate the instrument could finally be coded.

3.5.2 Software

The software was coded using LabVIEW 2012 (National Instruments, Austin, TX, USA). LabVIEW uses a proprietary graphical dataflow programming language called *G*; each program coded in *G* is referred to as a Virtual Instrument (VI), and for this instrument, two VIs were created. The first VI was originally designed to test the autobalanced photoreceiver, but was adapted to serve as a calibration program to ensure that iSCAT signals would be read correctly. The second VI was the instrument's user interface, containing all the necessary functionalities to collect data. For a description of how to use the user interface, see Ch. 4.2.

To interface with the relevant hardware, namely the autobalanced photoreceiver and the spectrometer, the LabVIEW VIs relied upon two separate driver suites. To read Raman data from the spectrometer, the VI used a third-party suite of drivers known as the Scientific Imaging Toolkit (SITK), which specializes in communica-

tion between Acton (Acton, MA, USA) and Princeton Instruments (Trenton, NJ, USA) hardware and LabVIEW software. To read iSCAT data from the autobalanced photoreceiver, a USB-powered Data Acquisition (DAQ) card was used (model no. *NI USB-6210*, National Instruments Inc., Austin, TX, USA); the DAQ card had native LabVIEW support, as they are both developed by the same company.

The iSCAT calibration VI was designed simply to display raw output from the autobalanced photoreceiver's log output (i.e. autobalanced signal) and signal monitor (i.e. reference) channels. While this did not display data in any useful capacity, it was designed to show whether the signal beam was properly attenuated relative to the reference beam. This was a requirement for reliable data collection; the signal beam should be roughly half as powerful as the reference beam, in order for the photoreceiver's differential amplifier to effect the best common-mode rejection. [64]

As part of its software suite, SITK provides a number of example VIs; one of these was used as the basis for the instrument's user interface. This example VI was intended for use with basic spectroscopic applications; it featured simple spectrometer controls and data viewing functionality. The VI was less robust than Princeton Instruments' proprietary spectroscopy software, WinSpec; the latter was used for alignment of the confocal Raman branch of the instrument, but could not be integrated with LabVIEW-based iSCAT functionality.

The VI's main functions were organized into tabs; one for initializing the CCD camera, one for selecting a Region of Interest (ROI) on the CCD, one for moving the spectrometer's grating turret, one for performing simple background subtractions, and two for collecting data (live spectra display and single spectrum collection). The functions in these tabs allowed the user to make the necessary adjustments before any data collection would begin, in order to ensure the data set's integrity. This included the live spectra display tab, which was used for Raman focusing operations where data storage was unnecessary.

The example VI's basic spectroscopic functions were augmented by integrating iSCAT functionality. The basic process for collecting iSCAT data was to set up a raster scan, record the photoreceiver's log output, then raster the piezo drivers. The raster was either done as a stack of horizontal *xy* planes, or a stack of vertical *xz* planes, with user-set distances and number of steps. These two values controlled

the resolution of the resulting iSCAT map, though there were also instrumental limitations; see Figs. 4.2 and 4.3 for a practical example of this instrumental resolution limit.

Raman data collection could also be incorporated into the aforementioned raster scan routines. Thus, at each point in the scan, the software would collect a point of iSCAT data and a Raman spectrum, then compile both into maps. Further, there was also an option for Raman-only raster scans.

A third piece of software was needed to facilitate the joint viewing of the collected iSCAT maps and Raman spectra. This VI was designed to visually unify the two data sets; it displayed both the iSCAT map and a Raman heatmap for a selected wavelength, as well as the complete Raman spectrum for any point selected on the map. It also incorporated some simple data processing functionalities, such as DWT and Second-Derivative Variance Minimization (SDVM). See Appendix A for images of the VI's front panel and block diagram, as well as examples of the VI in use.

With all the software in place, the instrument was deemed to be in working order and was ready to be tested. This was done using a variety of samples, some examples of which can be seen in the next chapter.

Chapter 4

The Original Design

This chapter describes the design and use of the instrument in its original single-channel configuration, used for both Interferometric Scattering Microscopy (iSCAT) and Raman microscopy. Refer to Fig. 4.1 for a schematic diagram of the instrument. The glossary contains definitions for the abbreviations used in Fig. 4.1.

4.1 Description of the Instrument

The first part of this section describes the line-of-sight propagation through the instrument, mentioning only key optics, followed by a list of important hardware and some of their properties.

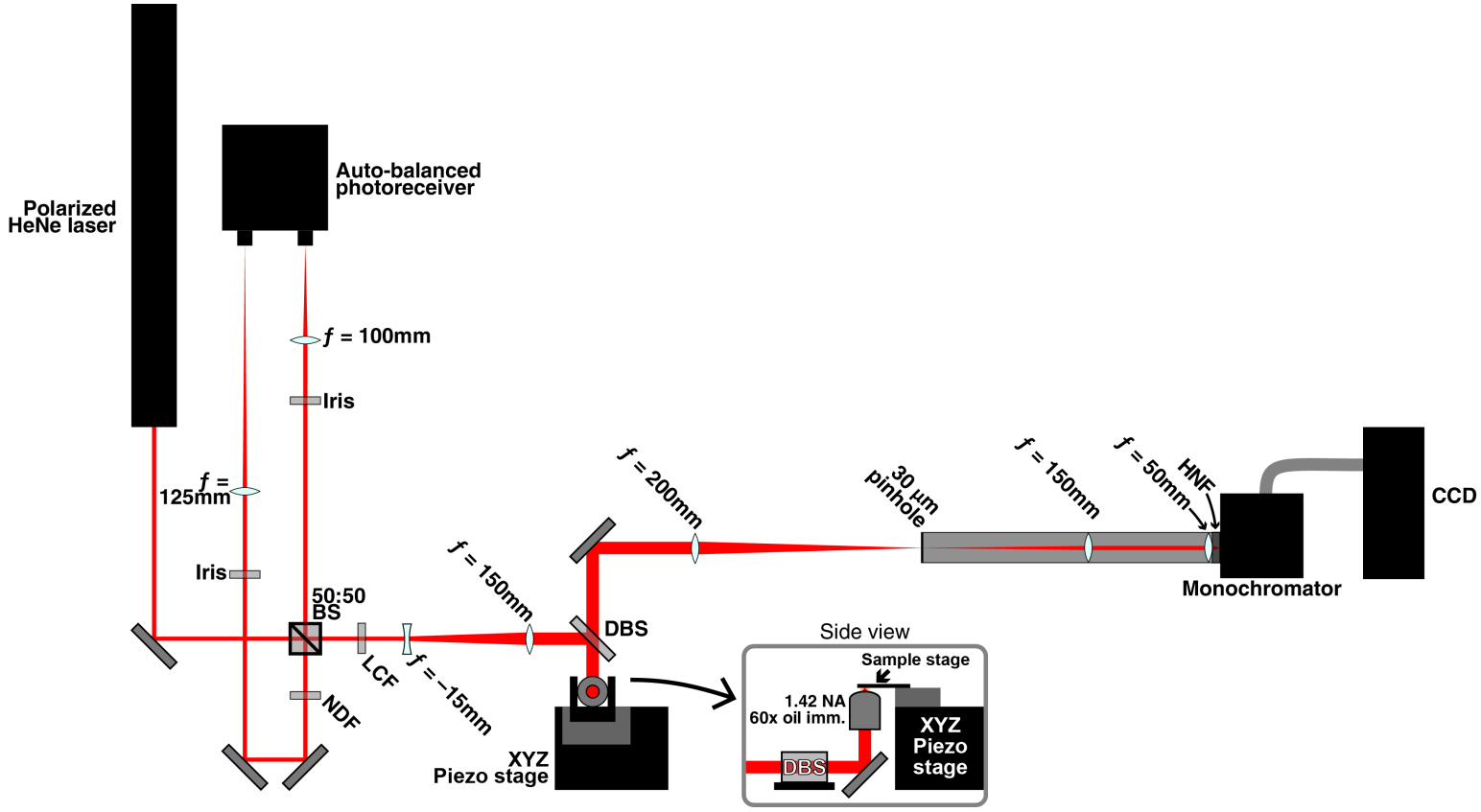

Figure 4.1: Diagram of the Instrument's Original, Single-Channel Configuration.

4.1.1 Description of Optical Train

After exiting the laser, the beam first met a 50:50 Beamsplitter Cube (50:50 BS); half of the beam was split off and directed through a variable Neutral Density Filter (NDF) towards the *Reference* channel of the photoreceiver (see Ch. 3.3.1 for more details on the photoreceiver). The light passing through the beamsplitter next passed through a Laser Clean-up Filter (LCF), and then was expanded and reflected off a longpass Dichroic Beamsplitter (DBS) towards the objective and sample. The beam expansion optics enlarged the beam to completely fill the objective's aperture. The sample was held in place above the objective upon a 3-axis open-loop piezo stage with integrated manual actuators. After returning from the sample, the signal beam again met the DBS; at this point, the iSCAT and Raman beams diverged. Rayleigh-scattered light (i.e. light of the same wavelength as the laser) was reflected back towards the 50:50 beamsplitter, where it then was directed into the *Signal* channel of the photoreceiver; this provided the iSCAT signal. Raman-scattered light (i.e. Stokes-shifted, of higher wavelength that he laser) passed through the DBS and was directed through a 30 μm confocal pinhole, through a Holographic Notch Filter (HNF), and into the monochromator; this provided the Raman signal.

4.1.2 List of Major Components

- Microscope objective: oil immersion, infinity-corrected, planar apochromatic; model name *PLAPON60XO*, manufactured by Olympus Corp., Shinjuku, Toyko, Japan

  Magnification: 60x

  Immersion oil refractive index: $n = 1.518$

  Numerical Aperture (NA)=1.42

  Working distance: 0.15 mm

- Autobalanced photoreceiver for iSCAT: model no. Nirvana *2007*, manufactured by Newport Corp., Irvine, CA, USA

  Detector: 2x PIN diode

  Detector diameter: 2.5 mm

Noise-equivalent Power (NEP): 3 pW/$\sqrt{\text{Hz}}$

Peak responsivity: 0.5 A/W

Common mode rejection: 50 dB

- HeNe laser: model name *HNL225R*, manufactured by Thorlabs, Inc., Newton, NJ, USA

  Emission wavelength: 632.8 nm

  Maximum output power: 21.0 mW

  Polarization ratio: 500:1

- Piezo stage (incl. drivers): model name *MAX312D/M*, manufactured by Thorlabs, Inc.

  Manual range: 4 mm (coarse), 300 μm (fine)

  Piezo range: 20 μm

  Theoretical resolution: 20 nm

  Accuracy: 1.0 μm

- Piezo controller (open-loop): model *MDT693A*, manufactured by Thorlabs, Inc.

  Voltage range: 0 to 75 V

- Monochromator: model *SP 2150i*, manufactured by Acton Research Corp., Acton, MA, USA

  Focal length: 150 mm

  Aperture ration: f/4

  Gratings: 600 g/mm, 1200 g/mm

  Grating blaze wavelength: 750 nm

  Spectral resolution: 0.4 nm (1200 g/mm grating)

- CCD detector: model *Spec-10 XTE-100B*, manufactured by Roper Scientific Inc., Sarasota, FL, USA

Chip size: 1340x100 px

Pixel size: 20 μm

Dark current: 0.0005 e^-/p/sec

Spectrometric well capacity: 250 ke^- to 1 Me^-

Read noise: 3.5 e^- RMS

Chip type: forced-air cooled, back-illuminated thermoelectric

Typical operating temperature: -90 °C

4.2 Using the Instrument

The following is a generalized outline of the procedure used to collect and view data using the instrument.

Preparation of samples was no different from any conventional optical microscope: the sample was laid on a glass slide, and covered with a thin glass coverslip. The objective required a dab of immersion oil to be placed on the coverslip; then, the sample slide could be put in place, upside down, in the sample holder.

The next step was to calibrate the iSCAT system using the Virtual Instrument (VI) mentioned in the previous chapter (Ch. 3.5.2). To perform the calibration, the objective was moved to a "blank" area of the sample (i.e. so the focal point was moved off the sample and into the glass). Then, the NDF on the reference beam (see Fig. 4.1) was adjusted so that the readout in the VI was close to zero. This ensured that the background signal was half as intense as the reference signal, and that therefore the photoreceiver's autobalancing circuitry would correctly record the interference pattern in the signal beam that characterizes iSCAT.[1] Adjusting the NDF was straightforward, as the filter itself was linearly graded between 0.01% and 91% transmission;[2] thus, adjusting the filter was simply a matter of moving it horizontally with respect to the beam.

After the iSCAT signal was calibrated, the spectrometer was initialized using the main VI, also mentioned in the previous chapter. Once the experimental parameters

[1] See Ch. 2.1 for a more thorough explanation of the principles of iSCAT.

[2] Optical density between 0.04 and 4.0; $T = 10^{-OD}$

(exposure time, number of frames to collect, etc) were written to the spectrometer, and it became sufficiently cool, data could be collected as desired. This required programming scan parameters for the piezo controller. At each point along the scan, the system would record an iSCAT value and a Raman spectrum; the VI could also be set to only record either iSCAT or Raman, though this made it more difficult to correlate the two data sets. The User Interface (UI) displayed the latest Raman spectrum and would auto-update an iSCAT map, so that the latest value could be visualized in context. All data were stored in Text Array (TXT) files.

The data was best visualized using MATLAB or the Raman Map Reader VI (Appendix A). The latter allowed the user to correlate iSCAT and Raman data, as well as apply some basic processing (Discrete Wavelet Transform (DWT), Second-Derivative Variance Minimization (SDVM)) to the Raman data; however, it was a visualization tool only. Data processing methods are discussed in more detail in Ch. 8.2.

4.3 Limitations and the Need for More

With the single-channel design completed, routine sample imaging began in earnest, both to see what how the instrument worked and to probe any unforeseen complications. There are several examples of collected data in this chapter.

4.3.1 Resolution

Two of the inherent difficulties with building iSCAT maps in the method used by this instrument, i.e. using a single-channel detector and rastering the sample, can be seen in Figs. 4.2 and 4.3. Both are maps of the same sample of sea spray aerosol particles. The map on top (Fig. 4.2), a 20x20 μm field of view, consists of 3,600 data points. Nonetheless, the resolution is limited, because of the relatively large step size of 333 nm; thus, only the larger particles are clearly visible.

This was a common problem with mapping samples, as it was difficult to ascertain both whether a sample was in focus and whether it contained any visible data. A large overview map of a sample may not show small features, while a small, zoomed-in map may miss features in other areas. The lack of live video display also made it difficult to determine whether the sample was in focus. Instead, Ra-

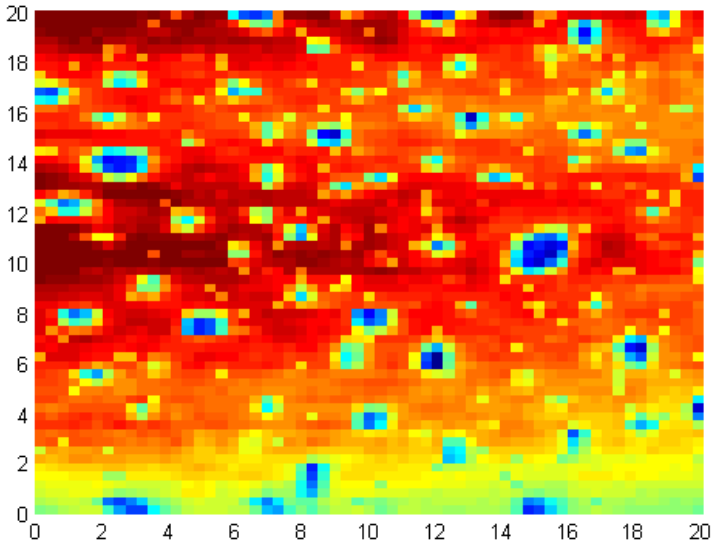

Figure 4.2: A 20x20 μm, 60x60 step single-channel iSCAT map of sea spray aerosol particles, demonstrating the user-determined resolution limit, determined by step size. Collection time was approximately 45 minutes. *Sea spray aerosols are predominantly composed of sodium chloride, and are collected using a cascade impactor. The size distribution is non-uniform.*[67]

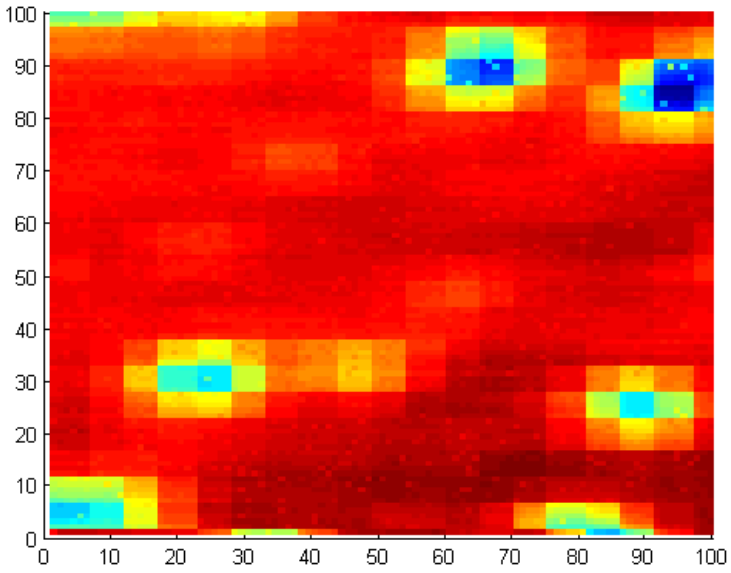

Figure 4.3: A 5x5 μm, 100x100 step map of the same sample, demonstrating an instrumental resolution limit of around 300 nm. Collection time was approximately 2 hours.

man was sometimes used to focus the sample, but only in Raman-active samples. As many samples lack strong spontaneous Raman spectra, this was often impossible, so a workaround was devised. Focusing the light reflected from the cover slip onto the confocal pinhole was adequate for iSCAT mapping.

The lower map (Fig. 4.3), a 5x5 μm field of view, consists of 10,000 data points; it shows a clearly-defined resolution limit. This is in fact an instrumental limit: though each step is larger the piezo driver's theoretical resolution, the image shows data in "blocks" of 6x6 pixels, or about 300 nm to a side. This limit is the Abbe diffraction limit, calculated as follows:

$$d = \frac{\lambda}{2n\sin\theta} = \frac{\lambda}{2 * \mathrm{NA}} = \frac{632.8\ \mathrm{nm}}{2 * 1.42} = 222.8\ \mathrm{nm} \tag{4.1}$$

Thus, the 300 nm resolution in Fig. 4.3 is slightly higher than the Abbe diffraction limit (222.8 nm) for the instrument. This limit is smaller than the step size in 4.2, so it is not observable in that map.

The discrepancy between the actual Abbe diffraction limit and the observed instrumental limit is likely due to the piezo driver; since the piezo controller is open-loop, this presented a certain degree of uncertainty - specifically, an absolute uncertainty of 1 μm - in the piezo actuators' physical positions. Thus, maps with a step size smaller than that figure had to be viewed with a degree of caution, even if they appeared accurate.

4.3.2 Time Investments

To draw again on the aerosol examples (Figs. 4.2 and 4.3), both iSCAT maps required serious time investments to collect. Collecting an individual iSCAT data point is trivially fast; however, stringing together hundreds or thousands of points, plus rastering the piezo drivers, greatly increases the collection time. The 3,600-step image (top) took about 45 minutes to collect, whereas the 10,000-step image (bottom) took approximately two hours; thus, collecting iSCAT data took approximately 750 ms per step.

When it comes to collecting Raman data, time is an even more serious concern. Since the probability of spontaneous Raman scattering is so low, [68, 69] a long

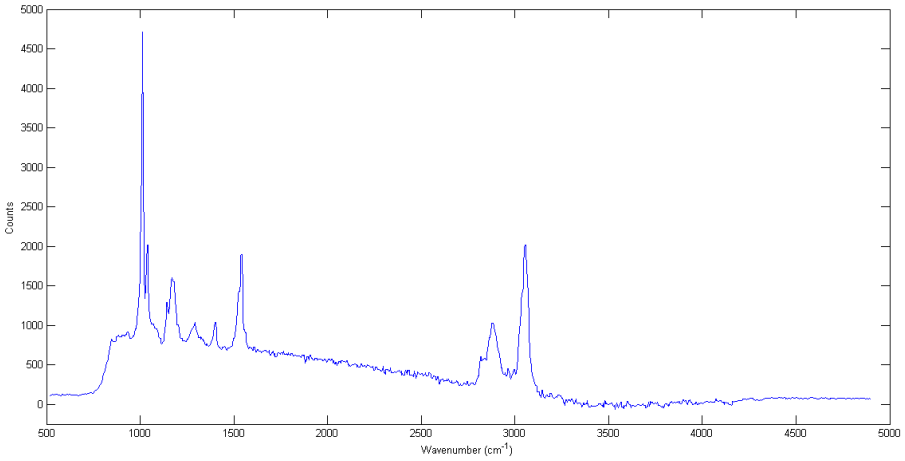

Figure 4.4: Raman spectrum of polystyrene bead (see also Figs. 8.3, A.1, and A.2). Collection time: 45 sec. The spectrum has been processed using SDVM and a median filter.

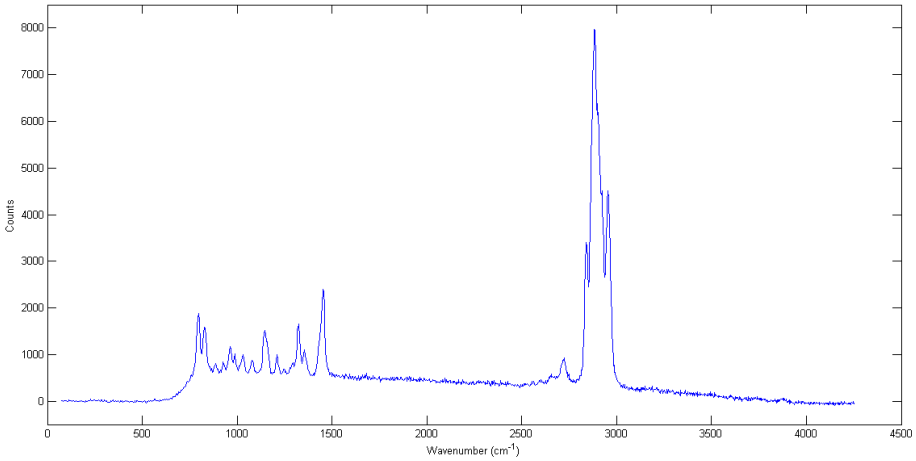

Figure 4.5: Raman spectrum of polypropylene resin, from a cottage cheese tub. Collection time: 20 sec. The spectrum has been processed using SDVM and a median filter.

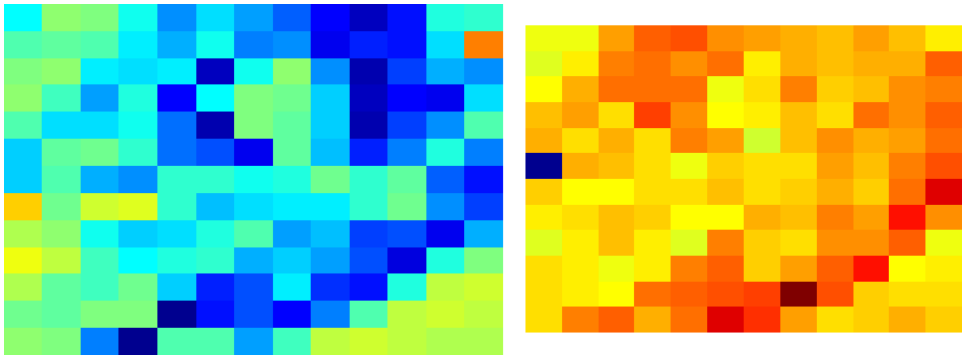

Figure 4.6: Data set showing of thin slices of plasticized pig brain mounted in a TEM grid.
Left: Cropped single-channel iSCAT map, approx. 15x15 μm. See Fig. 5.2 for the full map.
Right: Map of principal component 2 based on collected Raman spectra, processed using PCA. PC2 accounts for 7.50% of the variance in the Raman data set, and shows a complementary spatial distribution to the iSCAT image. *PC2 was chosen over PC1, as the latter represented the contribution of the TEM grid to the overall variance (see Fig. 5.2).*

exposure time must be used in order to collect a useful spectrum. This "useful" exposure time is at a minimum 15 seconds, and often several minutes (see Figs. 4.4 and 4.5). When hundreds or thousands of collections were strung together to make a map, as with (and often alongside) iSCAT, data collection on a single sample map could run for dozens of hours.

For example, the full iSCAT map shown in Fig. 5.2,[3] along with the accompanying Raman data with an exposure time of 25 seconds per point, took approximately three hours to collect; the Raman collection was clearly the limiting factor. Bear in mind that this map consisted of only 400 steps; the examples from Figs. 4.2 and 4.3 are orders of magnitude larger, and as such, had they had accompanying Raman data acquisition, would have taken days to collect.

[3] See also Figs. 4.6, A.1, and A.2.

4.3.3 Moving Forward

Because of these challenges - especially because of the time requirements - we began to consider alternative designs to improve the instrument's performance. The key change was to convert the iSCAT system from a single-channel detector to a wide-field detector, an idea previously mentioned in Ch. 3.3.1. This wide-field channel would mean that iSCAT data collection would no longer be vinculated to Raman data collection. These upgrades, and other design refinements, are discussed in the next chapter.

Chapter 5

Upgrading to Wide-Field

After the completion of the instrument in its single-channel configuration, we recognized a number of new challenges. Routine use of the instrument pointed to a number of possible refinements that would resolve some issues and improve its performance. The biggest refinement was the introduction of a wide-field iSCAT system, which is detailed in this chapter.

5.1 Wide-Field iSCAT: How and Why

The key bit of engineering that was required for the instrument's major upgrade was the design of the new, wide-field Interferometric Scattering Microscopy (iSCAT) channel. While iSCAT imaging is a relatively novel technique, wide-field imaging is not. [9, 70–74]

Simply replacing the photoreceiver with a wide-field detector such as a Complementary Metal-Oxide-Semiconductor (CMOS) camera is not possible, because the detector cannot elucidate localization information from the signal it receives. There are a number of ways to get around this problem, many of which involve interferometry of one kind or another. In fact, this is the key ability of interferometry: extracting recondite data from an otherwise useless signal. In the case of iSCAT, the recondite data in question is the variation in refractive index within a sample (see Ch. 2.1). Simply collecting all the backscattered light from the sample will not indicate where in the sample the scattering occurred.

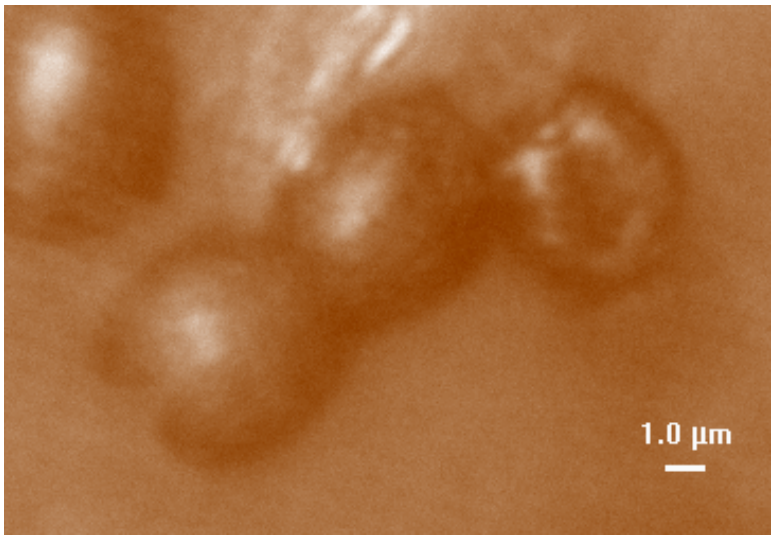

Figure 5.1: Cropped iSCAT image of four conidia - asexual spores - from the powdery mildew fungus *Microsphaera vaccinii*, imaged *in situ* on a dried leaf (*Vaccinium sp.*), collected in the Nanaimo River valley (BC, Canada). False color; field of view approx. 19 by 13 μm.

One way to obtain such localization information is to introduce a pattern along the optical train, either just before the sample or just before the detector; this technique is commonly referred to as structured illumination. By using a known illumination pattern, any perturbations to that pattern caused by a sample can be recorded and reconstructed into images. This produces a wide-field image, since the light pattern is observed all at once. [8, 70] Thus, through the interference caused by perturbing the illumiation pattern, localization information can be mathematically obtained. Structured illumination, however, would not be suitable for iSCAT measurements, as it would be highly challenging to set up a reference beam for the necessary scattering interference measurements.

An alternative approach to wide-field iSCAT that eschews further interferometry is to physically reposition the illumination beam as it enters the objective in a controlled fashion, thus moving the location of the focus point on the sample. In effect, this mechanically introduces localization information into the beam, by varying where the beam strikes the sample while also varying where it strikes the sensor. Such beam motion could introduced using Acousto-Optic Deflector (AOD)

units or galvanometric mirror sets. This methodology has found use in various applications, including an iSCAT experiment. [24, 28] We chose this approach, especially considering there was literature precedent of a wide-field iSCAT experiment using AODs.

5.1.1 Advantages of Wide-Field Imaging

One of the biggest advantages of wide-field imaging is its instantaneity: iSCAT data can be observed in real-time. This is a huge advantage over single-channel detection; there is no longer a need for lengthy mapping, and no longer any question about whether a sample is in focus, or indeed whether it is even visible in iSCAT before making a time commitment.

In the same vein, wide-field imaging allows the user to see and record the entirety of the sample - or at least as much of it as the optics physically allow - all at once. In addition to the aforementioned benefits, this video-rate data collection provides much more flexibility in how the data are stored. iSCAT images can be stored as Text Array (TXT) files as before, but also as image files and even video files. Chapter 8.1 contains more details on the variety of iSCAT data collection possibilities.

Figure 5.2 provides an example of the stark difference between wide-field imaging and single-channel mapping. Both images show plasticized pig brain slices mounted in a TEM grid, as in Fig. 4.6. Both images also show the TEM grid itself, on the top and left margins, for comparison. The top image, a map recorded using the single-channel configuration, took 5 minutes to collect,[1] and was reconstructed using MATLAB. The bottom wide-field image was collected in 22 ms,[2] and shows a substantially larger area, even though its size has been cropped.

When it comes to using iSCAT data to identify potential regions of interest for Raman data collection, the advantages of wide-field iSCAT become even clearer. Data processing time decreases by orders of magnitude, and even simply locating regions becomes easier. Collecting a Raman map is still advisable for some sam-

[1] This stated collection time is calculated based on iSCAT-only collection speed of about 80 steps per minute (see Fig. 4.3). The actual collection time for this map was three hours, due to 25 sec. Raman spectrum collection at each point.

[2] The framerate the CMOS camera used to collect the image is 45 Frames per Second (FPS).

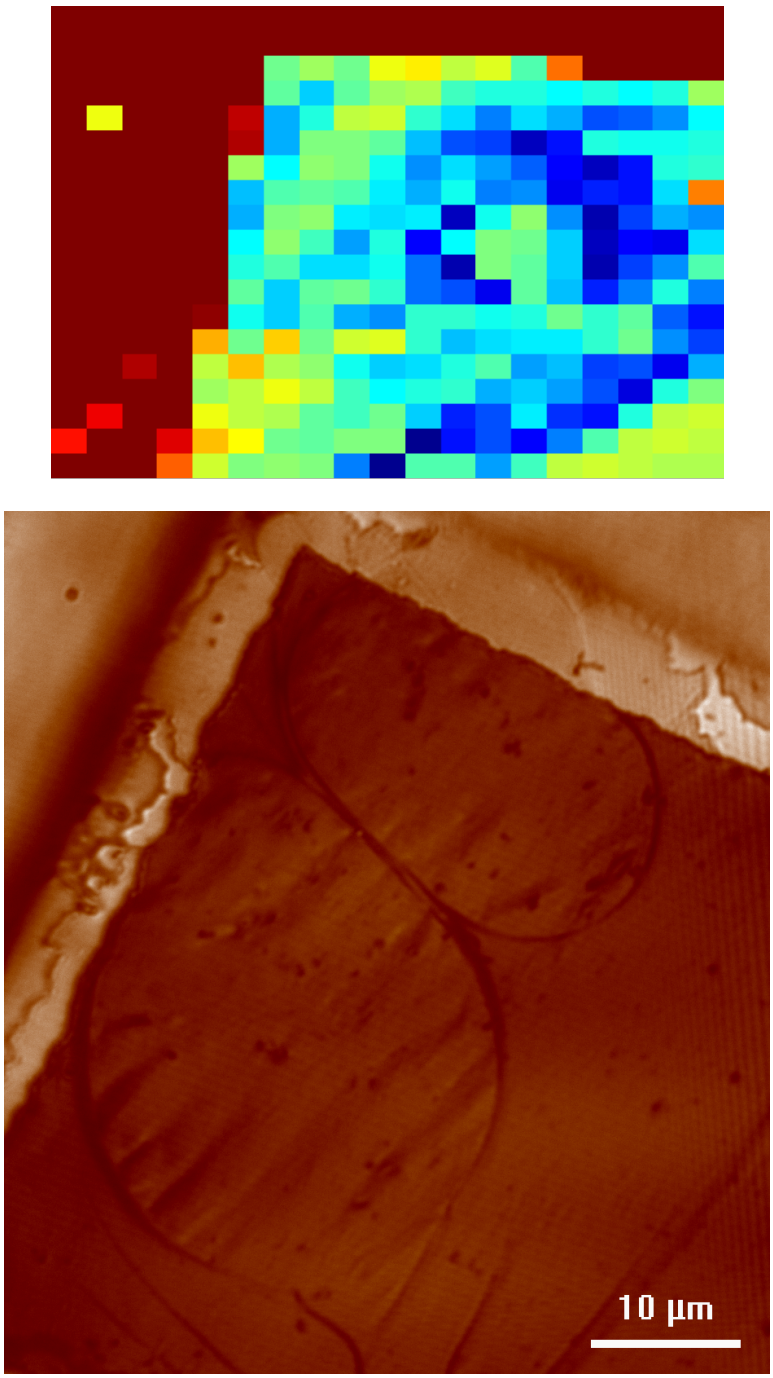

Figure 5.2: iSCAT images of thin slices of plasticized pig brain mounted in a TEM grid; see also Fig. 4.6. The images are not to scale. *(Note: the images are of different cells in the same TEM grid.)*
Top: Approx. 20x15 μm map, taken using old single-channel configuration (Ch. 4).
Bottom: Approx. 60x80 μm image, taken using new wide-field configuration (Ch. 5), with false color.

ples, but using the wide-field iSCAT image, the user can be far more judicious about where to move the Raman probe on the sample.

5.1.2 The Acousto-Optic Beam Deflector

The implementation of the wide-field iSCAT system depends on the use of AOD units. In brief, an AOD consists of a tellurium oxide (TeO_2) crystal attached to a lithium niobate ($LiNbO_3$) piezoelectric transducer. The transducer is fed a radiofrequency signal from a Voltage-Controlled Oscillator (VCO). This signal causes the transducer to expand and contract on a MHz frequency; this oscillation causes propagation of shear waves in the crystal along its (110) plane. The modular deformation of the crystal lattice changes the diffraction angle of light passing through the crystal, causing it to be linearly rastered at a high frequency.

The deflection angle θ_d, in other words the difference between the maximum and minimum diffraction angles, can be calculated as follows:

$$\theta_d = \left(\frac{\lambda_{\text{light}}}{V}\right)\lambda_{\text{RF}} = \left(\frac{632.8\text{ nm}}{0.66\ \frac{\text{mm}}{\mu\text{s}}}\right)\lambda_{\text{RF}} \tag{5.1}$$

where λ_{light} is the wavelength of incident light, in this case 632.8 nm, V is the acoustic velocity in the crystal, in this case 0.66 $\frac{\text{mm}}{\mu\text{s}}$ for TeO_2, and λ_{RF} is the radiofrequency input. In the case of the AODs purchased for use in the new wide-field configuration, the deflection angle θ_d is approximately to 56 mrad, or about 3.2°, before beam expansion.

However, since there is only one transducer per crystal, individual AODs can only raster a beam one-dimensionally. Producing a wide-field image necessitates two perpendicular AODs, one to raster over the x axis, and the other to simultaneously raster over the y axis, forming a rectangular pattern. Such an arrangement presents a problem, however; if the VCO-produced radiofrequencies are identical, the beam will simply be rastered along a diagonal line ($y = x$). Thus, the radiofrequencies need to be slightly offset from one another.

The function generators have four preset waveform outputs: sawtooth, sine, triangle, and square, and simulations were constructed in MATLAB to determine which would provide the most uniform coverage of the image plane. Figure 5.3

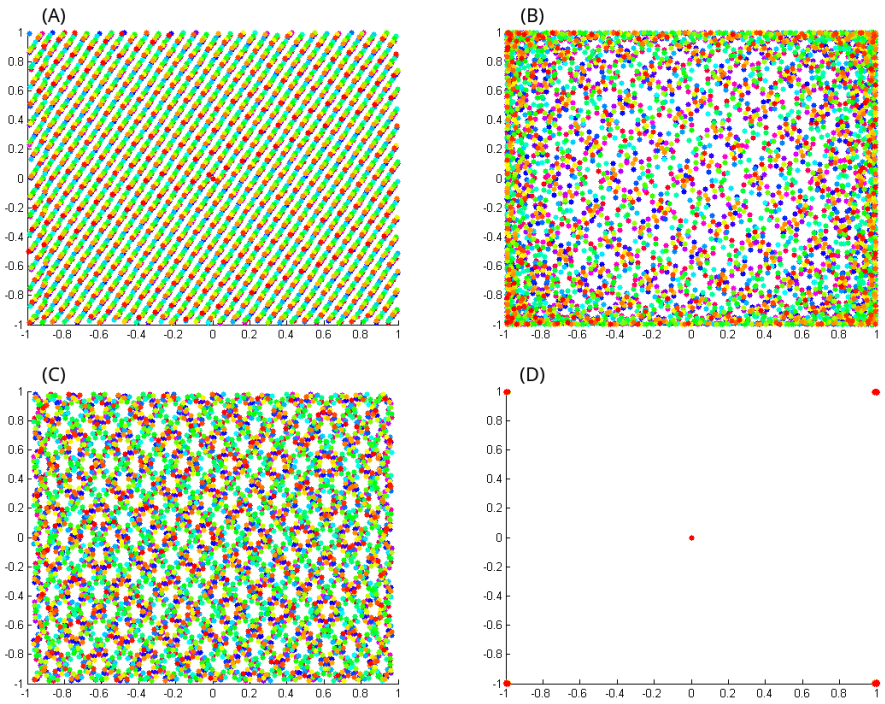

Figure 5.3: MATLAB simulations of AOD raster patterns. Point color represents location of beam over time; red is at $t = 0$. See also Fig. B.1.
A: Sawtooth wave.
B: Sine wave.
C: Triangle wave.
D: Square wave.

shows the results; see Appendix B for the simulation code, as well as experimental observations. Subfigure *A*, top left, shows the sawtooth output, and clearly provides the most uniform coverage of the arbitrary area. Subfigure *B*, top right, shows the sine wave output, which is noticeably sparse in the middle and concentrated in the corners, due to the shape of the trigonometric function. Subfigure *C*, bottom left, shows the triangle wave output, which although it uniformly covers the area, forms a diamond pattern that leaves significant gaps. Subfigure *D*, bottom right, shows the square wave output. Clearly, the latter is entirely unsuitable, as it points only to the corners (and to the center point at $t = 0$); this is due to the binary nature of the square wave. Based on the simulations, the sawtooth function was deemed the best

option, but experimental results showed the triangle function to be slightly better (see Fig. B.1).

5.1.3 Implementing the Wide-Field Channel

With the wide-field iSCAT design nailed down, we began implementing the upgrades. Figure 6.1 shows the design of the fully upgraded instrument. On that figure, both the PtGrey[3] and Thorlabs[4] cameras have CMOS sensors. The AOD units were purchased from Gooch & Housego plc (Ilminster, UK).

Getting the collinear wide-field iSCAT and confocal Raman channels operational required a convenient way for the user to switch between operating modes. This was achieved by changing the output of the function generators, thus changing the behavior of the AOD units. As discussed previously, for wide-field iSCAT data collection, the function generators must be outputting waveforms with similar (but not identical) frequencies in order to raster the beam over the sample. For confocal Raman data collection, on the other hand, the beam must *not* be rastering. The beam travels through the AOD crystals regardless, and the crystals will diffract the beam even when unpowered; however, the diffraction angle depends on the voltage input, as per Eq. (5.1). Thus, to maintain alignment, the beam must pass through the crystals while they are receiving a constant voltage equal to the average voltage they receive during iSCAT data collection. That is to say, the function generators must be set to output waveforms with amplitudes of 0 V, i.e. a constant voltage. That adjustment can be made on the front panel of the function generators, and as such, switching between iSCAT and Raman modes on the instrument is straightforward.

5.1.4 iSCAT Beating

A problem that is routinely encountered during wide-field iSCAT imaging is an interference pattern observed in the image. The pattern does not entirely disrupt the ability to collect data; however, it is pernicious enough to merit attention. Since wide-field iSCAT imaging is simulated by using point illumination rastered over a

[3]Point Grey Research Inc., Richmond, BC, Canada
[4]Thorlabs Inc., Newton, NJ, USA

sample using the AOD units, at a rate near 40 kHz, it creates the illusion of a wide-field image.[5] In fact, the redraw rate of the iSCAT image (i.e., the time it takes for the beam to raster over the entire image) is perceptible by the iSCAT camera's CMOS sensor. This is directly analogous to a very common problem: the 60 Hz refresh rate of most Cathode Ray Tube (CRT) screens interferes with the standard 24 FPS capture rate used by the film industry. Thus, CRT screens often appear to be flickering when captured on film.[6]

Exactly the same effect occurs in the iSCAT case. When faced with the high power of the laser, the camera adjusts the CMOS sensor's exposure time to become so short as to interfere with the iSCAT redraw rate, even at relatively low laser powers (around 100 mW). The iSCAT redraw rate is around 13.5 kHz, or once per 74.1 μs. The camera's exposure time ranges between 32 μs and 22 ms; when capturing bright laser light, it is typically less than 100 μs. Thus, when the exposure and redraw rate interfere, they form a beating pattern.

In the case of most CRT screens captured on film, the beat frequency is 36 Hz; this is highly perceptible to the human eye. In the case of the iSCAT camera, the frequency is variable due to the camera's rapid automatic exposure time adjustments. If the exposure time is faster than the redraw time, then each captured frame will be incompletely illuminated. For example, at 60 μs exposure, each frame is 80% illuminated. Because the redraw frequency is independent of the framerate, the illumination begins at a different point on the field of view for each frame. Thus, the incompletely illuminated area appears to oscillate across the frame. When strung together at the default 45 FPS framerate, this oscillation beats with the latter.

To combat this beating, a Neutral Density Filter (NDF) was installed to attenuate the laser's power before the illuminating beam reaches the objective, and again before the signal beam reaches the camera. However, the former NDF significantly impedes the spectrometer's ability to observe spontaneous Raman signals, and thus must be removed for confocal Raman detection.

[5] See Chs. 5.1 for more information on wide-field iSCAT imaging.

[6] This problem occurs with traditional photochemical film stock, as well as with the CMOS sensors found in modern digital cameras.

Chapter 6

The Finalized Design

This chapter describes the design and use of the instrument in its final wide-field configuration, as well as some of the challenges it faces.

Figure 6.1 shows the finalized design for the new wide-field configuration.

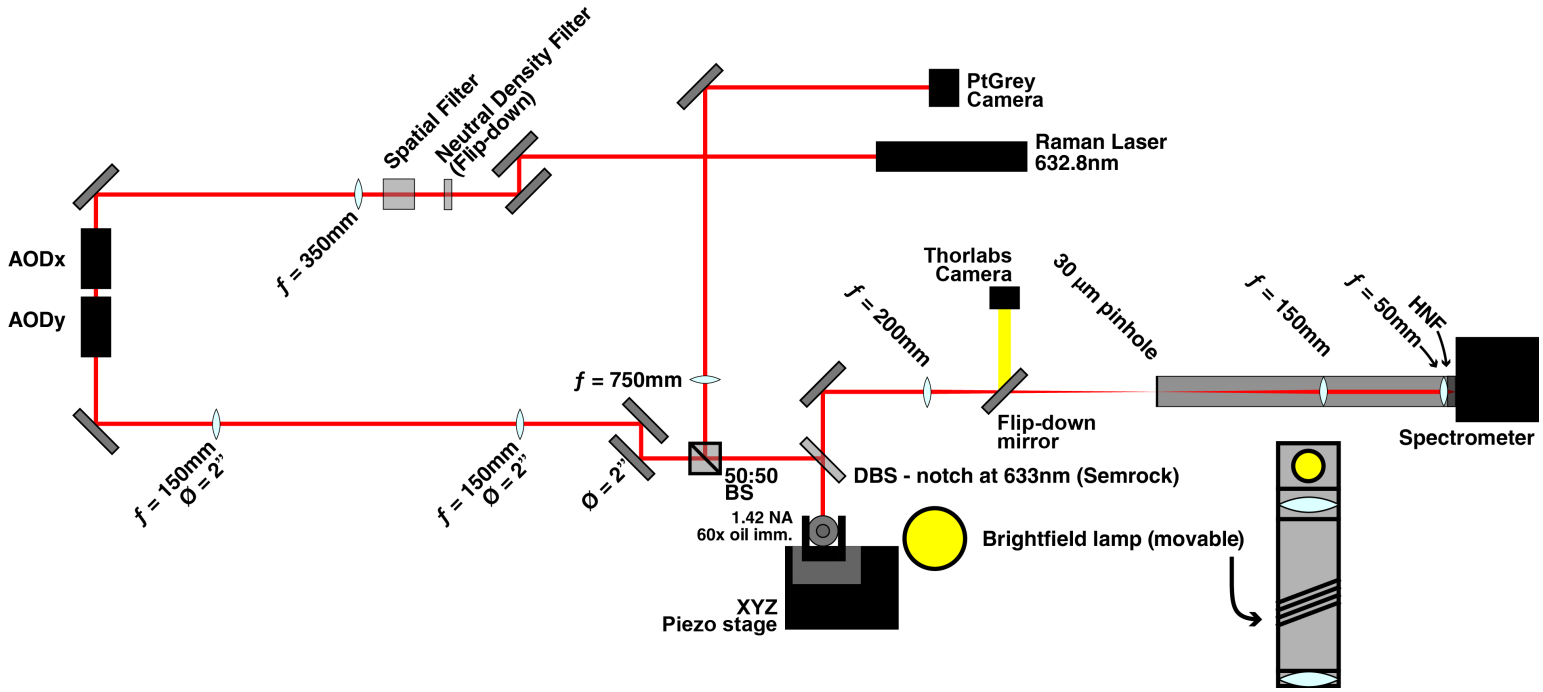

Figure 6.1: Diagram of the Instrument's Final, Wide-Field Configuration.

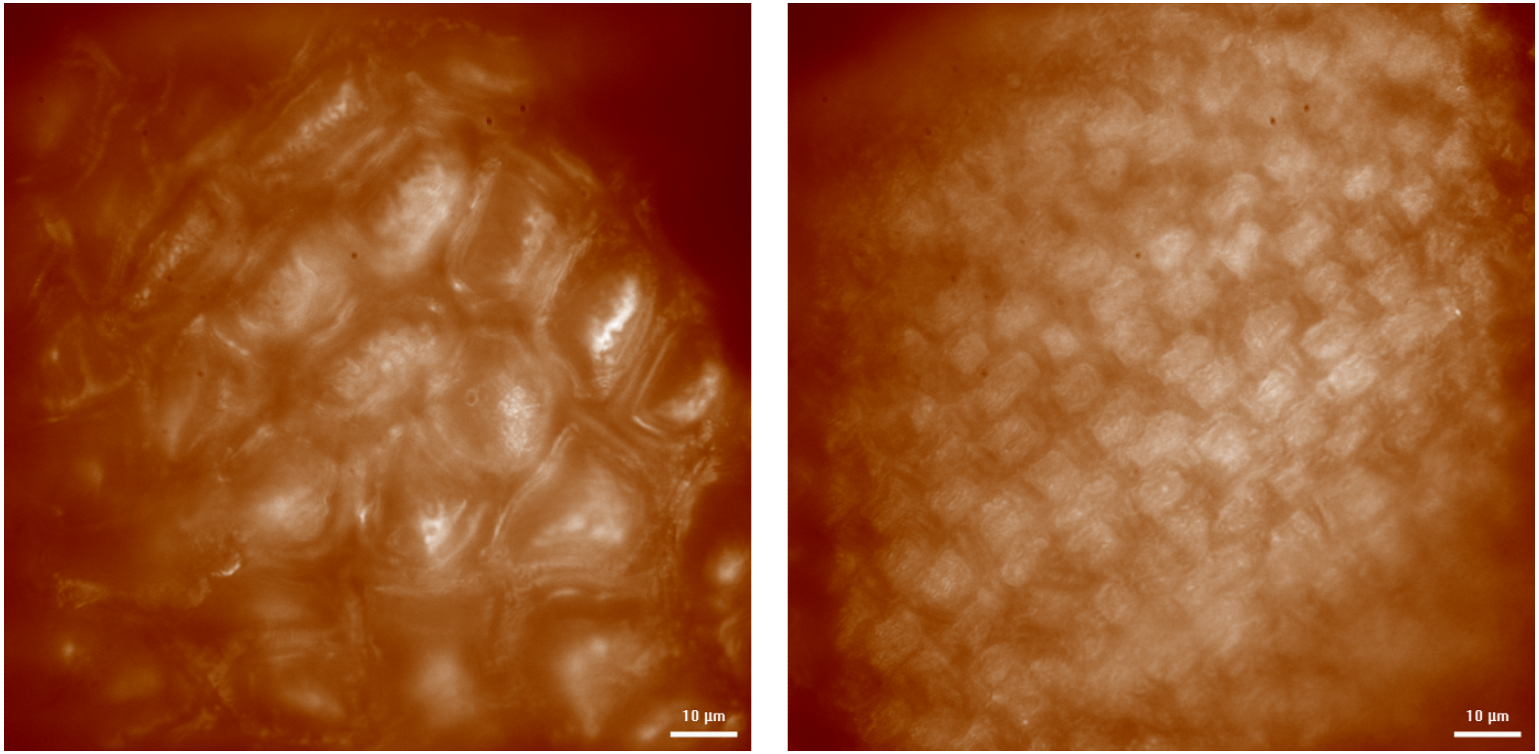

Figure 6.2: iSCAT images of a *Schistidium papillosum* sporophyte specimen. False color; field of view approx. 150 μm square. *S. papillosum is a species of moss, widespread across the northern hemisphere.*
Left: Exothecial cells of a sporangium (spore capsule), conforming to literature expectations. [75] Small trigones between the cells are visible.
Right: Distal cells of a seta. Cells are typically short-rectangular and 8-10 μm wide; [75] this is supported by the iSCAT image, though iSCAT's narrow focal plane impedes observation of the three-dimensional specimen.

6.1 Description of Upgraded Optical Train

After exiting the laser, the beam passes through a flip-down Neutral Density Filter (NDF) (for iSCAT mode only) and a spatial filter, before being focused into the Acousto-Optic Deflector (AOD) units. The beam passes through the two perpendicular AOD crystals (x and y); in Raman mode, they simply diffract the beam, while in iSCAT mode, they raster the beam into a roughly square shape at MHz frequencies. The beam is then expanded to fill the objective, directed through a 50:50 Beamsplitter Cube (50:50 BS), and reflected off a 633 nm longpass Dichroic Beamsplitter (DBS) into the objective, where it is focused onto the sample. Light returning from the sample is split by the DBS. Rayleigh-scattered light is reflected back towards the 50:50 BS, and is then focused onto the PtGrey camera's Complementary Metal-Oxide-Semiconductor (CMOS) sensor. Raman-scattered light passes through the DBS and is directed through the confocal pinhole and into the spectrometer.

6.2 List of Upgraded Components

This brief list specifies those components critical to the upgrades discussed in this chapter. See Ch. 4.1.2 for a list of original components; of those, only the autobalanced photoreceiver was removed.

- AOD system: deflector model name *45070-5-6.5DEG-.63*, driver model name *MVL050-90-2AC-A1*, manufactured by Gooch & Housego plc, Ilminster, UK

  Transmission: $>95\%$

  Frequency range: 50-90 MHz

  Diffraction efficiency: $>70\%$

  Deflection angle: 67 mrad (38 mrad from center, at 633 nm illumination)

- CMOS camera for iSCAT: model *GS3-U3-41C6M-C*, manufactured by Point Grey Research Inc., Richmond, BC, Canada

  Chip size: 2048x2048 px

  Pixel size: 5.5 μm

Mode: monochrome 8-bit

Readout rate: 45 FPS

Dynamic range: 52.78 dB

Maximum SNR: 38.82 dB

- CMOS camera for brightfield: model *DCC1545M*, manufactured by Thorlabs, Inc.

  Chip size: 1280x1024 px

  Pixel size: 5.2 μm

  Mode: monochrome 10-bit

  Readout rate: 30 FPS

  Dynamic range: 68.2 dB

  Maximum SNR: 45 dB

6.2.1 Brightfield and Köhler Illumination

The brightfield system is partially depicted in yellow in Fig. 6.1; for clarity, the path between the objective and flip-down mirror is omitted.

6.2.2 Light Source

The lamp used for brightfield illumination is a quartz tungsten-halogen lamp, model name is *QTH10*, manufactured by Thorlabs, Inc. (Newton, NJ, USA). It emits a broadband spectrum between 300 and 2500 nm, peaking at 621 nm; the spectrum is shown in Fig 6.3. Its output power is approximately 50 mW, with a color temperature of 2800 K.

The lamp is housed in an SM2-threaded Ø = 2" lens tube system, and clamped directly above the objective. The clamp is intended to allow the lamp be moved when it is not needed, as it is quite bulky. Also included in the lens tube system are two lenses and two irises, as well as an area of adjustable length (see Fig. 6.4). This setup allows the lamp to be used for Köhler illumination of samples during brightfield operations. The first lens, labeled *A* in Fig. 6.4, is the field lens that focuses light emitted by the lamp through the field diaphragm (the iris labeled *B*). From there, the light passes through the adjustable infinity space (*C*) until it reaches the condenser diaphragm (*D*). At this point, the image of the lamp's filament is in focus. After passing through the condenser diaphragm (*D*), the now de-focusing light is collected by the condenser lens (*E*) and passed towards the sample (*F*). When it reaches the sample, the light is collimated, so the image of the lamp's filament is invisible. Thus, the sample is uniformly illuminated, and its image is separated from the image of the filament, making observation much clearer.

In the instrument's Köhler illumination system, the field lens (*B*) is an uncoated biconvex N-BK7 lens with a focal length of 60 mm (part no. *LB1723*, Thorlabs, Inc.). The condenser lens (*E*) is an uncoated aspheric N-BK7 lens with a focal length of 40 mm and a Numerical Aperture (NA) of 0.554 (part no. *ACL5040*, Thorlabs, Inc.).

6.2.3 Optical Path

The brightfield lamp, when needed, is positioned directly above the sample, and its diaphragms are adjusted as necessary. Light passes through the sample, objective, and two DBS filters. This has the effect of removing all light with wavelength below 633 nm; however, the *QTH10* lamp's emission spectrum extends far into the infrared (see Fig 6.3), so this is not a big concern. The filtered light is then focused onto the chip of the dedicated brightfield CMOS camera.

6.3 Challenges and Limitations

The instrument faces a number of limitations and challenges. Many of these are physical limitations, imposed by the laws of nature, that prevent the instrument from working in *just* as one might want it to. Perhaps the best known example of

such a limitation, at least with regards to microscopy, is the Abbe diffraction limit. In simplest terms, one cannot observe objects much smaller than the wavelength of the light being used to observe them.

6.3.1 Raman Power Limitations

One of the most straightforward limitations of the instrument can be found in its Raman functionality. Namely, the relatively low emission power of the laser (21.5 mW) means that the Raman effect in general, and Raman data of interest in particular, can be difficult to observe. The instruments ability to pair Raman data collection with iSCAT imagery does mitigate this challenge somewhat, insofar as one can associate Raman data with features observed in iSCAT, thus making it easier to attribute Raman data to a particular sample region.

Nevertheless, collecting Raman data is still a challenge. By the time light from the laser has reached the objective, it has passed through two lenses, a longpass filter, and a quarter wave plate, as well as being reflected off two silvered mirrors and a notch filter (see Fig. 6.1). None of these optical components have 100% transmittance or reflectance, and thus each component attenuates the light's power slightly; the light filling the objective is slightly less than 21.5 mW, and that is just the incident light.

Spontaneous Raman emission is, in itself, an unlikely process. In most cases, a miniscule fraction of scattered photons has undergone spontaneous Stokes or anti-Stokes scattering (as opposed to elastic Rayleigh scattering). [69] Thus, the power of spontaneous Raman scattered light returning from the sample has been reduced by many orders of magnitude compared to the incident light. After leaving the objective, this weak Raman light passes through three lenses, three filters, the 100 μm confocal pinhole, and the quarter wave plate before reaching the spectrometer, with each component attenuating its power slightly more. Spontaneous Raman signals are thus very weak and difficult to observe, due to the limited laser power.

There are a number of tricks one can employ in order to improve the strength of a Raman signal. One common example is Surface-Enhanced Raman Spectroscopy (SERS), which can increase the power of Raman signals by many orders of magnitude. This is accomplished by adsorbing a sample to a metallic surface,

and although the exact mechanism of enhancement is not well understood, it is typically believed to be the result of surface plasmons. [68, 69] However, this technique is not commonly applied to biological samples, where non-destructive and non-adulterative imaging is crucial. [77]

6.3.2 Raman Signal Limitations

A further complication with spontaneous Raman emission is that weak signals are highly prone to outside interference. This can come from any number of sources, including cosmic rays and overhead lights, as well as sample fluorescence. Cosmic rays are transitory extrasolar high energy particles, typically protons, and are observed by the spectrometer's Charge-Coupled Device (CCD) if they happen to strike it. See Fig. 6.5 for an example; note how the cosmic ray artifact drowns out the Raman signal, which is itself mostly background fluorescence from the glass cover slip. There is no practical way to shield the system from cosmic rays, so cosmic ray artifacts must be mathematically removed from collected data. Given their appearance as very sharp spikes, this is not difficult; one need only use a simple median filter to remove them.

More persistent interference, however, is not so easy to remove. Raman signals are extremely prone to being overwhelmed by fluorescence signals, which are much more intense. Fluorescent overhead lights are no exception to this, as mercury's fluorescence emissions will handily drown out any useful Raman data. Thus, the instrument is operated with the overhead fluorescent lights turned off and thick laser-proof curtains blocking out light from other parts of the laboratory. This works well enough, but other light sources within the darkened laboratory can cause interference, especially the mercury lamps or LEDs that illuminate computer monitors, as well as any incandescent lamps that are used to help researchers see what they are doing. In order to exclude as much foreign light as possible, the Raman branch of the instrument, after the confocal pinhole, is isolated within a lens tube.

Fluorescence in the sample is much harder to abate than either cosmic rays or background light. In fact, there is no way to reliably extract Raman data from highly fluorescent samples. For mildly fluorescent samples, however, there are a

number of mathematical post-processing techniques that can be employed to remove or abate the fluorescence background. These are discussed in more depth in Ch. 8.2.2. All samples contain some mild fluorescence from the glass on which they are mounted. As demonstrated in Fig. 6.6, removing this information is not impossible, but the results often need further processing to become usable. In the example, the fluorescence removal process used Second-Derivative Variance Minimization (SDVM) background subtraction and Discrete Wavelet Transform (DWT) (sym 5 wavelet, 10 iterations). Data processing methods are discussed in more detail in Ch. 8.2.

6.3.3 iSCAT Resolution Limit

As previously mentioned, the resolution of the wide-field iSCAT system is Abbe diffraction limited to 223 nm[1] In practical terms, this limit is not as clear-cut as it appears; as long as a sample's Point Spread Function (PSF) is larger than 223 nm in diameter, it can be imaged, *even if* the sample itself is smaller than the diffraction limit. The wide-field configuration also obviates the piezo-imposed instrumental limit discussed previously.

The PSF is observed as a blurring or broadening of a small sample. In general terms, it arises because the system's optics can only capture a portion of a small sample's scattering field.[2] Since, under Mie theory, scattering phase functions for small particles are more or less spherical, capturing a segment of a scattering field and projecting it onto a planar detector causes an Airy disk to form around the focal point. Under normal conditions, it will not be a perfect pattern, because of optical aberrations in the lenses, but nonetheless it will expand the observed spot. Thus, the PSF effectively allows the detection of some large sub-diffraction sized samples.

To put this to a practical test, we imaged various sizes of gold nanoparticles. Since they are only commercially available at certain diameters, it was a matter of finding the smallest visible diameter set. In fact, the smallest that could be imaged were 30 nm, several times smaller than the Abbe diffraction limit (223

[1] See Ch. 4.3, Eq. (4.1).

[2] Typically, the PSF is described in terms of a perfectly spherical point *emitter*, but that does not apply in the case of iSCAT.

nm). Figure 6.7 shows one of the particles that was imaged in aqueous solution. The nanoparticle's apparent size is approximately 450 nm; this is caused by its PSF. Using the instrument's iSCAT video function, the motion of the nanoparticles in solution was easily observed.

Another way to test the resolution of the instrument is to use a test target; Figs. 6.8 and 6.9 show the results of imaging a 1951 USAF resolution test chart, which consists of a group of progressively smaller line pairs. Fig. 6.9 shows a schematic of the imaged area. The actual target, however, is the negative of Fig. 6.9: the black patterns are transparent glass and the white background is opaque (low-reflectivity chrome, plated onto the glass substrate).

In the iSCAT image of the target (Fig. 6.8), the transparent glass sections appear dark and the opaque chrome appears light. This speaks to the imaging mechanism of iSCAT; the transparent glass areas have the same refraction index as the immersion oil and objective optics ($n = 1.518$), thus they do not produce any interference in the scattering field. On the other hand, the chrome plating has a substantially different index of refraction (approx. $n = 3.2$), [78] which causes substantial substantial interference and high observed iSCAT intensity.

6.3.4 The iSCAT Background

One of the most pernicious difficulties with wide-field iSCAT imaging is the omnipresence of a substantial background. This can be seen clearly in Fig. 9.1. Since the background is not uniform, and it pervades all images, it is essentially impossible to remove mathematically. Referring to Ch. 2.1 and the general iSCAT equations, the contribution from the reflection r is critical:[28]

$$I_{\text{iSCAT}} = |E_i|^2 \left\{ r^2 - 2r|s|\cos\phi \right\} \tag{6.1}$$

The r^2 term represents the background (and reference) signal, from the reflection of the cover slip. The observed intensity pattern in the background is caused by the non-uniform illumination of the out-of-focus cover slip.[3] Thus, the background contribution is physically inseparable from the data, and mathematically

[3] See Fig. B.1 for the illumination patterns.

extremely difficult to attenuate.

However, looking at data collected using the single-channel iSCAT configuration,[4] the background observed with the wide-field configuration is conspicuously absent. Keeping Eq. (6.1) in mind, one can deduce that the background is not actually gone, but rather uniform - and therefore much easier to treat mathematically. This is, of course, because in the old configuration, samples were uniformly illuminated.

This knowledge presents a possibility: if data could be collected on the two-color instrument using a similar single-channel process to that of the old instrument, *alongside* the wide-field channel, then perhaps the intensity variations in the background can be accounted for and removed. The development of such a system, and some of the challenges it faces, are addressed in Ch. 9.1.

[4] Figs. 4.6, 4.2, 4.3, 5.2, 8.3

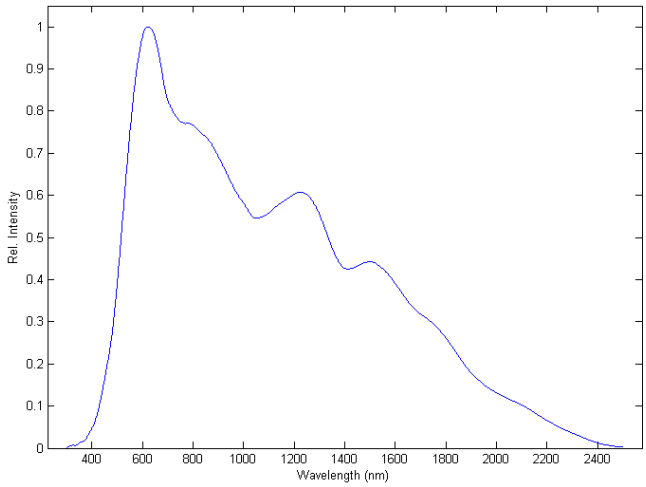

Figure 6.3: Emission spectrum of *QTH10* tungsten-halogen lamp. Data from Thorlabs, Inc. [76]

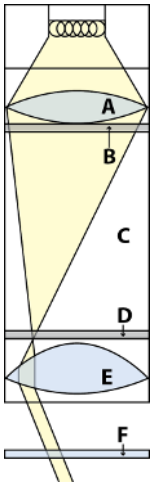

Figure 6.4: Schematic of Köhler illumination setup, from lamp (top) to sample (bottom). *A:* Field lens (biconvex). *B:* Field diaphragm. *C:* Infinity space. *D:* Condenser diaphragm. *E:* Condenser lens (aspheric). *F:* Sample.

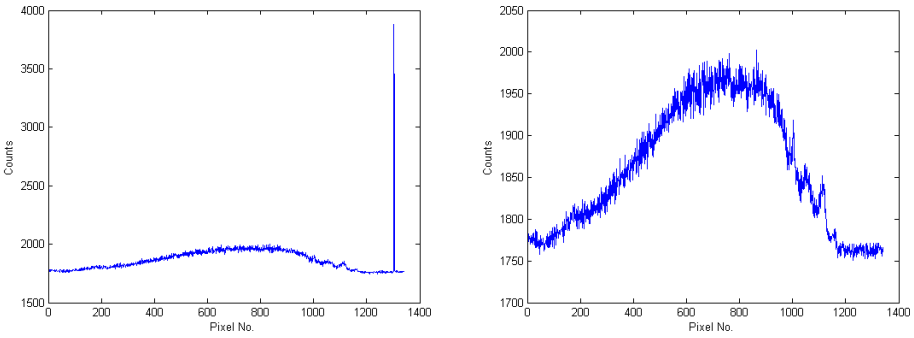

Figure 6.5: Two Raman spectra of a marine aerosol sample (integration time: 400 ms, taken sequentially). The spectrum on the left features a cosmic ray artifact, at pixel no. 1303.

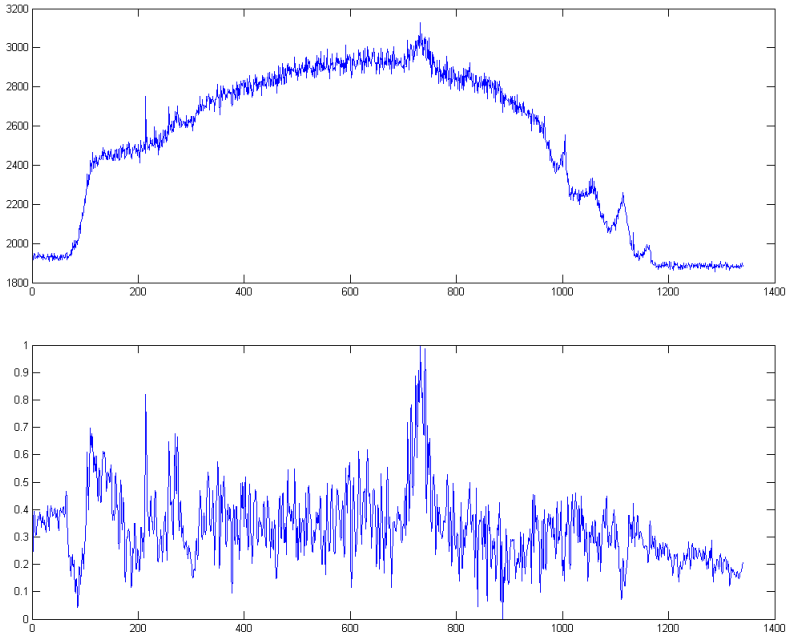

Figure 6.6: *Top:* Raw Raman spectrum of poly(methyl methacrylate) (PMMA), collected from a microtome section of plasticized neural tissue (integration time: 25 sec). The spectrum exhibits a large glass background.
Bottom: The same spectrum, with the glass background mathematically removed using SDVM and DWT.

Figure 6.7: iSCAT image of a 30 nm gold nanoparticle in aqueous solution. Field of view approx. 6.5 by 5.5 μm, nanoparticle PSF diameter approx. 450 nm. Contrast enhanced.

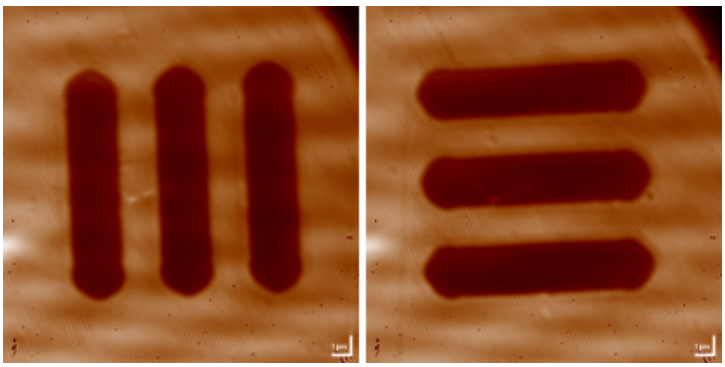

Figure 6.8: Optically expanded iSCAT images showing lines from Group 7, Element 6 of a 1951 USAF resolution test chart, the smallest lines on the chart. Line pair width is approximately 4.4 μm. False color; fields of view approx. 17 μm square.

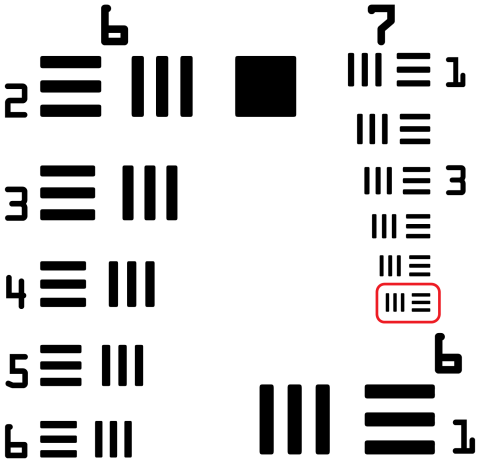

Figure 6.9: Schematic of the 1951 USAF resolution test chart used for the above images; total size approx. 4 mm square. The pattern conforms to the MIL-STD-150A standard. The imaged lines are circled in red.

Chapter 7

Designing the User Interface

Work to develop a User Interface (UI) proceeded in concert with the construction and optimization of the instrument's optical train. We coded this interface as a Virtual Instrument (VI), using LabVIEW 2014. This chapter outlines the design process and the functionality of the VI.

7.1 Communication Problems

One confronts a number of challenges when designing control interfaces from scratch. The most urgent is setting up communication between the hardware and the software. Most hardware comes with basic software designed by its respective original equipment manufacturer (OEM), which is useful for basic testing. The problem with such software is that it is typically designed to be stand-alone and cannot be easily integrated with other software, owing to its reliance on proprietary OEM drivers and source code. As previously alluded to, this is the reason that the Scientific Imaging Toolkit (SITK) drivers are needed: to communicate between Princeton Instruments hardware (i.e. the spectrometer) and the LabVIEW software. Again, the new VI has its base in the SITK example VIs; these examples were designed to be used as building blocks, so to speak, that incorporate the nitty-gritty of calling Dynamic Link Library (DLL) drivers into handy sub-VIs.

Little in the way of starting material came with the other hardware, including in particular the piezo system and the iSCAT and brightfield cameras. Each has its

own way of communicating with the computer, requiring unique protocols. For example, the piezo drivers use serial port communications, the iSCAT camera uses National Instruments' proprietary image acquisition (IMAQ-DX) drivers, and the Raman spectrometer uses specialized DLL drivers.

Combining all these protocols into a single program presents a challenge, but one that LabVIEW is well suited to handle. By cordoning off routine hardware communication code blocks into sub-VIs that can be called as needed, the various communication protocols become modular, and thus much easier to incorporate into code as needed. Figure 7.1 shows one such example. The code block *Thorlab MDT 693* in the center of the image contains the actual communication protocols, and the inputs can be wired as needed. On the left-hand side of the block, the inputs from top to bottom are: the port number for the piezo driver (blue wire, defined as `0` for `COM1`), a string indicating the piezo axis to move (pink box and wire, x-axis), and `NewVal`, the user-input desired position value (orange wire). On the right-hand side of the block, the output is the actual position value after moving, read back from the driver. Throughout the Operations VI, there are several times this communication procedure must be called, so defining it as a sub-VI is by far the most efficient way to handle it.

One common problem that arises from having a multitude of different communication protocols is communication conflict. For example, when the software is actively reading from the iSCAT camera, it cannot communicate with any additional hardware, because the live display must operate within a while loop. Determining how and when such conflicts might arise is a very important part of the software design, and will be addressed in the next section.

7.2 Constructing a Unified Interface

The final challenge of designing a control interface is to bring everything together into a convenient UI. First, the software should be able to execute any and all functionalities that users may need. This requires judiciousness on the part of the designer, so that superfluous tools are excluded and future needs are accounted for. The details of these functionalities will be reviewed in the next section.

As functionalities are being developed, they need to be put together in a way

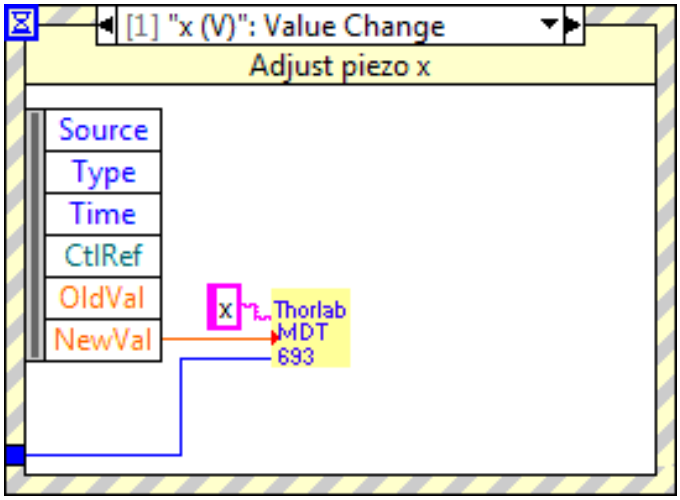

Figure 7.1: Event structure showing the case for moving the *x*-axis piezo driver to a user-input value (input into the numeric control *Set x*), using a sub-VI.

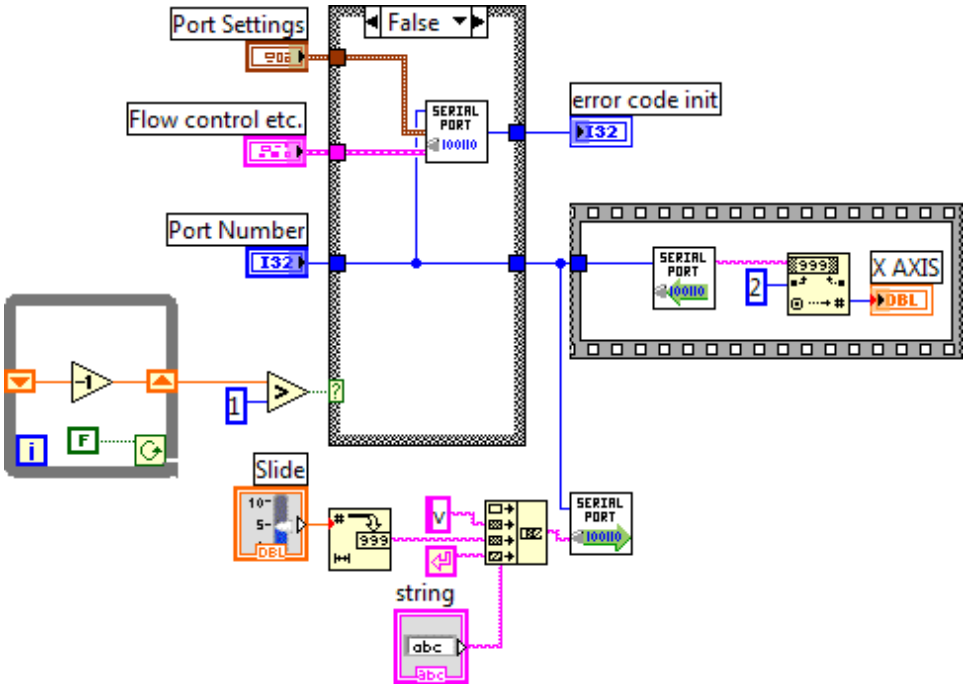

Figure 7.2: Serial communication contained within the sub-VI in the above image.

that is easy-to-use and, more importantly, efficient. This again requires judiciousness, in order to lay out the information hierarchy presented to the user by the UI. It also requires the designer to practice quality control, in order to predict what could go wrong and determine how the software handles errors.

The easiest way to organize the information hierarchy of the VI was by using a tab control structure. That way, each separate data collection mode could be given its own tab pane, without too much clutter from other irrelevant features. The VI has ten tabs in total: three for initializing and setting up the spectrometer, four for Raman data collection and processing , two for iSCAT data collection, and one for brightfield data collection.

Having thus divided the VI, each tab's own information hierarchy had to be laid out. As mentioned in the previous section, protection against creating communication conflicts was necessary; this was by and large done cosmetically, by simply disabling various controls during situations where their use could cause errors. The tabs also had to be designed in such a way so as to facilitate ease-of-use. This included adding such features as progress bars, as well as organizing controls and displays in a logical manner.

As an example of a typical design decision, consider the piezo system. At its most basic, it can be used to reposition the sample on the objective by changing the voltage being fed to any of its three drivers (see Fig. 7.1). Simply having the ability to make that adjustment within the VI is not enough, however, as some applications may require multiple movements in sequence. This is best addressed through movement automation, so that the software will automatically move the piezo position along a user-set line, or raster the position over a user-set area, both with a user-set number of steps.

Aside from programming that automation process, deciding *where* to put the piezo controls involves both knowledge of how the instrument might be used, as well as design and programming considerations. The location of the controls is very important on both the front panel and the block diagram; for example, though they appear similar, the piezo movement controls for iSCAT and Raman are different. In the iSCAT Viewer tab, the piezo controls can *only* be used while the software is reading data from the iSCAT camera. As previously indicated, this is the case because of the live display must operate within a while loop. If, on the block di-

agram, the piezo controls were located outside the while loop, they would *not* be accessible during viewing of iSCAT live video. This is not an ideal arrangement, as users typically want to see how their piezo adjustments affect the iSCAT image in real time. Therefore, the piezo controls were placed inside the while loop, so that they could be used concurrently with the iSCAT camera.

On the other hand, in the Raman Collection tab, the piezo controls can only be used while the software is *not* reading data from the spectrometer. This is because it is highly undesirable for a sample to move during Raman data collection. Thus, in order to prevent users from accidentally destroying the validity of their Raman data, the piezo controls are made accessible only while Raman data is not being recorded.

Many such design decisions were made throughout the course of building the Operations VI, due to the numerous functionalities that it provides.

7.3 Functionality of the User Interface

This section will outline some of the features of the Operations VI. These features were gradually added and refined over time, both as the need arose, and as future needs were predicted. The next chapter (Ch. 8) will describe the standard operating procedures for how the instrument and VI are used to collect data.

7.3.1 iSCAT Features

The flexibility of the IMAQ-DX drivers allowed for a host of options to be added to the iSCAT data collection process. Chief among them is the ability for a live display of iSCAT information being read from the camera. That display includes cosmetic options to apply false color and to zoom in on the image, as well as more substantive additions, such as a superimposed scale bar, and the ability to re-center the image on a selected point.

Additionally, iSCAT raster scan functionality was added, much like that in the old instrument. This can be both a two-dimensional area scan, or a one-dimensional linear trace. Options for how to record iSCAT data were added as well, allowing users to choose between video, still images, or text arrays.

7.3.2 Raman Features

The SITK building blocks include functions for initializing the spectrometer, as well as very basic spectrum capture features. Since the initialization of the CCD camera and setup of the spectrometer are fairly involved hardware operations, they were included more or less as-is. These include setting up exposure time and monochromator position, as well as more advanced settings that are not routinely used but could prove useful in exceptional circumstances.

In addition, SITK's focusing function was retained, but with the addition of an option to view the entire CCD chip, rather than just a binned portion of it. This was useful both for focusing on a sample, but also for aligning and tuning the confocal Raman branch of the instrument.

To maximize the instrument's Raman data collection capacity, several augmentations to those basic functions were added. In the previous instrument, the collection of rastered Raman maps was routine, albeit very lengthy (see Ch. 4.2). This ability was added as an option to the new VI. Another key addition was the option of doing some on-line processing, or of exporting the collected data into a separate dedicated processing VI. The online processing methods that were included are, in sequence, Discrete Wavelet Transform (DWT), Savitzky-Golay filtering, zeroing, and normalization.

7.3.3 Other Features

As the brightfield imaging system is not intended to be used to collect routine data, but rather simply as a qualitative imaging tool, its features in the VI are few. Brightfield images can be viewed live and be recorded as text arrays.

Error handling is another important feature of any software. As previously mentioned, measures were taken to try to prevent users from causing certain types of errors. But, there are other errors that could not be prevented by the software at all; the only thing the software could do is display a relevant error message. These types of errors include hardware being powered off, or having been unplugged from the computer.

Unfortunately, the error messages that are displayed by such errors frequently are very cryptic or technical in their wording, and of course, offer no suggestion

for how to go about resolving the problem. In order to provide a resource for addressing those types of problems, a list of possible error messages was compiled, along with information about what caused them and how the underlying problems could be fixed.

Chapter 8

Data Collection and Processing Techniques

This chapter will cover some basic data collection procedures, as well as some basic data processing techniques.

8.1 Data Collection: Procedures and Practices

One of the biggest advantages of the present instrument, as alluded to in Ch. 1.3, is the facility of sample preparation. Since Interferometric Scattering Microscopy (iSCAT) is at its core an optical microscopy method, sample preparation is essentially identical to that used by more traditional microscopy methods: glass slides and coverslips, though with the addition of index-matched immersion oil, as required by the objective. Samples need not undergo chemical alterations, though some physical alterations, such as resizing, may be necessary.

When imaging animal cells, having them squished by a coverslip is generally not desirable, as the cells will rupture, or at the very least, distort. To get around this problem, we purchased a microscope well slide specifically designed to image live cell cultures, and modified it for our needs. This well slide was not needed to image plant samples on a cellular level (Figs. 5.1, 6.2), as they have rigid cell walls.

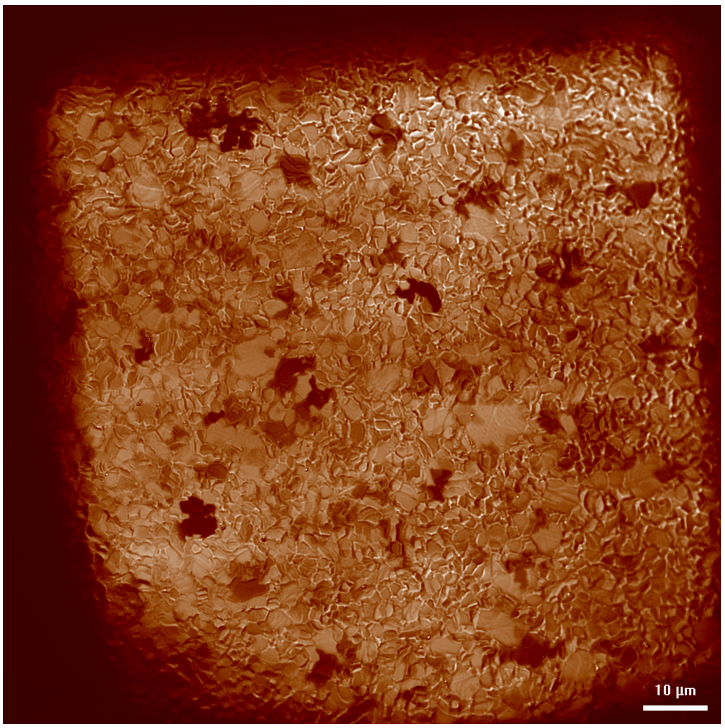

Figure 8.1: iSCAT image of graphene deposited on nickel. Its deposition profile is non-uniform. False color; field of view approx. 150 μm square.

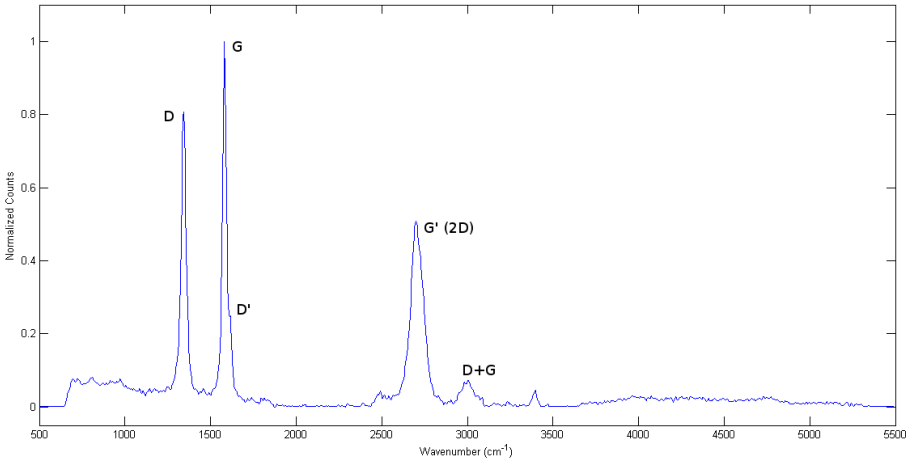

Figure 8.2: Processed Raman spectrum of graphene deposited on nickel, 8 sec integration. Peak assignments shown; the intensity ratio of *G* (1582 cm^{-1}) to *G'* (2700 cm^{-1}) peaks - approx. 2:1 - indicates the graphene is multilayered. [79, 80] Processed using DWT, Savitsky-Golay filter, zeroing, and normalization.

8.1.1 iSCAT Data Collection

Collecting iSCAT data is quite straightforward. The most significant challenge is actually focusing on the sample; this can be difficult if the sample is very small, or if the sample does not have a large refractive index morphology. An example of such would be tissue consisting mostly of water; this would produce little in the way of iSCAT signal as the interference would be largely uniform throughout the sample.

Since the iSCAT focal plane is quite narrow, on the order of microns, it is sometimes necessary to use the piezo actuators to focus the sample. This is made easy with the video iSCAT display in the software;[1] however, if a sample is not flat - as is often the case - then only a small part of the sample may be contained within the focal plane. Collecting reliable iSCAT data in such a circumstance typically requires a raster scan along the z axis. This presents its own difficulty, insofar as the out-of-focus parts of the sample will contribute scattered light to the partially in-focus image, which may obfuscate regions of interest to the user.

Once focused, iSCAT data can be recorded in a number of ways. Most commonly, it is saved as a still image in Portable Network Graphics (PNG) format. This is the most convenient form for storage and transmission. Still images can simply be captured from the video iSCAT display, in a "what you see is what you get" situation, or they can be collected at points along a raster scan. The average full-size (2048 by 2048 pixel) image is approximately 4 MB in size. There are many image processing techniques that can be applied to improve image quality; the next section (Ch. 8.2) will discuss some of these techniques. The PNG format applies lossless compression to the recorded bitmap; the end result is an array of 8-bit pixel data.

iSCAT data can also be stored as 30 Frames per Second (FPS) video data in Audio Video Interleave (AVI) format. Again, video can be recorded both from the video iSCAT display or of a raster scan. Video is useful for live or otherwise mobile samples. Additionally, during a raster scan, recording video can be preferable to storing scores of still images. A nine-second video occupies 42 MB, whereas 270 still images (equal to the number of frames in the video) would occupy 1 GB;

[1] See Chs. 7.3.1.

however, a raster scan that produced nine seconds of video would almost certainly consist of only a few dozen images, rather than hundreds. Writing an AVI file uses the Motion JPEG codec, such that each frame is stored as a JPEG image within the AVI file. The JPEG format applies lossy compression to the recorded bitmap, thereby reducing its quality; the result is many arrays of 6-bit pixel data interleaved at a rate of 30 per second.

The third data storage method is as a double-precision floating point array. This format is substantially different, not least because it entirely lacks any visual aspect. The array storage is designed to maximize the dynamic range of the image by iteratively adding multiple accumulations - the numeric equivalent of still image captures - thus increasing the difference in pixel intensity between the darkest and brightest regions. The default number of accumulations is 200. The array storage is also useful since it lends itself to mathematical processing techniques that can be more difficult to apply to images. A floating point array is the most true-to-life data storage method, because it is neither encoded nor compressed. When comparing to PNG and AVI formats (8 and 6 bits per pixel), the floating point array stores data at 64 bits per pixel, with a vastly superior dynamic range. Therefore, for applications where rigorous data processing is required, floating point arrays are ideal.

8.1.2 Raman Data Collection

Observing Raman data is a challenge, due to the inherent weakness of the Raman effect. It is quite often the case that samples are either not Raman-active at all, or are only very weakly so. Samples might only produce a signal in certain region, and the signal may be so obfuscated by background noise or fluorescence that it is not even discernible without advanced processing.

Thus, getting a sample perfectly in focus for collecting a Raman spectrum is often very difficult. The best practice is usually to use the focusing display to attempt to find a signal, then set up a raster scan along the z axis in an attempt to refine the precise focal plane.[2]

Finding a Raman signal can be assisted by iSCAT. By using the video iSCAT display to localize a region of interest on a sample, the Raman probe can then be

[2] See Ch. 7.3.2.

directed to that region, and then rastered as desired. This is another of the big advantages that the present instrument offers.

When it comes to storing Raman data, there is really only one option: a floating point array. Because the readout from the spectrometer's CCD is typically fully binned vertically, it consists of a one-dimensional array 1,340 numbers long. The spectrometer can be set up to record multiple frames per capture, which has a similar effect as the floating point array accumulations mentioned previously, except that in this case each frame is stored as a separate row in the file, rather than being added to the previous one-dimensional array.

8.2 Common Processing Techniques

This section will outline some of the data processing techniques used to clean up both iSCAT and Raman signals. The details of these techniques are very well-reported in the literature.

8.2.1 Processing iSCAT Data

The manner in which iSCAT data are processed depends largely on how the data are stored. As a floating point array, any number of processing methods can be applied. PNG images are treated as intensity arrays, but because of their encoding, are open to different methodologies. AVI movies typically must be separated into their component frames for processing, which can be a lengthy process.

The goal of the processing is typically to remove noise from the iSCAT image; the background, discussed in Ch. 6.3.4, is not so easily removed.

One of the most common noise removal techniques for image processing is the median filter. In essence it functions by replacing the intensity of a given pixel with the median intensity of that pixel's neighbors, in one or two dimensions. The radius can be extended to include several neighboring pixels. [81] This has the effect of abating random noise or shot noise, but at the cost of image clarity. Overcorrection (i.e. too large a radius) can effectively blur an image beyond recognition. Given that random noise is not highly prevalent in wide-field iSCAT images, the median filter is used sparingly.

Another, more sophisticated noise removal technique is the two-dimensional

Discrete Wavelet Transform (DWT). The DWT algorithm, originally developed for one-dimensional data sets, decomposes a signal into a set of waveforms with a range of frequencies (termed *wavelets*), the sum total of which approximates the signal. [82] Depending on the needs of the user, several of the wavelets at the high and low ends of the frequency range are rejected, and the signal is re-composed from the remainder. Low-frequency wavelets typically contain persistent background contributions, whereas high-frequency wavelets typically contain junk data, such as shot noise. [51, 82] The technique can be tailored to the user's needs, and expanded into two dimensions, thus proving to be useful for de-noising an iSCAT image.

8.2.2 Processing Raman Signals

There are a number of algorithms that are routinely used to process Raman spectra; Chapter 6.3.2 briefly mentions some techniques for background removal, making reference to Figs. 6.5 and 6.6. Fig. 8.2 shows an example of a highly processed spectrum.

Noise and Background Removal

As discussed previously, DWT is a fine methodology for de-noising Raman spectra. [51, 83] Another complementary technique is the Savitsky-Golay filter, which uses polynomial approximation to smooth a signal over a preset window. [82] As with iSCAT images, care must be taken to avoid over-smoothing, as that might remove meaningful data that is not easily visible.

Background removal is also an important step in Raman signal processing. As discussed in Ch. 6.3.2, many signals contain large background contributions. Simple mathematical subtraction of a preset background spectrum is insufficient, as the background level tends to vary between spectra. Thus, more elaborate methods are required, such as Second-Derivative Variance Minimization (SDVM). SDVM functions by computing the difference of the second derivatives of a signal spectrum minus a scaled background spectrum. These second derivatives are smoothed using the previously mentioned Savitsky-Golay filter, and the resulting difference spectrum is compared to an arbitrary threshold for an acceptable background con-

tribution. The scaling factor is recalculated and the subtraction iterates until the threshold is met. [84] However, as can be seen in Fig. 6.6, the result is often quite noisy, and further processing may be needed.

Chemometrics

In Raman data sets, meaning is so often hidden that a host of chemometric techniques must be employed to elucidate anything from a set of spectra. One of the most basic chemometric techniques is PCA, which functions by transforming a data set onto an orthogonal basis set where each variable (termed *principal components*) is a linearly independent contribution to the set's overall variance. The algorithm works such that the first principal component represents the largest contribution to the overall variance, the second principal component the second largest, and so on. [86] Figure 8.3 shows an example of a practical application of PCA, where the first two principal components provide useful information that would not otherwise be apparent.[3]

The simplicity of PCA limits its utility as a multivariate processing method, especially when the user wishes to quantitatively correlate spectral features to other real-world variables, using a classification model. In such situations, more advanced processing methods are needed, typically involving regression analysis. The Partial Least-Squares Regression (PLS) is perhaps the best-known of these methods. Given a matrix of measured signals $\mathbf{X}$ and a matrix target properties $\mathbf{Y}$, the regression can be mathematically represented as:

$$\mathbf{Y} = \mathbf{Xb} + \mathbf{e} \tag{8.1}$$

where $\mathbf{b}$ is the matrix of regression coefficients, and $\mathbf{e}$ is the error matrix. [87, 88] $\mathbf{Y}$ contains known classification information, $\mathbf{X}$ represents experimentally observed spectra, and $\mathbf{b}$ is determined through the model. PLS projects both data matrices onto a new basis set that maximizes the covariance between the dimensions of $\mathbf{X}$ and $\mathbf{Y}$, such that the latter can be predicted by linear regression from the former; this is the aforementioned classification model. It is often the case that $\mathbf{X}$ contains

[3] See also Figs. A.1 and A.2.

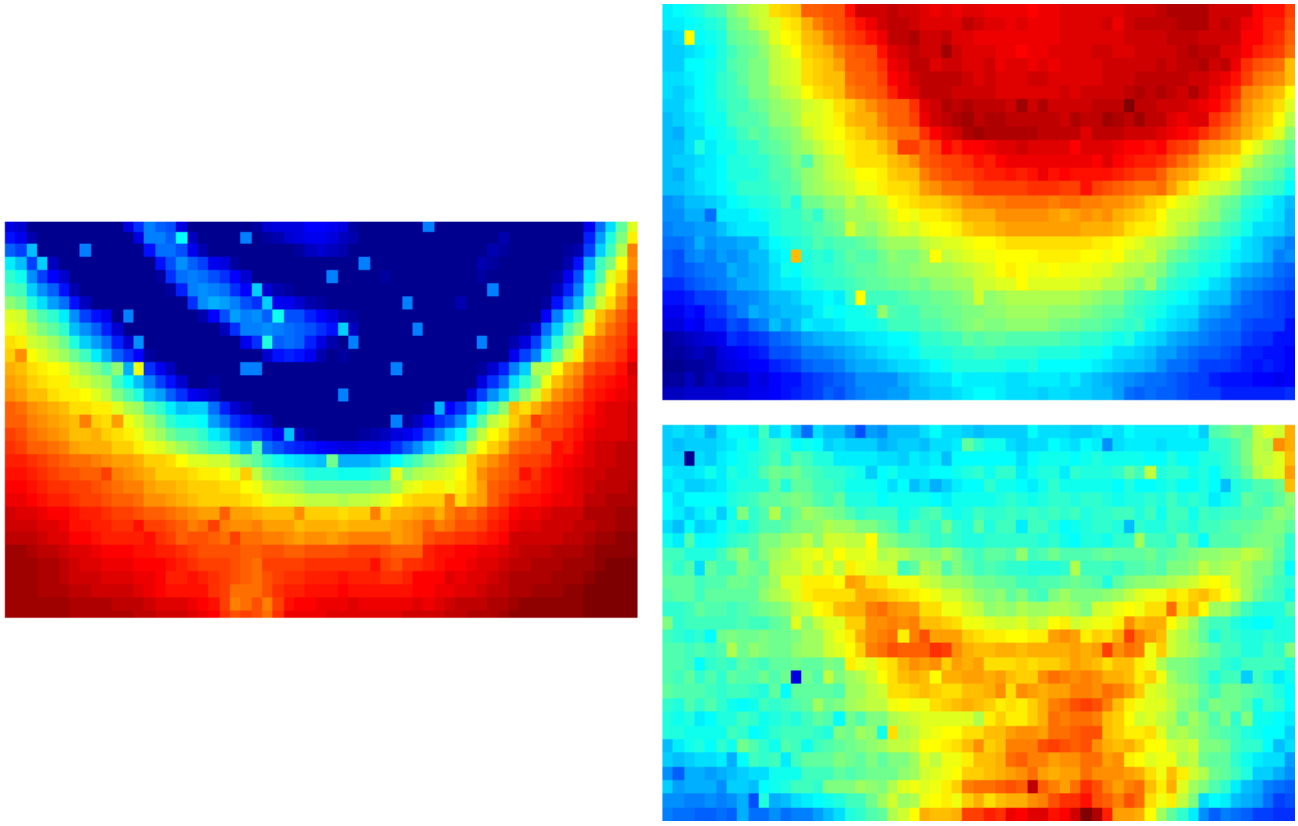

Figure 8.3: Data set showing magnesite adsorbed to a polystyrene bead, collected using the single-channel configuration (Ch. 4). See Fig. 4.4 for a single Raman spectrum of the bead, and Figs. A.1 and A.2 to compare the principal component maps to unprocessed Raman peak maps. *Magnesite is a carbonate mineral, having the formula* $MgCO_3$ *in its dehydrated form.* [85]
Left: iSCAT map of sample, approx. 20x12 μm.
Right, Top: Map of principal component 1 based on collected Raman spectra, processed using PCA. PC1 accounts for 64.7% of the variance within the Raman data set. Given its clear correlation with the iSCAT map (*left*), it is reasonable to infer that PC1 represents the polystyrene bead within the data set.
Right, Bottom: Map of principal component 2 based on collected Raman spectra. PC2 accounts for 7.30% of the variance within the Raman data set. PC2's concentration around the margin of the bead indicates that it represents the adsorbed magnesite within the data set.

many more dimensions than does **Y**, but PLS is well suited to handle that since, like PCA, it determines which dimensions are relevant to the target properties and which are not. [89] See Fig. 3.2 for an example of a PLS model.

When these methodologies fail to produce meaningful results, still more advanced processing techniques can be employed, such as Template-Oriented Genetic Algorithm (TOGA) and Orthogonal Signal Correction-Support Vector Machine (OSC-SVM). These techniques are based on machine learning, which falls outside the scope of this thesis; it is sufficient to simply assert that TOGA and OSC-SVM are better at discarding junk data from calibration models than is PLS. [45, 90]

Such a variety of data analysis methods opens the instrument described herein to a whole host of possible uses. From simple imaging to providing quantitative data about chemical and physical properties of a sample, the instrument is well-suited to meet the needs of contemporary microscopy.

Chapter 9

Future Prospects

As the operations of the instrument became routine, that left time to pursue several new prospects. One of them was the development of a confocal iSCAT channel, at least at a proof-of-concept level, that would function as an alternative to the current wide-field channel. As previously discussed in Ch. 6.3.4, the omnipresent background in wide-field iSCAT images is somewhat problematic, and developing a complementary confocal channel could be a way to address the problem.

9.1 Moving to Confocal iSCAT: A Clearer Picture

A confocal iSCAT channel would use pinholes - one after the laser and one before the detector - and a scanning galvanometric mirror system, rather than Acousto-Optic Deflector (AOD)s. Such a system would represent a significant alteration to the instrument (as well as outlay of funds), so a reasonable facsimile was devised. This pseudo-confocal arrangement uses a single pinhole and an single-channel detector. The development of the pseudo-confocal iSCAT channel is outlined in this section.

9.1.1 Challenges Facing Wide-Field iSCAT

The iSCAT background problem has been addressed in Ch. 6.3.4; however, this is not the only difficulty facing wide-field iSCAT.

Figure 9.1 shows what a typical out-of-focus iSCAT image looks like. This im-

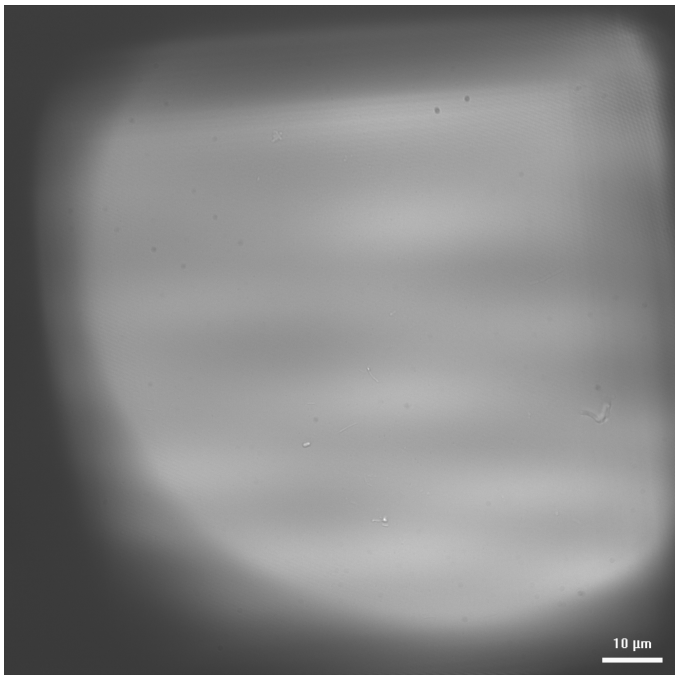

Figure 9.1: Irregular illumination in an unfocused iSCAT sample, illustrating the large background contribution present in all wide-field images. Note the similarity of the pattern with that in subfigure *C* of Figure B.1. The background light itself consists out of focus reflections from the glass cover slip.

age is instructive in a number of ways, even if it contains no usable sample data. First, the camera's sensor is underfilled; this is not overly concerning, though, as it is only slightly underfilled, and all the relevant information is captured. However, the irregularity of the illumination area is relevant, as it determines what parts of a sample can be observed. The irregularity, both in shape and in intensity distribution, means that certain parts of a sample may be better illuminated than others. For instance, the lower half of the illuminated area appears slightly brighter than the upper half. Additionally, the pervasive intensity pattern caused by the AOD units is clearly visible, and bears a striking resemblance to the pattern in subfigure *C* - the sine wave - of Fig. B.1.[1]

[1] See Ch. 5.1.2 for a thorough discussion of this subject.

A further complicating factor is positional uncertainty in the illumination beam. Without the ability to know *where* on the image plane the beam is at any given time, it is impossible to correct for any variations in illumination power over the sample caused by the AOD crystals, or any other unforeseen factors.

As mentioned previously, all these factors cause the irregular background that pervades wide-field iSCAT images; imagine Fig. 9.1 overlaid on every sample image. Being able to remove that pattern is a highly desirable goal. Because of the sheer complexity and variability of the background pattern, though, it would be impossible (or, at least, very unwise) to simply designate an arbitrary background file and perform a pixel-by-pixel subtraction to remove it from a sample image.

The advantage of introducing a confocal iSCAT channel, using a single-channel detection method,[2] would be introducing the ability to have a positionally certain, point-by-point reference channel that could be used concurrently with an iSCAT signal channel. The reference/signal coupling allows for background suppression and for correction of laser power fluctuations; more generally phrased, it allows the iSCAT signal to be normalized, both temporally and positionally. Being able to normalize the channel in such a way would increase the instrument's ability to resolve smaller features, due to the reduction in the system's Point Spread Function (PSF).

9.2 Designing a Confocal iSCAT Channel

The basic design principles for a single-channel iSCAT detection system having already been developed, there was not much difficulty in their translation to the new configuration. The detectors would have to be placed before the AOD system; some of the scattered light returning from the sample does pass through the AOD units backwards, thus, adding photodiode detectors there was feasible.

In addition to detectors, a way to read position information into the computer was needed. The function generators' waveform outputs are translated into beam position by the Voltage-Controlled Oscillator (VCO) units and the AOD crystals; if those waveforms could be mathematically related to beam position, simply acquiring those waveforms with a Data Acquisition (DAQ) card would do the trick. Of

[2] See Chs. 3.3.1 and 4.1.

course, since the waveform frequencies are in the kHz range, a very fast DAQ card would be necessary.

9.2.1 Choosing the Right Detector

The first step in designing the configuration was to choose detectors that would actually work with the system. Because of the large number of optics that the beam must pass through, by the time it reaches the photodetector it is exceptionally weak. Thus, highly sensitive detectors were necessary.

The *Nirvana 2007* autobalanced photoreceiver (New Focus Inc., Santa Clara, CA, USA), from the old single-channel configuration, was one possibility for a detector. We also purchased two fixed-gain silicon transimpedance-amplified photodiodes from Thorlabs, Inc. (model name *PDA10A*), one for the signal channel and one for the reference channel. Both, however, proved unsuitable.

The Thorlabs photodiodes could not detect a signal at all, as their bias voltage overwhelmed any photocurrent generated on the detector itself. The autobalanced photoreceiver also had difficulty generating an output signal, since the reference beam was far too powerful for the autobalancing circuitry. Recall from Ch. 3.3.1 that the signal beam should be roughly half as powerful as the reference beam in order to achieve maximum common-mode rejection; this was practically impossible given the optical train, even with the addition of several additional filters. Although some small autobalanced signal could be detected from the photoreceiver, it was so minimal that it was essentially useless.

Eventually, a pair of much more sensitive Silicon Photomultiplier (SiPM) detectors were purchased (model name *MicroFC-SMA-10050*, SensL Technologies Ltd., Cork, Ireland). SiPM detectors are orders of magnitude more sensitive than transimpedance-amplified photodiodes; thus, they function quite well in the low-intensity confocal iSCAT design. Testing the detectors proved their ability to detect the very weak iSCAT signal beam.

9.2.2 Confocal Channel Implementation

Setting up the confocal iSCAT channel required some creative thinking. The first step was to construct a calibration model to relate beam position on the image

plane with function generator outputs. This was done by switching the function generators to output fixed voltages, and recording the resulting spot's location on the wide-field CMOS detector.

The initial design, with only one DAQ card (having two input channels), had been to use one input channel to read from the signal detector, and the other from the reference detector. It very quickly became clear that there was a critical flaw with this design; even though we had the calibration model, it was impossible to actually *use*, since there was no way to know the phase of the function generators' waveforms.

The initial solution to this problem was to switch the function generators to deliver waveform bursts upon receiving a Transistor-Transistor Logic (TTL) signal. They could deliver a maximum of 30,000 waveforms per burst, which at their frequencies near 40 kHz, equated to around 760 ms per burst. The assumption was that each generated burst would have identical phase, so that we would then be able to determine the waveform's phase based on time information alone. However, this did not turn out to be the case; when the DAQ card was reconnected to read out from the function generators, it was clear that the phase was *not* constant for the start of each burst.

The only way to account for this phase problem was thus to purchase a second DAQ card so that the waveforms from the function generators could be recorded concurrently with the signals from the photodetectors. Only then would the calibration model be useful. Having two cards would also obviate the need to use waveform bursts.

Setting up a second DAQ card required precise synchronization between the two. At first, we set up software timing through the LabVIEW interface, but that proved unreliable; there were delays between when the cards started acquisition. Then, we wired one card to trigger the other using hardware timing and a TTL signal, after receiving a digital bit change from the software; this arrangement worked well, as the DAQ cards' hardware clocks are better suited to such tasks.

9.2.3 Reconstructing the Confocal Image

Substantial mathematical manipulation is necessary to acquire an image from this setup. The DAQ cards simply record large arrays of time-coded values from the function generators and photodetectors. This data must then be reconstructed into an image.

A critical problem is that the data is discontinuous; simply reshaping it would yield an array of discrete points. One method to make the reconstructed image appear more realistic is to apply a constrained Gaussian blur to each data point, in order to simulate the PSF of the system. An alternative to a Gaussian blur would be to use a bilateral filter, which would preserve the edges of a feature while removing noise. There are also many stochastic methods reported in the literature for similar image reconstruction. [10, 25, 71, 77]

9.3 Looking Forward

The implementation of the confocal iSCAT channel is far from complete; as with all instrumental designs, it will undergo many refinements and adjustments before it can be called finished. The design and construction processes involved draw from many branches of knowledge; laser physics, chemistry, optics, and software design, to name a few. As the instrument described herein transitions from being a construction project to being a data collector, one can begin to consider where it might be useful.

The advantages of wide-field Interferometric Scattering Microscopy (iSCAT) and confocal Raman, namely label-free and non-destructive sample preparation, and capability for video-rate imaging alongside precise chemical characterization, give the instrument described herein a unique ability to investigate and characterize a wide variety of samples. Pulp and paper samples, as described in Chapter 3.1, are prime examples. Non-destructively imaging live cells in solution, rapidly characterizing surface materials such as graphene, and investigating the uptake of gold nanoparticles by cancerous cells versus healthy cells are more examples of the potential this instrument holds.

It remains an open question, however, if instruments, such as the one described in this thesis, could ever be considered to be “complete”.

Bibliography

[1] C. Connolly, "A review of medical microscopy techniques," *Sensor Review*, vol. 25, pp. 252–258, Dec. 2005. → pages 2

[2] D. J. Stephens and V. J. Allan, "Light microscopy techniques for live cell imaging," *Science*, vol. 300, pp. 82–86, Apr. 2003. → pages 2

[3] E. Thomsen and M. Thomsen, "Darkfield microscopy of living neurosecretory cells," *Cell. Mol. Life Sci.*, vol. 10, pp. 206–207, May 1954. → pages 2

[4] H. E. Rosenberger, "Differential interference contrast microscopy," *Interpretive techniques for microstructural analysis*, pp. 79–104, 1977. → pages 2, 3

[5] F. Zernike, "Phase contrast, a new method for the microscopic observation of transparent objects," *Physica*, vol. 9, pp. 686–698, July 1942. → pages 2

[6] W. Lang, *Nomarski Differential Interference Contrast Microscopy*, pp. 1353–1354. Springer Science + Business Media, 1982. → pages 3

[7] T. G. Rochow and P. A. Tucker, "Interference microscopy," *Introduction to Microscopy by Means of Light*, pp. 221–231, 1994. → pages 3

[8] M. G. L. Gustafsson, "Nonlinear structured-illumination microscopy: Wide-field fluorescence imaging with theoretically unlimited resolution," *Proceedings of the National Academy of Sciences*, vol. 102, pp. 13081–13086, Sept. 2005. → pages 4, 43

[9] M. G. L. Gustafsson, D. A. Agard, and J. W. Sedat, "I5M: 3D widefield light microscopy with better than 100nm axial resolution," *J. Microsc.*, vol. 195, pp. 10–16, July 1999. → pages 4, 42

[10] B. Huang, H. Babcock, and X. Zhuang, "Breaking the diffraction barrier: Super-Resolution imaging of cells," *Cell*, vol. 143, pp. 1047–1058, Dec. 2010. → pages 4, 6, 85

[11] E. Klimov, W. Li, X. Yang, G. G. Hoffmann, and J. Loos, "Scanning near-field and confocal Raman microscopic investigation of p3Ht-PCBM systems for solar cell applications," *Macromolecules*, vol. 39, pp. 4493–4496, June 2006. → pages 4, 13

[12] L. Schermelleh and R. Heintzmann, "A guide to super-resolution fluorescence microscopy," *The Journal of cell* , vol. 190, pp. 165–175, July 2010. → pages 4, 6

[13] R. Böhme, M. Richter, D. Cialla, P. Rsch, V. Deckert, and J. Popp, "Towards a specific characterisation of components on a cell surface-combined TERS-investigations of lipids and human cells," *J. Raman Spectrosc.*, vol. 40, pp. 1452–1457, Oct. 2009. → pages 4, 5

[14] K. Domke and B. Pettinger, "Studying surface chemistry beyond the diffraction limit: 10 years of TERS," *ChemPhysChem*, vol. 11, pp. 1365–1373, May 2010. → pages 4, 5

[15] C. Blum, T. Schmid, L. Opilik, S. Weidmann, S. R. Fagerer, and R. Zenobi, "Understanding tip-enhanced Raman spectra of biological molecules: a combined Raman, SERS and TERS study," *J. Raman Spectrosc.*, vol. 43, pp. 1895–1904, June 2012. → pages 5

[16] J. Chen, M. Badioli, and A. P, "Optical nano-imaging of gate-tunable graphene plasmons," *Nature*, 2012. → pages 5

[17] S. Lal, S. Link, and N. Halas, "Nano-optics from sensing to waveguiding," *Nature photonics*, 2007. → pages 5

[18] D. A. Skoog, F. J. Holler, and S. R. Crouch, *Principles of Instrumental Analysis*. Brooks/Cole, 6th ed., 2007. → pages xi, 5, 15

[19] Z. Fei, A. Rodin, G. Andreev, W. Bao, M. AS, M. Wagner, L. Zhang, Z. Zhao, M. Thiemens, and G. Dominguez, "Gate-tuning of graphene plasmons revealed by infrared nano-imaging," *Nature*, vol. 487, no. 7405, pp. 82–85, 2012. → pages 5

[20] M. Qazilbash, M. Brehm, G. Andreev, and A. Frenzel, "Infrared spectroscopy and nano-imaging of the insulator-to-metal transition in vanadium dioxide," *Physical Review B*, 2009. → pages 5

[21] J. Samson, G. Wollny, and E. Bründermann, "Setup of a scanning near field infrared microscope (SNIM): imaging of sub-surface nano-structures in gallium-doped silicon," *Physical Chemistry* , 2006. → pages 5

[22] S. W. Hell and J. Wichmann, "Breaking the diffraction resolution limit by stimulated emission: stimulated-emission-depletion fluorescence microscopy," *Opt. Lett.*, vol. 19, p. 780, June 1994. → pages 6

[23] S. W. Hell, "Far-field optical nanoscopy," *Science*, vol. 316, pp. 1153–1158, May 2007. → pages 6

[24] M. A. Schwentker, H. Bock, M. Hofmann, S. Jakobs, J. Bewersdorf, C. Eggeling, and S. W. Hell, "Wide-field subdiffraction RESOLFT microscopy using fluorescent protein photoswitching," *Microsc. Res. Tech.*, vol. 70, no. 3, pp. 269–280, 2007. → pages 6, 44

[25] J. Tønnesen and U. V. Nägerl, "Superresolution imaging for neuroscience," *Exp. Neurol.*, vol. 242, pp. 33–40, Apr. 2013. → pages 6, 85

[26] C. G. Galbraith and J. A. Galbraith, "Super-resolution microscopy at a glance," *J. Cell Sci.*, vol. 124, pp. 1607–1611, May 2011. → pages 6

[27] J. Lippincott-Schwartz and S. Manley, "Putting super-resolution fluorescence microscopy to work," *Nat. Methods*, vol. 6, pp. 21–23, Jan. 2009. → pages 6

[28] J. Ortega-Arroyo and P. Kukura, "Interferometric scattering microscopy (iSCAT): new frontiers in ultrafast and ultrasensitive optical microscopy.," *Physical Chemistry Chemical Physics : PCCP*, vol. 14, no. 45, pp. 15625–15636, 2012. → pages 8, 9, 10, 11, 21, 22, 44, 59

[29] J. Ortega-Arroyo, *Investigation of Nanoscopic Dynamics and Potentials by Interferometric Scattering Microscopy*. PhD thesis, St. Hugh's College, University of Oxford, 2015. → pages 9, 10, 11

[30] E. Atılgan and B. Ovryn, "Reflectivity and topography of cells grown on glass-coverslips measured with phase-shifted laser feedback interference microscopy," *Biomed. Opt. Express*, vol. 2, pp. 2417–37, July 2011. → pages 10

[31] J. H. Seinfeld and S. N. Pandis, *Atmospheric Chemistry and Physics: From Air Pollution to Climate Change*. John Wiley & Sons, Inc., 2 ed., 2006. → pages 11

[32] R. H. Webb, "Confocal optical microscopy," *Rep. Prog. Phys.*, vol. 59, pp. 427–471, Mar. 1996. → pages 12

[33] N. J. Everall, "Confocal Raman microscopy: Performance, pitfalls, and best practice," *Appl. Spectrosc.*, vol. 63, pp. 245–262, Sept. 2009. → pages 13, 26

[34] N. J. Everall, "Confocal Raman microscopy : common errors and artefacts," *The Analyst*, vol. 135, no. 10, pp. 2512–2522, 2010. → pages 13

[35] E. M. Ali, H. G. Edwards, and I. J. Scowen, "In-situ detection of single particles of explosive on clothing with confocal Raman microscopy," *Talanta*, vol. 78, pp. 1201–1203, May 2009. → pages 13

[36] A. Belu, C. Mahoney, and K. Wormuth, "Chemical imaging of drug eluting coatings: Combining surface analysis and confocal Raman microscopy," *J. Controlled Release*, vol. 126, pp. 111–121, Mar. 2008. → pages 13

[37] T. E. Bridges, M. P. Houlne, and J. M. Harris, "Spatially resolved analysis of small particles by confocal Raman microscopy: depth profiling and optical trapping," *Anal. Chem.*, vol. 76, pp. 576–584, Feb. 2004. → pages 13

[38] J. Choi, J. Choo, H. Chung, D.-G. Gweon, J. Park, H. J. Kim, S. Park, and C.-H. Oh, "Direct observation of spectral differences between normal and basal cell carcinoma (BCC) tissues using confocal Raman microscopy," *Biopolymers*, vol. 77, no. 5, pp. 264–272, 2005. → pages 13

[39] J. V. Glenn, J. R. Beattie, L. Barrett, N. Frizzell, S. R. Thorpe, M. E. Boulton, J. J. McGarvey, and A. W. Stitt, "Confocal Raman microscopy can quantify advanced glycation end product (AGE) modifications in bruch's membrane leading to accurate, nondestructive prediction of ocular aging," *The FASEB Journal*, vol. 21, pp. 3542–3552, Nov. 2007. → pages 13

[40] M. P. Houlne, C. M. Sjostrom, R. H. Uibel, J. A. Kleimeyer, and J. M. Harris, "Confocal Raman microscopy for monitoring chemical reactions on single optically trapped, solid-phase support particles," *Anal. Chem.*, vol. 74, pp. 4311–4319, Sept. 2002. → pages 13

[41] W. Schrof, E. Beck, R. Kniger, W. Reich, and R. Schwalm, "Depth profiling of UV cured coatings containing photostabilizers by confocal Raman microscopy," *Prog. Org. Coat.*, vol. 35, pp. 197–204, Aug. 1999. → pages 13

[42] P. Caspers, G. Lucassen, and G. Puppels, "Combined in vivo confocal Raman spectroscopy and confocal microscopy of human skin," *Biophys. J.*, vol. 85, pp. 572–580, July 2003. → pages 13

[43] L. Chrit, C. Hadjur, S. Morel, G. Sockalingum, G. Lebourdon, F. Leroy, and M. Manfait, "In vivo chemical investigation of human skin using a confocal Raman fiber optic microprobe," *J. Biomed. Opt.*, vol. 10, no. 4, p. 044007, 2005. → pages 13

[44] K. Klein, A. M. Gigler, T. Aschenbrenner, R. Monetti, W. Bunk, F. Jamitzky, G. Morfill, R. W. Stark, and J. Schlegel, "Label-free live-cell imaging with confocal Raman microscopy," *Biophys. J.*, vol. 102, pp. 360–368, Jan. 2012. → pages 13

[45] N. Tavassoli, Z. Chen, A. Bain, L. Melo, D. Chen, and E. R. Grant, "Template-oriented genetic algorithm feature selection of analyte wavelets in the Raman spectrum of a complex mixture," *Anal. Chem.*, vol. 86, pp. 10591–10599, Nov. 2014. PMID: 25260090. → pages xv, 18, 79

[46] N. Wistara and R. Young, "Properties and treatments of pulps from recycled paper. part I. physical and chemical properties of pulps," *Cellulose*, vol. 6, pp. 291–324, 1999. → pages 18

[47] L. Safranyik and B. Wilson, *The mountain pine beetle: a synthesis of biology, management and impacts on lodgepole pine*. Pacific Forestry Centre, Canadian Forest Service, Natural Resources Canada, 2006. → pages 19

[48] TEMAP, "Fibre Morphology." Online, 2007. TEMAP is a division of Canfor Pulp Ltd. (Vancouver, BC, Canada). → pages 19

[49] P. Watson and M. Bradley, "Canadian pulp fibre morphology: superiority and considerations for end use potential," *The Forestry Chronicle*, vol. 85, pp. 401–408, June 2009. → pages xiii, 19

[50] TEMAP, "Premium reinforcement pulp: Glossary of terms." Online, n.d. → pages 19

[51] N. Tavassoli, W. Tsai, P. Bicho, and E. R. Grant, "Multivariate classification of pulp NIR spectra for end-product properties using discrete wavelet transform with orthogonal signal correction," *Anal. Methods*, vol. 6, pp. 8906–8914, July 2014. → pages 20, 76

[52] U. P. Agarwal, R. R. Reiner, and S. A. Ralph, "Estimation of cellulose crystallinity of lignocelluloses using Near-IR FT-Raman spectroscopy and comparison of the Raman and Segal-WAXS methods," *J. Agric. Food. Chem.*, vol. 61, pp. 103–113, Jan. 2013. → pages 20

[53] G. Downes, R. Meder, C. Hicks, and N. Ebdon, "Developing and evaluating a multisite and multispecies NIR calibration for the prediction of kraft pulp yield in eucalypts," *Southern Forests: a Journal of Forest Science*, vol. 71, pp. 155–164, June 2009. → pages 20

[54] N. Durán and R. Angelo, "Infrared microspectroscopy in the pulp and Paper-Making industry," *Appl. Spectrosc. Rev.*, vol. 33, pp. 219–236, Aug. 1998. → pages 20

[55] P. Fardim, M. M. C. Ferreira, and N. Durán, "Determination of mechanical and optical properties of eucalyptus kraft pulp by NIR spectrometry and multivariate calibration," *J. Wood Chem. Technol.*, vol. 25, pp. 267–279, Oct. 2005. → pages 20

[56] A. J. Hobro, J. Kuligowski, M. Dll, and B. Lendl, "Differentiation of walnut wood species and steam treatment using ATR-FTIR and partial least squares discriminant analysis (PLS-DA)," *Anal. Bioanal.Chem.*, vol. 398, pp. 2713–2722, Sept. 2010. → pages 20

[57] S. S. Kelley, T. G. Rials, R. Snell, L. H. Groom, and A. Sluiter, "Use of near infrared spectroscopy to measure the chemical and mechanical properties of solid wood," *Wood Sci. Technol.*, vol. 38, May 2004. → pages 20

[58] J. J. Workman, "Infrared and Raman spectroscopy in paper and pulp analysis," *Appl. Spectrosc. Rev.*, vol. 36, pp. 139–168, June 2001. → pages 20

[59] D. B. Chase, "Fourier transform Raman spectroscopy.," *J. Am. Chem. Soc.*, vol. 108, pp. 7485–7488, Nov. 1986. → pages 20, 21

[60] P. Matousek, M. Towrie, and A. W. Parker, "Fluorescence background suppression in Raman spectroscopy using combined Kerr gated and shifted excitation Raman difference techniques," *Journal of Raman Spectroscopy*, vol. 33, no. 4, pp. 238–242, 2002. → pages 20

[61] A. C. Albrecht, "On the dependence of vibrational Raman intensity on the wavelength of incident light," *The Journal of Chemical Physics*, vol. 55, no. 9, p. 4438, 1971. → pages 21

[62] J. E. Pemberton and R. L. Sobocinski, "Raman spectroscopy with helium-neon laser excitation and charge-coupled device detection," *J. Am. Chem. Soc.*, vol. 111, pp. 432–434, Jan. 1989. → pages 21

[63] P. A. Laplante, *Comprehensive Dictionary of Electrical Engineering*. CRC Press, 2nd ed., 2005. → pages 21

[64] New Focus, Inc., 2630 Walsh Av., Santa Clara, CA, USA 95051, *Nirvana Auto-Balanced Photoreceivers - Model 2007 & 2017 User's Manual*, n.d. → pages 22, 23, 29

[65] T. M. Niebauer, J. E. Faller, H. M. Godwin, J. L. Hall, and R. L. Barger, "Frequency stability measurements on polarization-stabilized he–ne lasers," *Appl. Opt.*, vol. 27, pp. 1285–1289, Apr. 1988. → pages 22

[66] J. Dubessy, M.-C. Caumon, F. Rull, and S. Sharma, *Instrumentation in Raman spectroscopy*, vol. 12 of *EMU Notes in Mineralogy*, ch. 3, pp. 83–172. Mineralogical Society, 2012. → pages 26

[67] E. Vignati, M. Facchini, M. Rinaldi, C. Scannell, D. Ceburnis, J. Sciare, M. Kanakidou, S. Myriokefalitakis, F. Dentener, and C. O'Dowd, "Global scale emission and distribution of sea-spray aerosol: Sea-salt and organic enrichment," *Atmos. Environ.*, vol. 44, pp. 670–677, Feb. 2010. → pages 37

[68] C. L. Haynes, A. D. McFarland, and R. P. V. Duyne, "Surface-Enhanced Raman spectroscopy," *Anal. Chem.*, vol. 77, pp. 338–346, Sept. 2005. → pages 38, 57

[69] B. Pettinger, G. Picardi, R. Schuster, and G. Ertl, "Surface-enhanced and STM-tip-enhanced Raman spectroscopy at metal surfaces," *Single Molecules*, vol. 3, pp. 285–294, Nov. 2002. → pages 38, 56, 57

[70] D. Karadaglić and T. Wilson, "Image formation in structured illumination wide-field fluorescence microscopy," *Micron*, vol. 39, pp. 808–818, Oct. 2008. → pages 42, 43

[71] E. B. van Munster, L. J. van Vliet, and J. A. Aten, "Reconstruction of optical pathlength distributions from images obtained by a wide field differential interference contrast microscope," *J. Microsc.*, vol. 188, pp. 149–157, Nov. 1997. → pages 42, 85

[72] S. Schlcker, M. D. Schaeberle, S. W. Huffman, and I. W. Levin, "Raman microspectroscopy: a comparison of point, line, and wide-field imaging

methodologies," *Anal. Chem.*, vol. 75, pp. 4312–4318, Aug. 2003. → pages 42

[73] J. R. Swedlow and M. Platani, "Live cell imaging using wide-field microscopy and deconvolution," *Cell Struct. Funct.*, vol. 27, no. 5, pp. 335–341, 2002. → pages 42

[74] I. Toytman, K. Cohn, T. Smith, D. Simanovskii, and D. Palanker, "Wide-field coherent anti-Stokes Raman scattering microscopy with non-phase-matching illumination," *Opt. Lett.*, vol. 32, p. 1941, June 2007. → pages 42

[75] R. H. Zander and P. M. Eckel, "Bryophyte flora of North America," in *Flora of North America North of Mexico* (F. of North America Editorial Committee, ed.), vol. 27, Flora of North America Association, 2007. → pages 52

[76] Thorlabs Inc., "QTH10 Emission Spectrum." Online, n.d. → pages 61

[77] S. Ayas, G. Cinar, A. D. Ozkan, Z. Soran, O. Ekiz, D. Kocaay, A. Tomak, P. Toren, Y. Kaya, I. Tunc, H. Zareie, T. Tekinay, A. B. Tekinay, M. O. Guler, and A. Dana, "Label-Free Nanometer-Resolution imaging of biological architectures through Surface Enhanced Raman Scattering," *Sci. Rep.*, vol. 3, p. 2624, Sept. 2013. → pages 57, 85

[78] F. L. McCrakin, E. Passaglia, R. R. Stromberg, and H. L. Steinberg, "Measurement of the thickness and refractive index of very thin films and the optical properties of surfaces by ellipsometry," *Journal of Research of the National Bureau of Standards A*, vol. 67A, pp. 363–377, July 1963. → pages 59

[79] D. Graf, F. Molitor, K. Ensslin, C. Stampfer, A. Jungen, C. Hierold, and L. Wirtz, "Spatially resolved Raman spectroscopy of single- and few-layer graphene," *Nano Lett.*, vol. 7, pp. 238–242, Feb. 2007. → pages 72

[80] L. Malard, M. Pimenta, G. Dresselhaus, and M. Dresselhaus, "Raman spectroscopy in graphene," *Phys. Rep.*, vol. 473, pp. 51–87, Apr. 2009. → pages 72

[81] D. R. K. Brownrigg, "The weighted median filter," *Communications of the ACM*, vol. 27, pp. 807–818, Aug. 1984. → pages 75

[82] V. J. Barclay, R. F. Bonner, and I. P. Hamilton, "Application of wavelet transforms to experimental spectra: smoothing, denoising, and data set compression," *Anal. Chem.*, vol. 69, pp. 78–90, Jan. 1997. → pages 76

[83] D. Chen, Z. Chen, and E. Grant, "Adaptive wavelet transform suppresses background and noise for quantitative analysis by Raman spectrometry," *Anal. Bioanal.Chem.*, vol. 400, pp. 625–634, Feb. 2011. → pages 76, 108

[84] Y. L. Loethen, D. Zhang, R. N. Favors, S. B. G. Basiaga, and D. Ben-Amotz, "Second-Derivative variance minimization method for automated spectral subtraction," *Appl. Spectrosc.*, vol. 58, pp. 272–278, Mar. 2004. → pages xiv, 77, 109

[85] I. M. Power, S. A. Wilson, A. L. Harrison, G. M. Dipple, J. McCutcheon, G. Southam, and P. A. Kenward, "A depositional model for hydromagnesite–magnesite playas near Atlin, British Columbia, Canada," *Sedimentology*, vol. 61, pp. 1701–1733, June 2014. → pages 78

[86] S. Wold, K. Esbensen, and P. Geladi, "Principal component analysis," *Chemom. Intell. Lab. Syst.*, vol. 2, pp. 37–52, Aug. 1987. → pages 77

[87] J. H. Kalivas, "Multivariate calibration, an overview," *Anal. Lett.*, vol. 38, pp. 2259–2279, Nov. 2005. → pages xiv, 77

[88] Y.-H. Yun, D.-S. Cao, M.-L. Tan, J. Yan, D.-B. Ren, Q.-S. Xu, L. Yu, and Y.-Z. Liang, "A simple idea on applying large regression coefficient to improve the genetic algorithm-PLS for variable selection in multivariate calibration," *Chemom. Intell. Lab. Syst.*, vol. 130, pp. 76–83, Jan. 2013. → pages 77

[89] D. Chen, Z. Chen, and E. R. Grant, "Adaptive multiscale regression for reliable Raman quantitative analysis," *The Analyst*, vol. 137, no. 1, pp. 237–244, 2012. → pages 79

[90] O. Svensson, T. Kourti, and J. F. MacGregor, "An investigation of orthogonal signal correction algorithms and their characteristics," *J. Chemom.*, vol. 16, no. 4, pp. 176–188, 2002. → pages xiii, 79

[91] A. Palm, "Raman spectrum of polystyrene.," *The Journal of Physical Chemistry*, vol. 55, pp. 1320–1324, Aug. 1951. → pages 97

[92] P. Gillet, C. Biellmann, B. Reynard, and P. McMillan, "Raman spectroscopic studies of carbonates part I: High-pressure and high-temperature behaviour of calcite, magnesite, dolomite and aragonite," *Phys. Chem. Miner.*, vol. 20, May 1993. → pages 98

Appendix A

Raman Map Reader Program: RMR.VI

This appendix contains images of the LabVIEW Virtual Instrument (VI) used to read iSCAT-Raman maps generated by the old instrument, as well as the MATLAB code of dependencies. LabVIEW's dataflow programming language - *G* - cannot be translated to code, so images of the block diagram and its various structures are the only way it can be recorded.

The use of this VI are outlined in Chapters 3.5.2 and 4.2. The first dependency *DWT Single.VI* contains code to apply a simple Discrete Wavelet Transform (DWT) to the data. The second dependency *SDVM Matlab.VI* applies Second-Derivative Variance Minimization (SDVM) to Raman spectra to remove background contributions.

Raman Map Reader EXE.vi

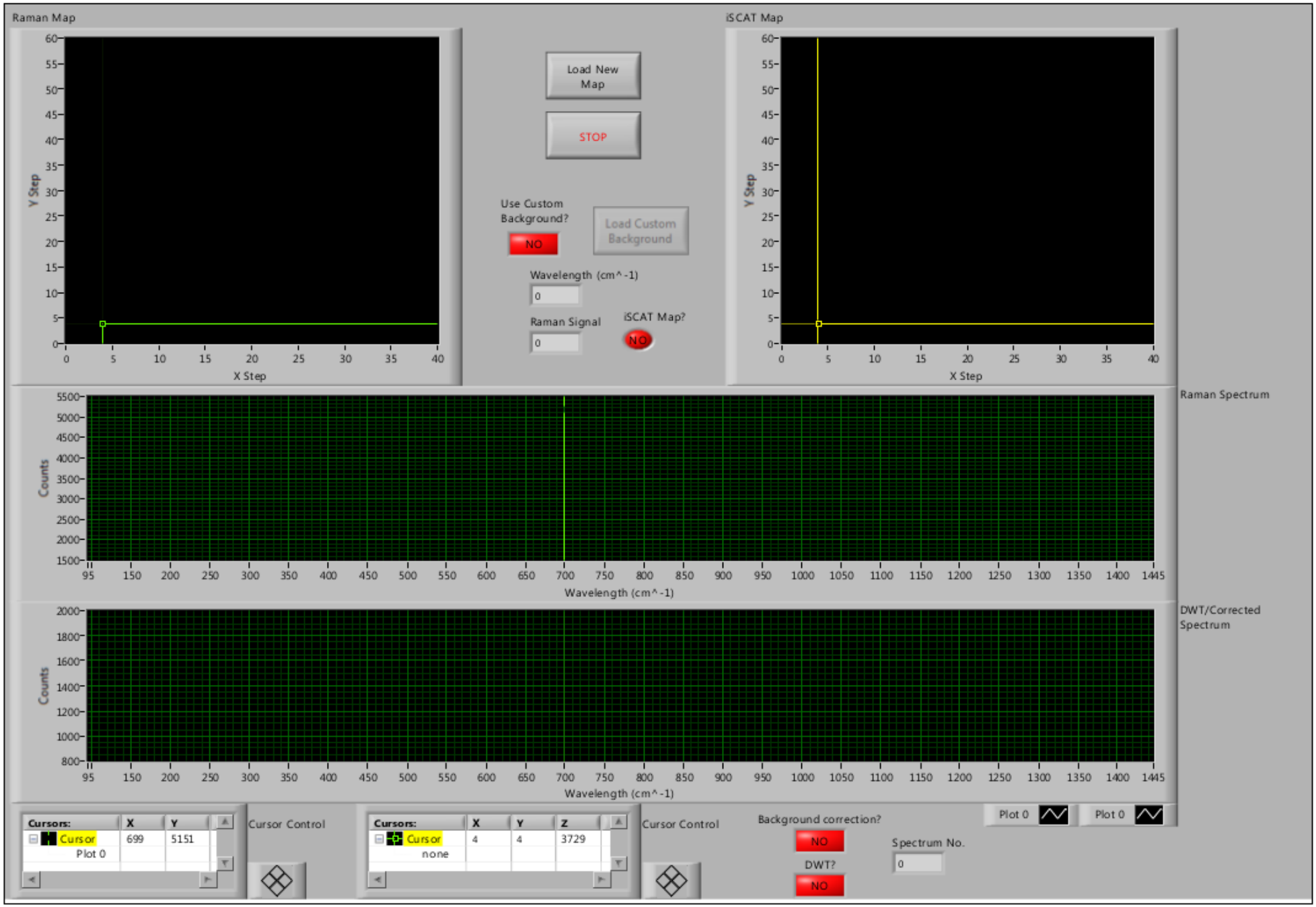

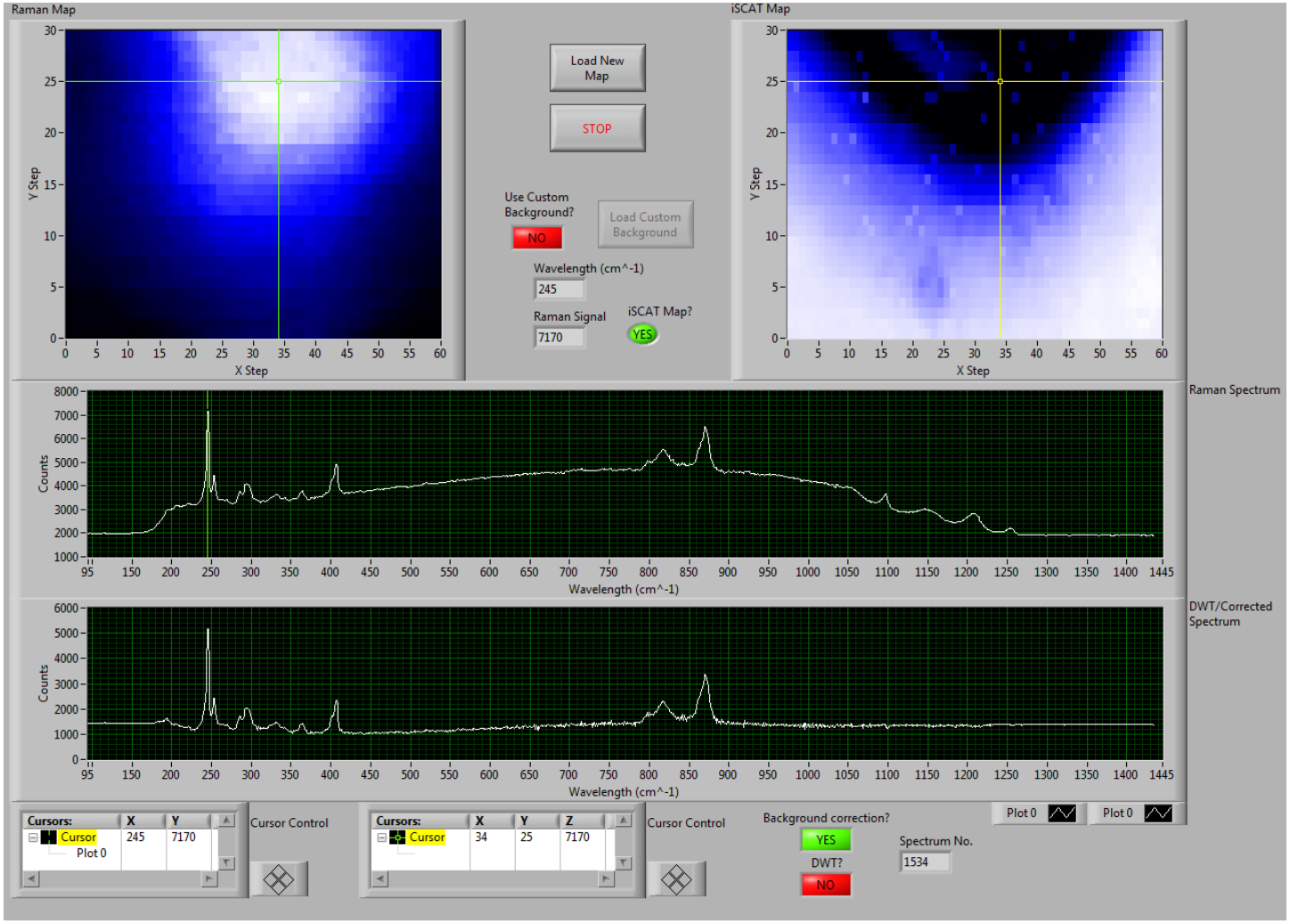

Figure A.1: RMR.VI in use, showing the Raman distribution of a characteristic polystyrene peak near 1000 cm^{-1}. [91] The polystyrene peaks dominate the acquired spectrum and reconstructed map (top left). The Raman exposure time was 25 seconds. See also Figs. 4.4 and 8.3.

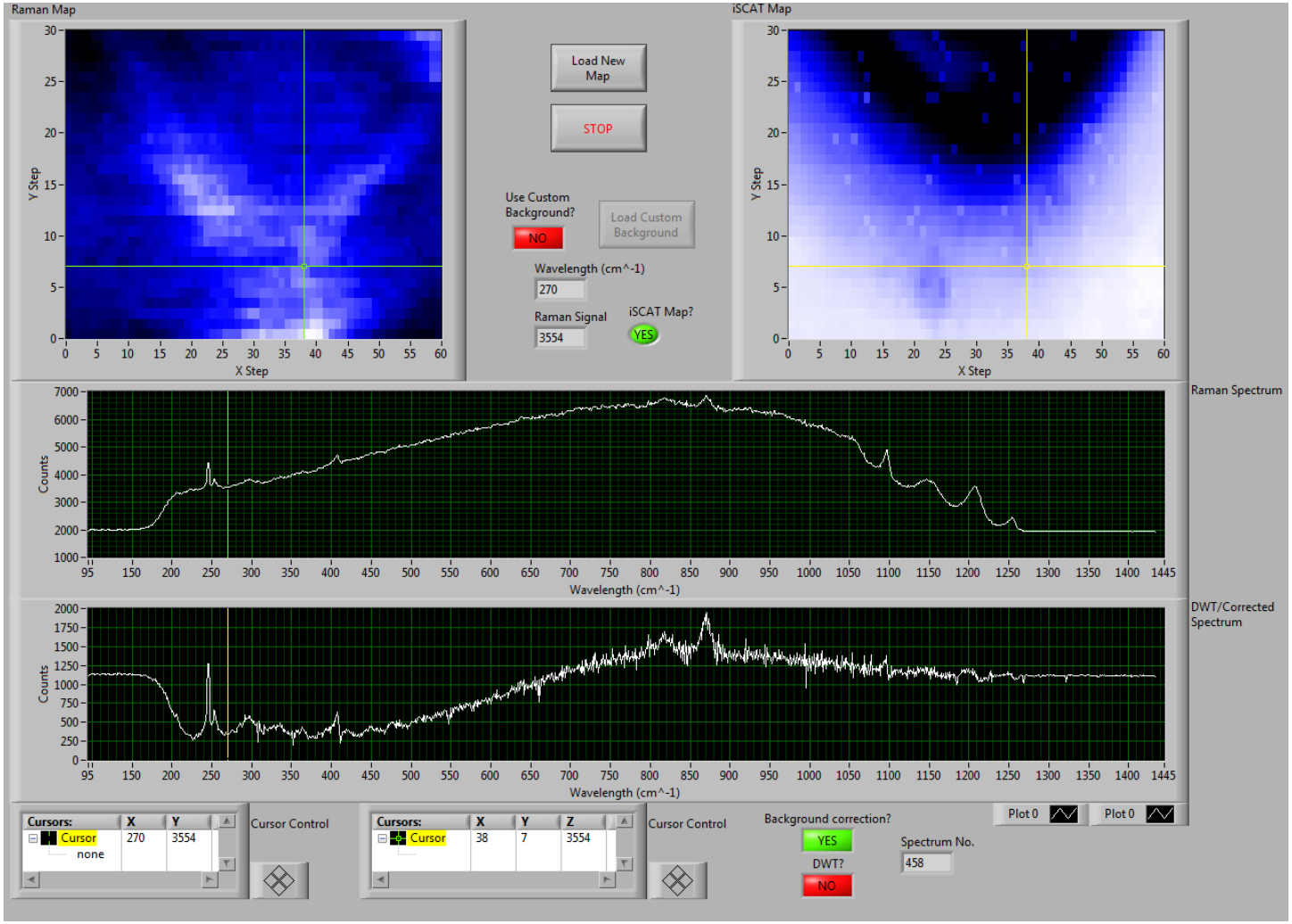

Figure A.2: RMR.VI in use, showing the Raman distribution of a characteristic magnesite peak near 1095 cm^{-1}. [92] Any magnesite peaks are overwhelmed by polystyrene and glass fluorescence, and cannot be observed in the acquired spectrum without processing. The Raman exposure time was 25 seconds. See also Figs. 4.4 and 8.3.

Raman Map Reader EXE.vi

Block Diagram

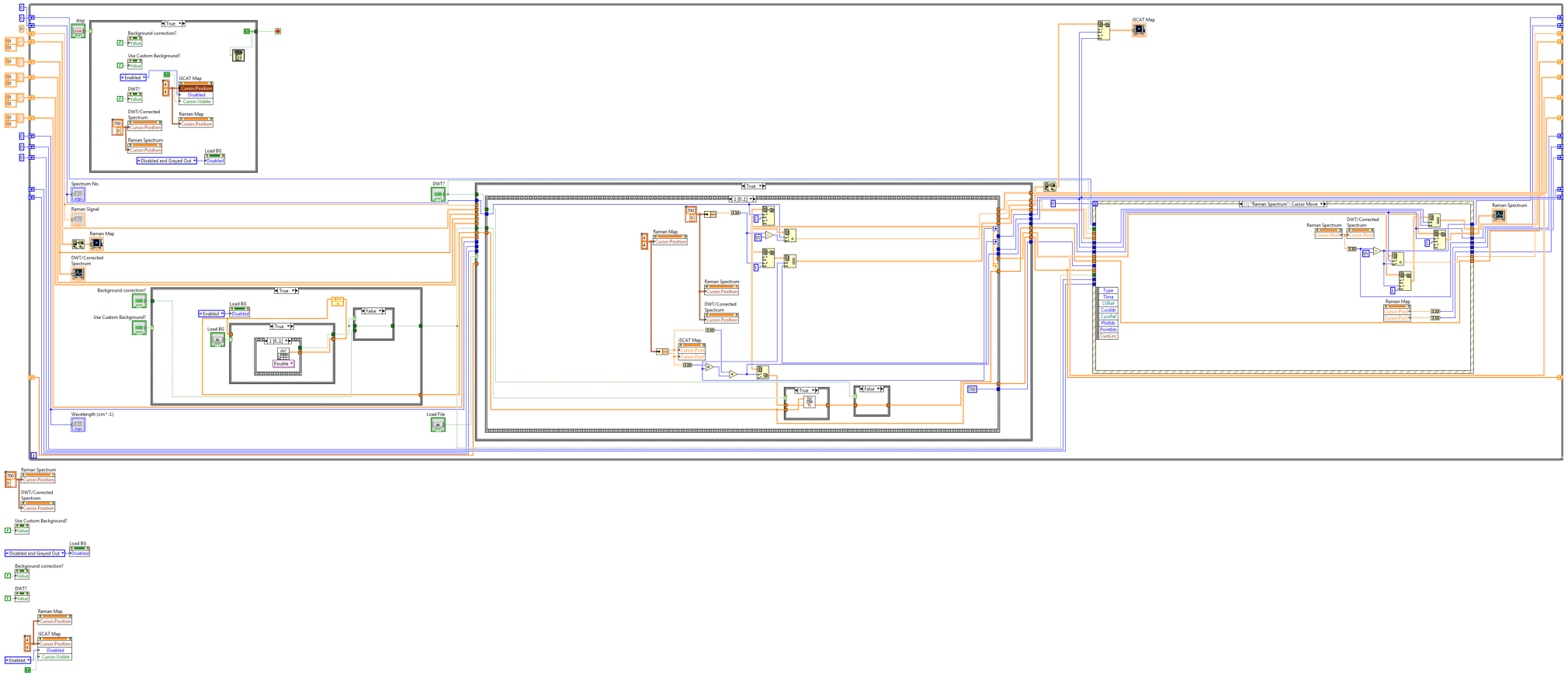

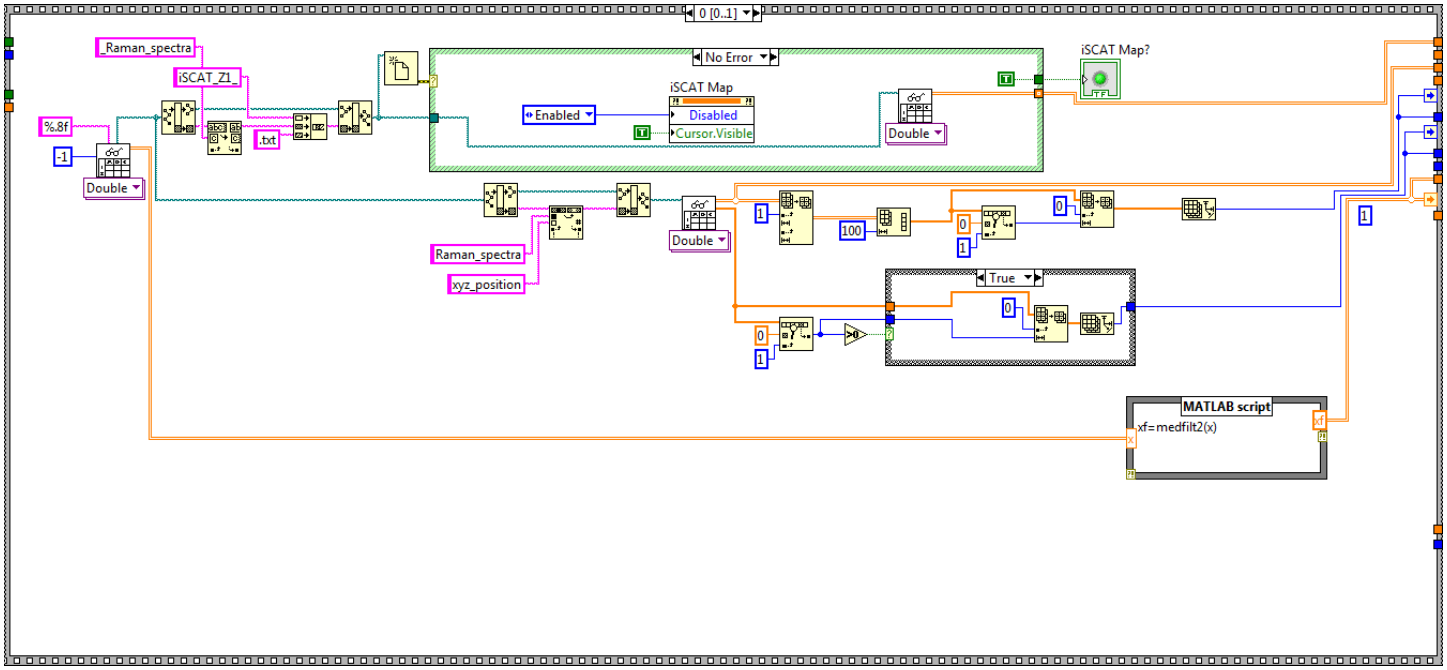

Figure A.3: Load File (Sequence 1 of 2) - *Detect and Load Files into Memory, Apply Median Filter*

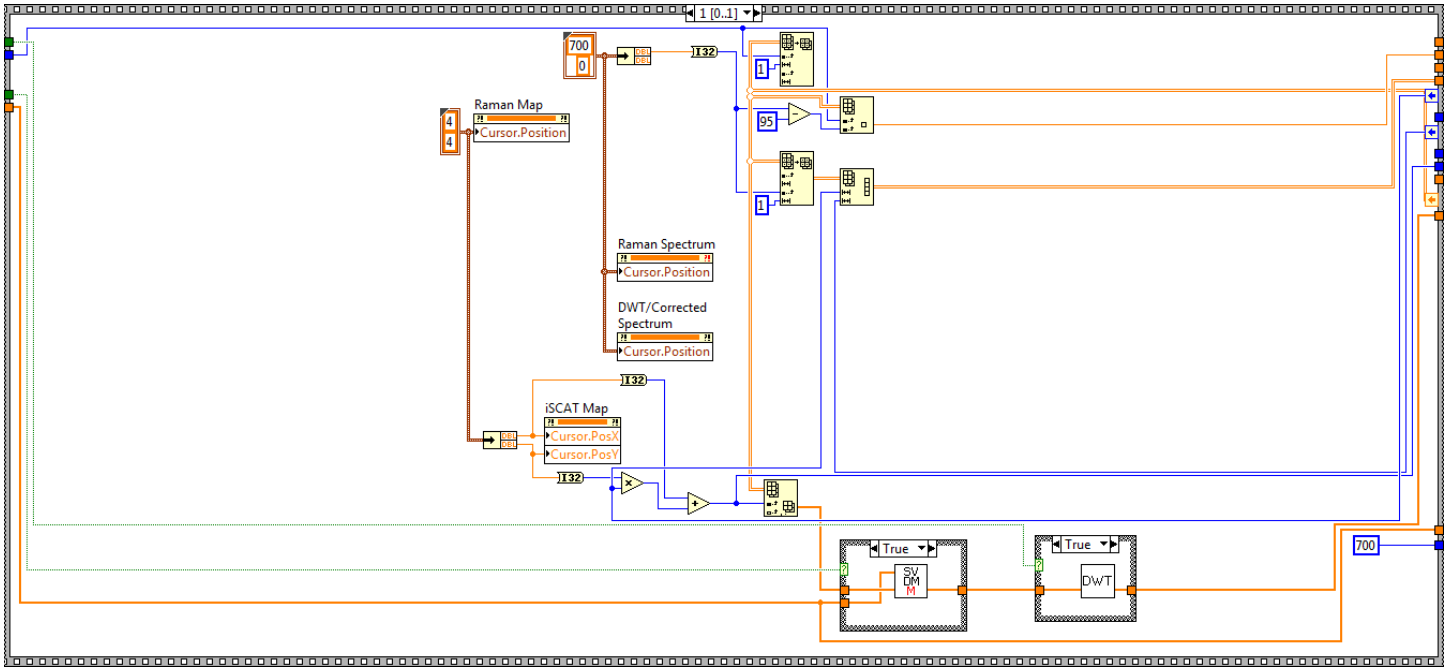

Figure A.4: Load File (Sequence 2 of 2) - *Read Cursor Position and Update Display, Apply Processing (*SVDM *and* DWT*; See Below for Block Diagrams of Processing* VIs*)*

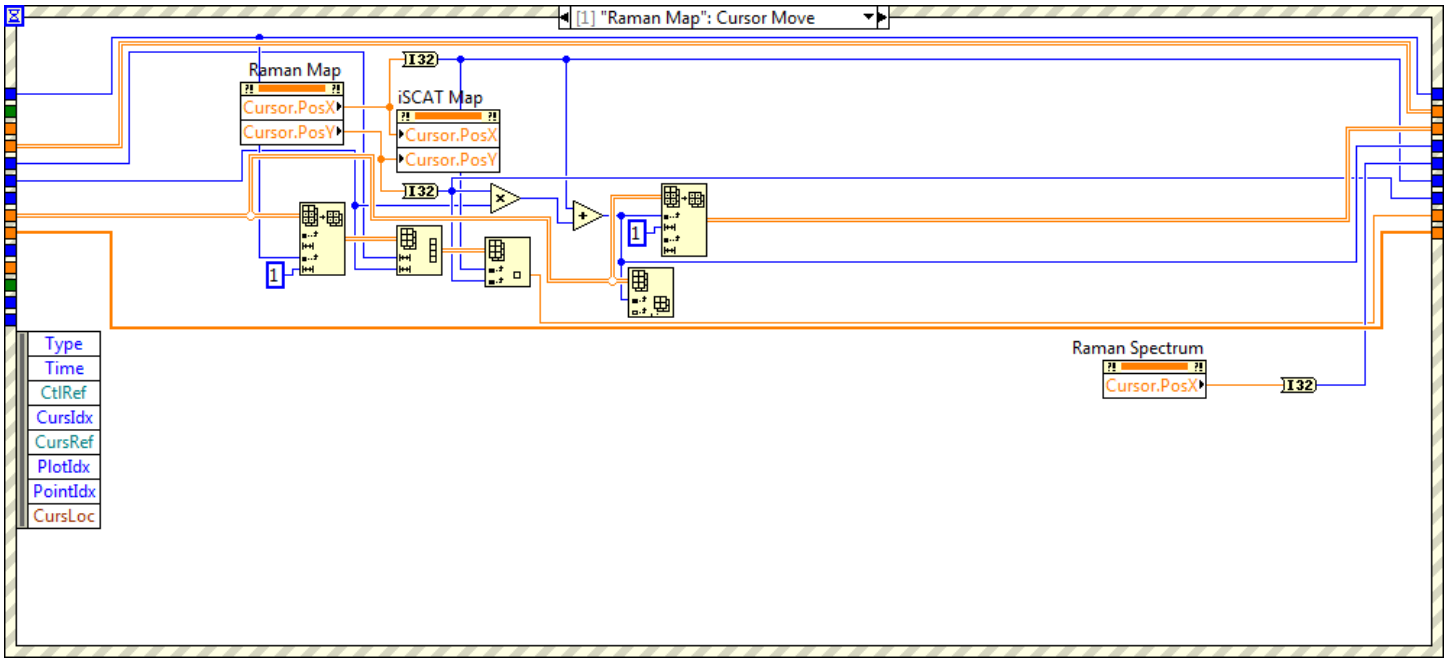

Figure A.5: Raman Map Cursor Move

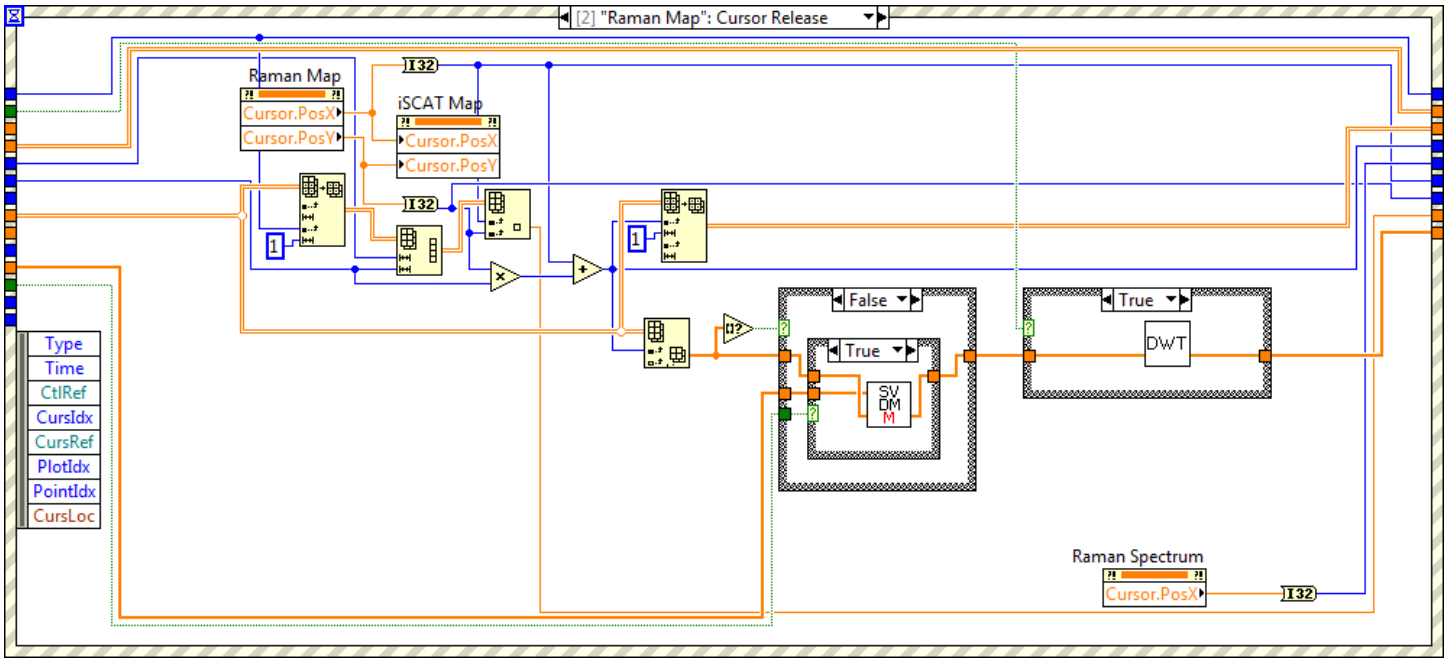

Figure A.6: Raman Map Cursor Release

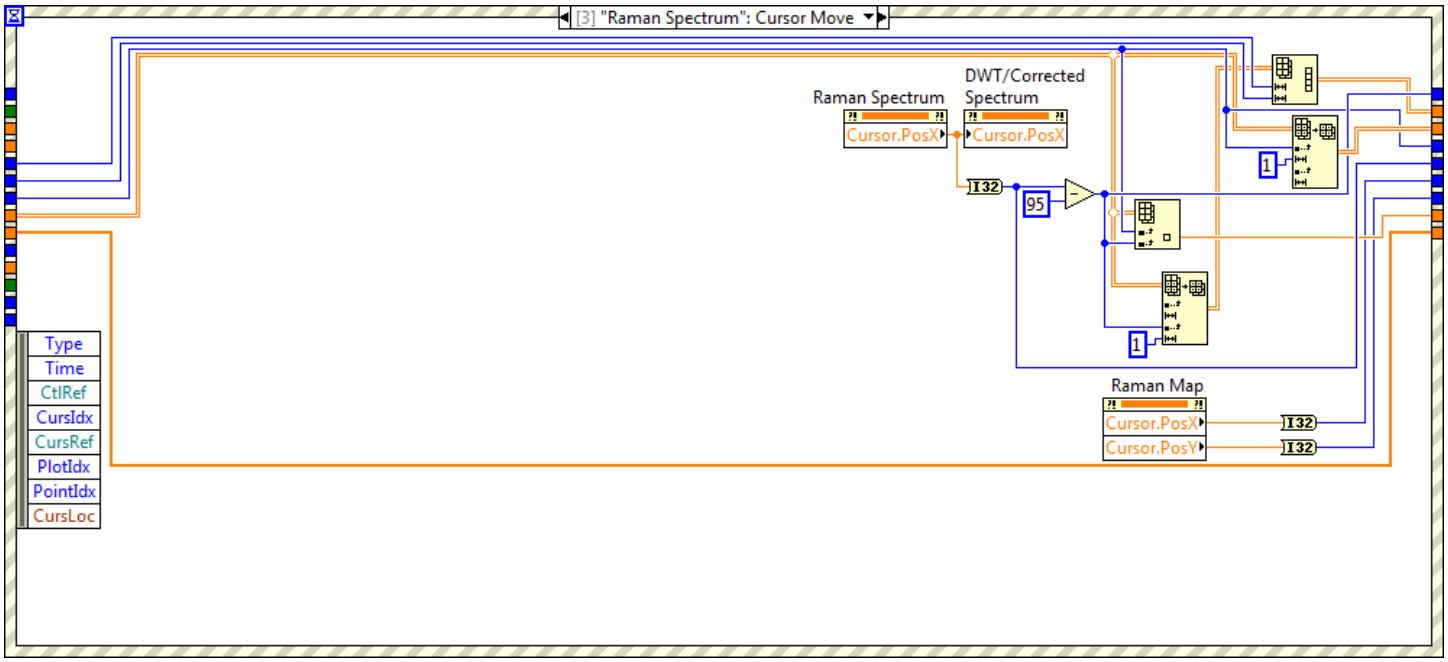

Figure A.7: Raman Spectrum Cursor Move

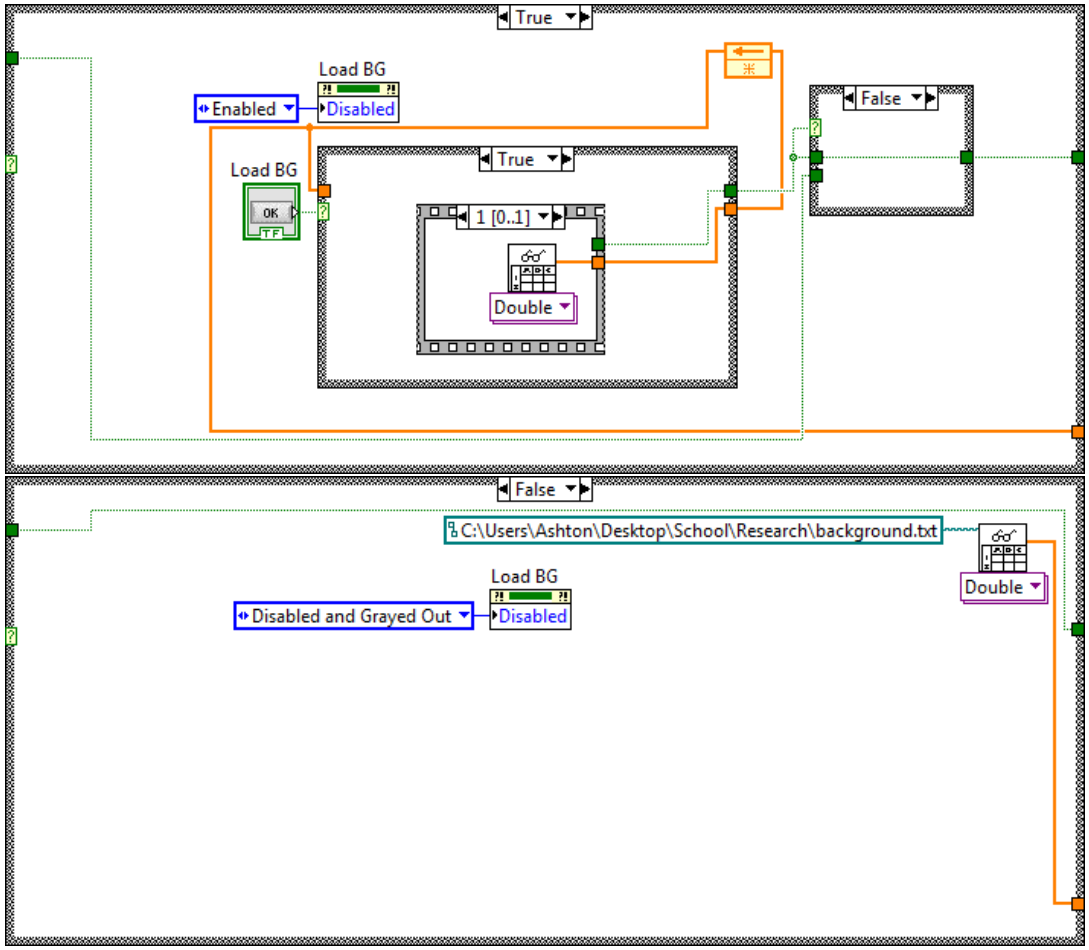

Figure A.8: Use Custom Background File?

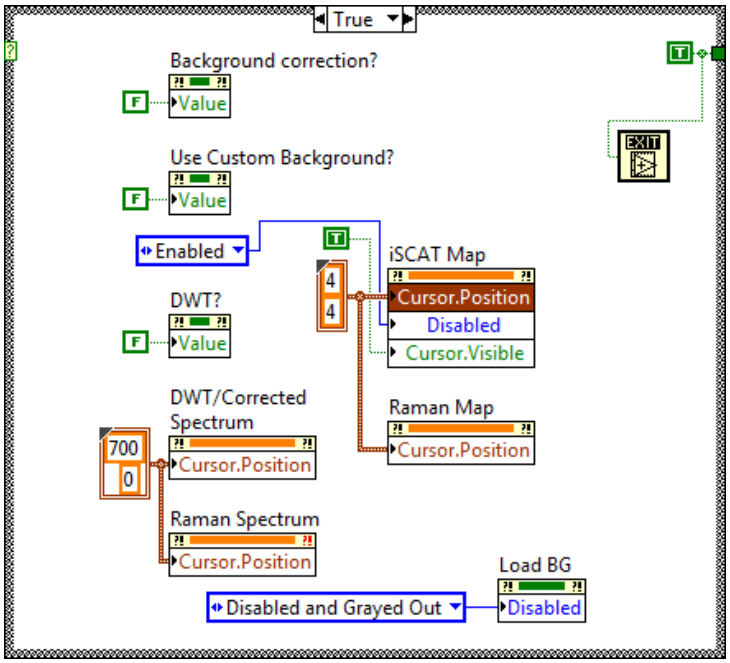

Figure A.9: Stop Program

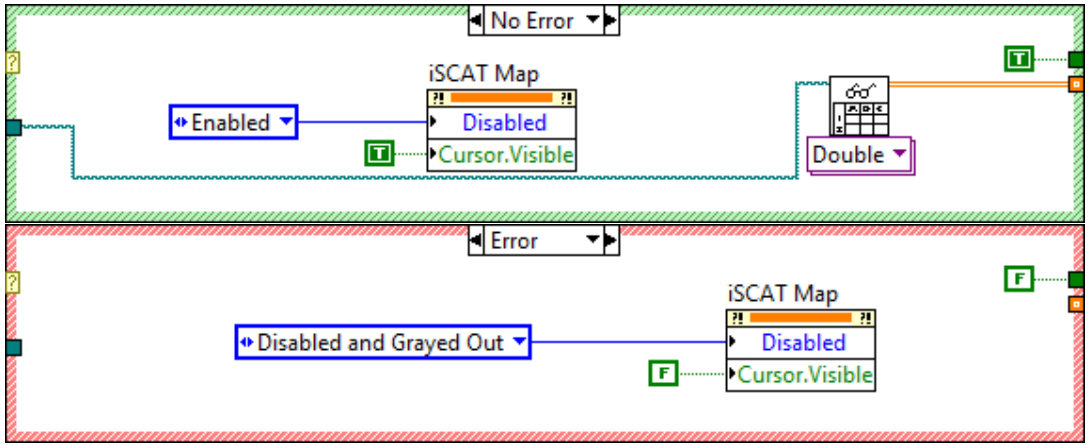

Figure A.10: Error Handling - File(s) Not Found

A.2 *DWT Single.VI*

Note: the dwt_rebu *function was developed by Daniel Da Chen,* [83] *a former student in the research group, and is beyond the scope of this thesis.*

```
%%%%%%%%%%%%%%%%%%
% MATLAB code: DWT Single.VI
%
% Discrete Wavelet Transform
%
% LabVIEW inputs: data
% LabVIEW outputs: wavedata
%

p=path;
path(p,'C:\...\VIs\')    %Actual path to dwt_rebu.m omitted
[wavedata, wcoefs]=dwt_rebu(data,'sym5',5,2);    %Execute DWT using sym5 wavelet
```

A.3 *SDVM Matlab.VI*

This code is based on a previously published SDVM methodology. [84]

```
%%%%%%%%%%%%%%%%%%
% MATLAB code: SDVM Matlab.VI
% by Ashton Christy, 18 Nov 2013
%
% Second-Derivative Variance Minimization
%
% LabVIEW inputs: Signal -> I ; Background -> A0
% LabVIEW outputs: Bf -> Data
%
% I = (c00-c)A0 + B
% signal = scale (best guess - modifier) * background + data
% => B = I - (c00-c)A0
%

c0=1;   %Initial Guess (minimum)
c00=10000;  %Initial Guess (maximum)
c0t=c0; %Index
n=1;    %Index

% Input I, A0 from LabVIEW (signal, background)

sdI=std(I); %Calculate signal stdev
sdA0=std(A0);   %Calculate background stdev

while abs(c00-c0t)>0.001    %Guess max/min background scale until within tolerance
    c0t=c00;

    Btest=I-(c0)*A0;    %Guess 1, minimum scale, c=0
    c01=(-sdI/(-sdA0/sqrt(1+(std(Btest)/sdA0)^2))); %Change of variance WRT guess

    Btest2=I-(c0-2*c01)*A0; %Guess 2, maximum scale, c=2*c01
    c02=2*c01-(sdI/(-sdA0/sqrt(1+(std(Btest)/sdA0)^2)));    %Change of variance WRT guess

    c00=(c01+c02)/2;    %Average max/min to get best guess
end
```

```
c=[0.001:0.001:c02];    %Initialize c array (scale modifier)
B=zeros(length(c),length(I));   %Initialize B array
varB=zeros(length(c),1);    %Initialize variance array
c=c';

while n<=length(c)  %For each value of c...
    B(n,:)=I-(c00*c(n))*A0; %...compute B
    varB(n)=var(B(n,:));    %...compute variance
    n=n+1;
end

[minV,minVi] = min(varB);   %Find optimal c value based on minimum variance

Bf = I-(c00-c(minVi))*A0;   %Calculate B output with best c00 ans c values
```

Appendix B

MATLAB Code for Waveform Simulation

This appendix contains the MATLAB code for the waveform simulations used to model AODs and wide-field iSCAT imaging, as discussed in Ch. 5.1.2. Fig. B.1 shows the results of the simulations, as well as experimental observations validating those results.

Experimental results were collected using the SensL photodiode and reconstructed in MATLAB using data retrieved from the function generators. See Ch. 9.1 for a description of this process. Resulting images have been cropped for clarity.

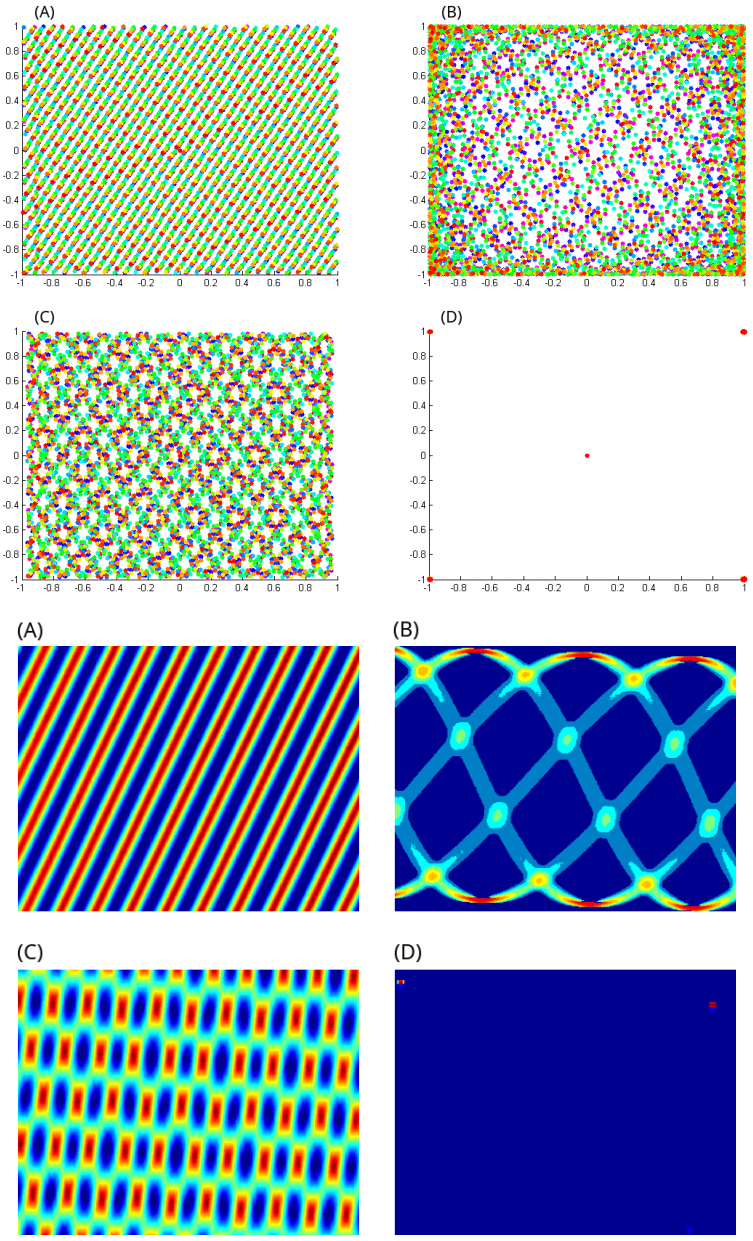

Figure B.1: Results of MATLAB simulations (top; reproduction of Fig. 5.3), and corresponding experimental observations (bottom).
A: Sawtooth wave.
B: Sine wave.
C: Triangle wave.
D: Square wave.

```
%%%%%%%%%%%%%%%%%%
% MATLAB simulation for AOD drivers
% by Ashton Christy, 17 Jul 2014
%
% Function generator outputs -> VCO outputs -> deflection angles -> illuminated pixel
% Vx(t),Vy(t) -> wx(t),wy(t) -> theta,phi -> x,y
%

clear;clc;close all;

N=13000;    %Number of simluation points

m=1:N;
x=zeros(N,1);
y=zeros(N,1);
color=1:N;  %Set up colors for final output
colormap('hsv');

% Frequency, phase, for X
fx=40;
px=0;

% Frequency, phase, for Y
fy=39.0;
py=pi/2;

Vx=RCwavetri(fx,px,N);  % Calculate X function; see next page
Vy=RCwavetri(fy,py,N);  % Calculate Y function

for n=1:N
    dx(n)=Vx(n);        % Update change in x,y
    dy(n)=Vy(n);
end

for n=2:N
    x(n)=x(n)+dx(n-1);  % Update x,y
    y(n)=y(n)+dy(n-1);
end

figure(1); scatter(x,y,250,color,'.')
```

```
%%%%%%%%%%%%%%%%%%
% MATLAB function for AOD driver simulations
% by Ashton Christy, 17 Jul 2014
%

function [y_sim]=RCwavetri(f,p,N)

num = 2;
den = [1 2];
H_s = tf(num, den);

w_o=(f*0.1)+0.9;  %Freq

t = linspace(0, 13000, N);

x_sim = sawtooth(w_o*t+p);  %Replace with desired waveform (sin, square, etc)
y_sim = lsim(H_s,x_sim,t);
```